# Tunable Field Enhancement in Plasmonic Nanostructures

*Edward John Osley*

Department of Electronic and Electrical Engineering

University College London

A dissertation submitted in partial fulfillment of the requirements for the degree of Doctor of Philosophy.

March 2013

*I, Edward John Osley, confirm that the work presented in this thesis is my own. Where information has been derived from other sources, I confirm that this has been indicated in the thesis.*

To my Mother and Father,

S. K. and N. J. Osley.

# Abstract

Metallic nanostructures that contain bound geometries will support localised surface plasmon (LSP) resonances if they are illuminated with light of appropriate frequency. These LSP resonances result in a concentration of the electric field of the incident light into a volume which is smaller than the photon wavelength. Certain geometries that support LSP resonances are sensitive to the polarisation of incident light, and the enhanced electromagnetic field can therefore be tuned *in situ* by adjusting this polarisation. We have investigated polarisation tunable LSP field enhancement by observing, in the linear regime, the interaction of an asymmetric cruciform aperture structure with a chemical bond and, in the non-linear regime, the second harmonic generation (SHG) produced by three metallic nanostructures.

Numerical simulations implementing rigorous coupled-wave analysis (RCWA) were used to find asymmetric cruciform aperture dimensions that produced LSP resonances when illuminated with light of a wavelength between 2 $\mu$m and 8 $\mu$m. Arrays of these apertures were fabricated in a 35 nm thick gold film on a transparent calcium fluoride ($CaF_2$) substrate. The fabrication methods used to create the apertures were either focused ion beam (FIB) milling, or electron beam lithography (EBL) with argon ion milling, of the gold film. Fourier transform infrared spectroscopy (FTIR) was used to measure the transmission and reflection spectra of these plasmonic nanostructures.

The apertures were coated with poly(methyl methacrylate) (PMMA), which has a local absorption maximum at 5.784 $\mu$m created by the stretching of its carbonyl bonds. The transmission and reflection spectra of the PMMA-coated apertures were measured using FTIR. The interaction of the LSP and molecular resonances was shown to form an asymmetric Fano resonance at

the carbonyl bond wavelength. We found that this Fano resonance can be tuned *in situ* by rotating the polarisation of incident light. A classical mechanical oscillator model was developed to interpret the reflection and transmission spectrum in terms of the interference of the LSP and molecular resonances. A quantum mechanical model was also developed and used to predict the absorption spectrum of the system. This quantum mechanical model provides information on the physical interactions within the system, and predicts a near-field mediated interaction between the plasmon and molecular resonances.

Nonlinear optical measurements were made using an SHG microscope, which allowed the location of near-field SHG hotspots to be determined. Three geometries were measured using this technique using fundamental wavelengths of 800 nm or 1 $\mu$m. The first geometry, a chiral star structure, was found to display dichroic SHG that was dependent on the handedness of the incident circularly-polarised fundamental light. The second, a 'windmill' structure, was used to investigate the dependence of near-field SHG on the linear polarisation of fundamental light; the ablation of these metallic windmill structures by the fundamental demonstrates that laser ablation of patterned surfaces is dependent on the LSP resonance of the constituent structures. Finally, the spatial dependence of SHG produced by a cruciform aperture structure in a gold film illuminated by linearly polarised light was observed. SHG intensity was found to be greatest along the axis of the cruciform which was perpendicular to the incident **E** field polarisation.

# Acknowledgements

I would like to sincerely thank my supervisor Dr. Paul A. Warburton for his invaluable help and advice throughout this work. I would like to thank Dr. Nicolae C. Panoiu for his extremely helpful and illuminating theoretical discussions and quantum mechanical calculations. I thank Dr. Ventsislav K. Valev for initiating our fruitful collaboration and for taking SHG microscopy measurements. I would like to thank Dr. Claudiu G. Biris for performing the initial rigorous coupled-wave analysis of the investigated system and for teaching me how to do this myself. In addition I would like to thank Paul Thompson, who has always been willing to discuss ideas and technical problems, and Huan Wang, for her encouragement and advice, and for both being such good friends throughout our time working together on our respective PhDs.

# Contents

# List of Figures

# Chapter 1

# Introduction

When light is incident on a metallic structure its electromagnetic field interacts with electrons in the metal. Depending on the size and shape of the structure and the wavelength and polarisation of the incident light, density waves of electrons may form near the surface of the metal. These density waves, which are driven at the frequency of the incident light, are described as either surface plasmon polaritons (SPPs) or localised surface plasmons (LSPs), depending on their behaviour. SPPs propagate across the metallic surface and are formed when the incident light and the plasmon are phase matched; this can be achieved by *eg.* periodic structures or prisms (see Section 2.2). LSPs are stationary and the product of bound geometries (see Section 2.3). SPP and LSP resonances occur in sub-wavelength structures and may therefore result in the concentration of the incident electromagnetic wave into volumes which are smaller than the photon wavelength, causing an electromagnetic field enhancement close to the metallic surface.

Although SPPs and LSPs have been known for a long time, sub-wavelength apertures which support these resonances have become the subject of intense research since Ebbesen *et al.* demonstrated extraordinary optical transmis-

sion in 1998 [1]. The resonances of sub-wavelength apertures which support LSPs are strongly dependent on the size and shape of the aperture. However LSP formation is not restricted to apertures in metallic films as rough metallic surfaces and sub-wavelength metallic particles interact with light in the same way. We are therefore able to engineer plasmonic materials with a broad range of resonances and electric field distributions. These patterned materials provide a versatile platform for investigating the interaction of enhanced electromagnetic fields over a large portion of the electromagnetic spectrum. As these apertures and particles have sub-wavelength dimensions that can be engineered to produce optical effects not normally observed in nature they are referred to as meta-molecules, the building blocks of meta-surfaces and meta-materials.

The field enhancements produced by meta-molecules have many applications, both in fundamental science and engineering. Applications include surface-enhanced Raman spectroscopy [2], infrared absorption spectroscopy [3], and biosensing [4]. In many of these applications it is desirable to tune the strength of the coupling between a plasmonic resonance of the meta-molecule and the resonance of an optically active material. As asymmetric meta-molecules have intrinsic optical anisotropy, an effective *in situ* approach to the tuning of the enhanced field produced by these structures is to control the polarisation of incident light. It has been shown theoretically [5] and experimentally [6] that plasmonic meta-molecules consisting of asymmetric cruciform apertures in thin metallic films support plasmonic resonances and associated field enhancements which are strongly dependent on the incident electric field polarisation.

Another effective approach to engineering the line shape of the resonance of a plasmonic system relies on the interference between relatively

narrow and broad plasmonic modes. The interference of these narrow and broad modes produces a Fano resonance, a general interference phenomenon which can be applied to any physical system where narrow and broad resonances interfere. In plasmonic systems the Fano formula has been used to describe the interaction of bright and dark modes, and the interaction between broad plasmon resonances and discrete molecular vibrations. As the Fano resonance is primarily formed by short-range, near-field interactions the transmission and reflection spectra resulting from this interference provides physical insight into light-matter interaction at the nanoscale.

The field enhancement produced by metallic structures that support LSPs may combine with the symmetry breaking at the metal dielectric interface to allow surface second harmonic generation (SHG). This enhancement has been observed in rough metallic films where plasmon resonances produce SHG hotspots in the near-field. The SHG produced by patterned surfaces is more intense and controllable than the SHG produced by a non-patterned metallic film. The study of the near-field SHG allows far-field SHG optical effects to be linked to surface morphology. As near-field SHG hotspots are located in regions that support high field enhancement the study of these hotspots is also relevant to the understanding of linear optical effects which are dependent on this localised field enhancement. The patterning of surfaces allows the formation of these hotspots to be investigated systematically, allowing us to probe the origins of SHG dichroism, using both linear and circularly polarised light. New effects can also be investigated, including sub-wavelength laser ablation caused by heating at the SHG hotspots.

## 1.1 A Review of Plasmonic Nanostructures

### 1.1.1 Extraordinary Optical Transmission

The wave-like nature of light causes diffraction to occur when a wavefront is partly obstructed by an opaque material. Bethe's theory of the diffraction of light by a small round hole with radius $r$ in a perfectly conducting, negligibly thick metal screen predicts that transmission scales as $(r/\lambda)^4$ where $\lambda$ is the wavelength of incident light [7]. This implies that for wavelengths much larger than the diameter of an aperture there should be negligible transmission.

In 1998 Ebbesen *et al.* discovered that in the case of periodic aperture arrays in metallic films Bethe is incorrect [1]. They fabricated arrays of apertures with diameters ranging from 150 nm to 1000 nm in thin (typically 200 nm thick) films using focused ion beam milling. A number of film materials were used: silver, chromium, gold and germanium. Figure 1.1 shows the transmission intensity of one of Ebbesen's arrays, the maximum transmitted intensity occurs at wavelength 1.370 $\mu$m. This wavelength is approximately nine times the diameter of the apertures in the array. They also found that more than twice as much light is transmitted as is directly illuminating the holes. The absence of this subwavelength transmission in hole arrays fabricated from germanium and the similarity in the behaviour of the transmission spectrum to that observed when light couples with surface plasmons in reflection gratings led them to relate this phenomenon to surface plasmon polaritons (propagating density waves of electrons). The effect was dubbed extraordinary optical transmission (EOT).

The effect of the material used to fabricate the apertures on the intensity of EOT has been investigated both experimentally and theoretically. Przy-

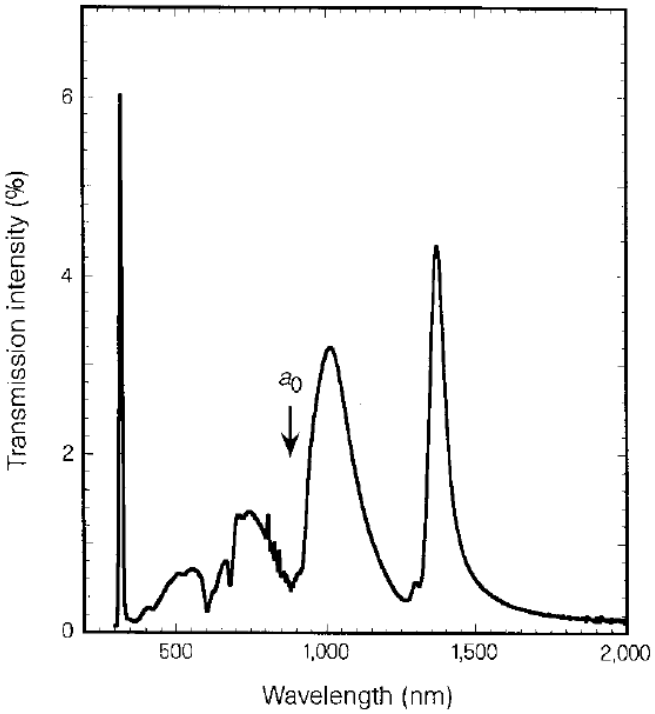


Figure 1.1: The zero-order transmission spectrum produced by an array of circular apertures milled in a 200 nm thick silver film. The aperture diameter is 150 nm and the array period $a_0$ is 900 nm. Reproduced from Ebbesen *et al.* [1].

billa *et al.* studied the transmission of circular aperture arrays fabricated by focused ion beam milling of Ag, Au, Cu, Co, Ni and W films [8]. They found that only the investigated noble metals (Ag, Au and Cu) supported significant EOT. This was linked to the real $\mathrm{Re}(\epsilon_m)$ and imaginary $\mathrm{Im}(\epsilon_m)$ parts of the dielectric constant of the metals investigated. When a metal has a large, negative $\mathrm{Re}(\epsilon_m)$, EOT was supported. Tungsten has positive $\mathrm{Re}(\epsilon_m)$ in the wavelength range studied (400 - 900 nm) and any transmission through tungsten apertures was shown to be purely diffractive. A small value of $\mathrm{Im}(\epsilon_m)$ was required for large EOT. This is because this term is related to the damping of the electron plasma in the metal. Hence noble metals, with small $\mathrm{Im}(\epsilon_m)$ terms, produced the maximum EOT. Rodrigo *et al.* investigated the optical response of circular aperture arrays in Ag, Au, Cu, Al, Ni, Cr, W and a perfect conductor theoretically [9]. Aperture arrays in a perfectly conducting film were calculated as having less transmission than aperture arrays of the same dimensions in Ag, Au and Cu films because the skin depth of these metals produces a larger effective hole area. Materials with long surface plasmon polariton (SPP) absorption lengths were also found to have higher transmittance.

Alternative aperture geometries have been investigated. Circular grooves surrounding a single aperture (and linear grooves running parallel to a sub wavelength slit) were found to couple incident light to the aperture with greater efficiency and reduce the angular divergence of the transmitted light [10].

The polarisation dependence of the transmission spectrum of subwavelength hole arrays has been found to be closely related to the shape of the apertures in the array [11]. Symmetrical aperture arrays do not exhibit polarisation dependent transmission, however rectangular or elliptical aper-

tures do [12]. The effect of aperture shape on EOT through gold films with subwavelength holes has been attributed to local surface plasmon (LSP) [13] and localised waveguide resonances [14]. LSP excitation has been identified as the mechanism which produces transmission in the investigated cruciform aperture geometry because of the insensitivity of the transmission to array periodicity and the existence of EOT in isolated apertures [5, 15]. The cruciform aperture geometry will be reviewed in the following section.

### 1.1.2 Cruciform Apertures and Resonance Tuning

We have chosen to work with asymmetric cruciform apertures because this geometry allows a greater degree of control over the plasmon resonance than is afforded by a simpler geometry. This is because a larger number of dimensions can be varied in the more complex cruciform shape: four dimensions may be varied in an asymmetric cruciform, as opposed to two in a rectangle, and one in a circle (neglecting metal layer thickness).

As the body of this work is concerned with the optical behaviour of sub-wavelength asymmetric cruciform apertures we will review previous applications of this aperture geometry here. We refer to a Swiss cross geometry consisting of two rectangles which both have their long and short axes centred on the origin; the overlapping rectangles form a void in a metallic film. The cross apertures may be asymmetric, having two arms longer or wider than the arms which cross them.

Cruciform apertures in metallic films have been investigated experimentally by several authors. Chen *et al.* observed the transmission of cruciform apertures in 100 nm thick silver film on a silicon substrate in 2007 [16]. The apertures had feature sizes between 3 $\mu$m and 7 $\mu$m and were resonant at approximately 36 $\mu$m wavelength. The transmission was found to be depen-

dent on the **E** field polarisation of incident light when asymmetric apertures were measured.

Lin, Roberts *et al.* have investigated the optical properties of symmetric cruciform apertures with sub micrometre feature sizes fabricated in gold films on glass substrates. In 2009 they investigated the role of SPP and LSP resonances on the transmission characteristics of symmetric cruciform apertures in the 600 - 1500 nm wavelength range [15]. The apertures were fabricated in a 140 nm thick gold film using focused ion beam milling. The cross arm width was approximately 40 nm and three lengths of cross arms were fabricated: 250 nm, 300nm and 350 nm. The crosses were arranged in a 40×40 $\mu$m array with periodicity 600 nm. A transmission minimum corresponding to the excitation of SPPs by the periodic array was observed at wavelength between 980 nm and 986 nm. At longer wavelengths LSPs were predicted as being the transmission mechanism. This interpretation was confirmed by Lin and Roberts in 2011 where they use a similar geometry to investigate the coupling of SPP and LSP modes [17]. They also concluded that the interference of SPP and LSP modes generates an asymmetric Fano lineshape in the transmission spectrum of the structures.

In 2010 Lin and Roberts investigated the effect of the angle of incidence of light on symmetric cruciform transmission [18]. 140 nm thick silver films were deposited on a glass substrate and symmetric cruciform apertures fabricated using focused ion beam milling. The LSP associated transmission peak of the apertures was found to be independent of the angle of incidence of TE polarised light, where as a red shift was observed in the case of TM polarised light. Lin, Roberts *et al.* have also produced a lens by combining different sized crosses in a circular array [19].

Roth *et al.* predicted the sensitivity of the transmission of asymmetric

cruciform apertures to the **E** field polarisation of incident light in 2007 [5]. The inset to Figure 1.2 shows the asymmetric aperture geometry in red. Simulations of a 100 nm thick gold layer perforated with a semi-infinite array of cross shaped apertures on an $SiO_2$ substrate were performed using rigorous coupled-wave analysis. The apertures had dimensions $L_x = 390$ nm, $L_y = 370$ nm, $g_x = 40$ nm, $g_y = 20$ nm and the aperture periodicity was 600 nm in both $x$ and $y$ directions. Figure 1.2 shows the transmission spectrum produced by the array at several incident **E** field polarisations. Two transmission peaks are discernable in the simulated transmission spectra, at wavelengths 1.56 $\mu$m and 2.07 $\mu$m, corresponding to an incident **E** field polarisation of 0° and 90° respectively. LSP modes were demonstrated theoretically as been responsible for the dependence of the structures resonant wavelength on the polarisation of incident light; this result was inferred from an examination of the polarisation dependence of simulated **E** field profiles produced by the structure. Changing the array period was found to shift the SPP associated features present at wavelengths shorter than 1 $\mu$m, the same behaviour was later observed experimentally by Lin, Roberts *et al.* in 2011 [17].

Experimental confirmation of the polarisation dependence of the transmission of asymmetric cruciform apertures has been presented by Thompson *et al.* in a paper in which I am a co-author [6]. Apertures were fabricated by focused ion beam milling of a 30 nm thick gold film and 5 nm thick chromium adhesion layer on a 0.5 mm thick calcium fluoride substrate. Figure 1.3 (a) shows the unit cell geometry schematically, (b) shows a typical array of apertures containing 15×15 unit cells and (c) shows the apertures in cross section. The arrays were measured using Fourier transform infrared spectroscopy (FTIR) (see Section 3.2.1).

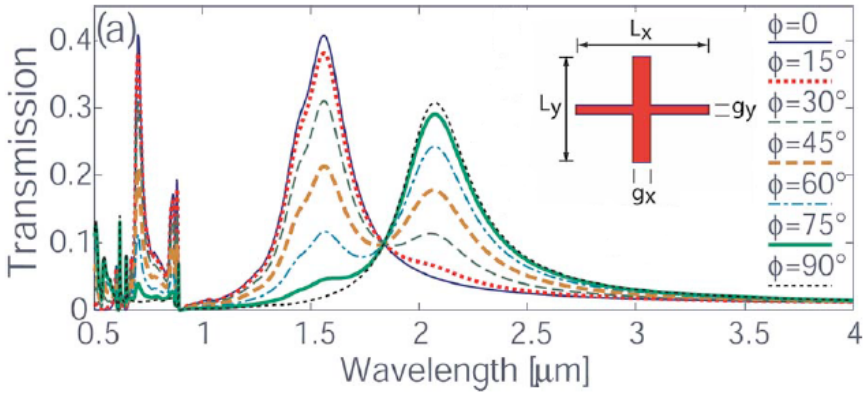


Figure 1.2: Simulated transmission spectrum of an asymmetric cruciform aperture array for varying incident **E** field polarisations from 0° to 90° at 15° intervals. The inset shows a unit cell. The aperture dimensions used in the simulations are $g_x = 40$ nm, $g_y = 20$ nm, $L_x = 390$ nm, $L_y = 370$ nm; the array periodicity is 600 nm in both $x$ and $y$ and the gold thickness is 100 nm.

Reproduced from Roth *et al.* [5].

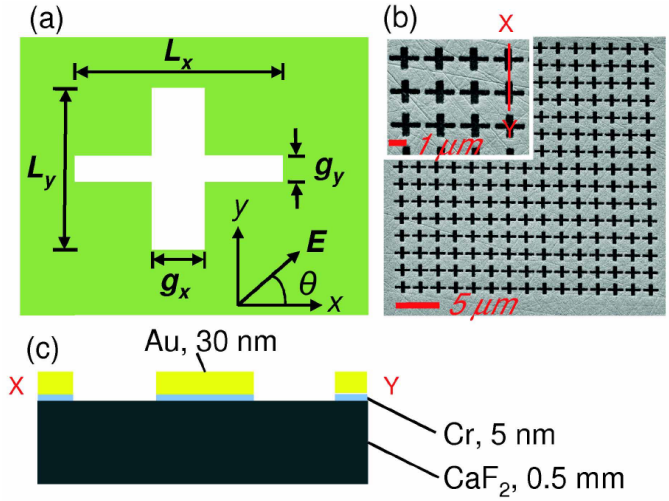


Figure 1.3: (a) Schematic representation of the aperture unit cell and definition of the **E** field polarisation angle $\theta$. (b) Scanning electron micrograph of a typical aperture array. (c) Schematic cross-section through the XY-segment shown in the inset to (b). Reproduced from Thompson *et al.* [6].

Figure 1.4 shows the transmission, reflection and absorption spectra of the arrays of asymmetric apertures, as well as the transmission of a symmetrical aperture array. The spectra are measured at **E** field polarisation angles varying between $\theta = 0°$ and $\theta = 90°$ in 15° increments. Panels (a), (c) and (e) show the spectra of the asymmetric apertures measured experimentally, and panels (b), (d) and (f) show the spectra for the same structure predicted theoretically using the rigorous coupled-wave analysis method. The transmission of a symmetrical structures is presented in panels (g) and (h), and is unchanged by rotation of the incident **E** field polarisation. In the panels the letters A and B label LSP resonances, the position of which are independent of the **E** field polarisation; I labels the isosbestic point where transmission, reflection and absorption are independent of **E** field polarisation; W labels the Wood's anomaly; C labels SPP resonances excited by the periodic arrangement of the array. A detailed discussion of the transmission, reflection and absorption of this structure is included in Chapter 4. The numerical simulations were also used to identify the LSP modes supported by the arms of the asymmetric apertures, and the associated increase in local **E** field magnitude.

In the same work Thompson *et al.* varied the aperture dimensions to determine design rules for tuning the resonance of the apertures. The length of the arms was found to determine the natural resonance of the two modes. Figure 1.5 shows the change in resonance of the modes as the aperture arm length $L_y$ is changed. The two transmission peaks labeled A and B and the isosbestic point labeled I (corresponding to the labels in Figure 1.4 (a)) are plotted with respect to changing $L_y$, all other dimensions remaining constant. Peak B remains at a constant wavelength whereas peak A and the isosbestic point red shift as $L_y$ increases.

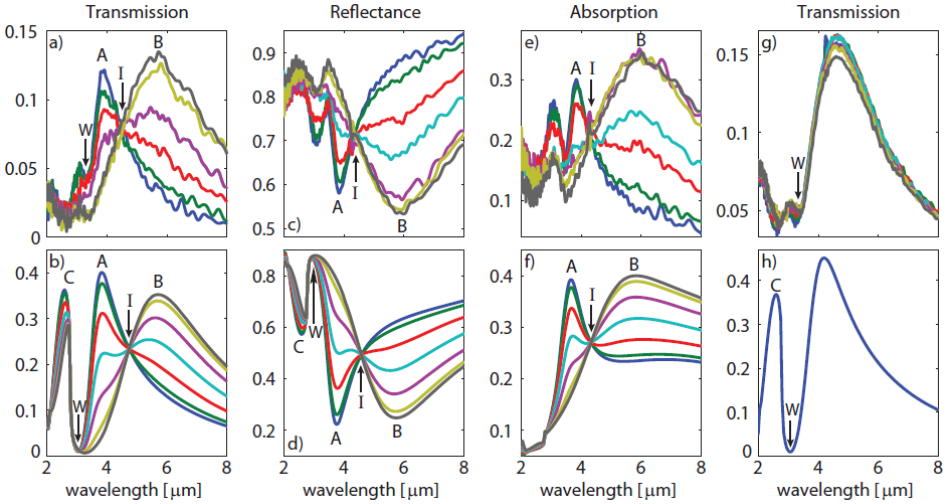


Figure 1.4: (a), (c) and (e) Measured transmission, reflection and absorption spectra (respectively) of an array of asymmetric cruciform apertures. Aperture dimensions are $g_x = 418$ nm, $g_y = 165$ nm, $L_x = 1675$ nm and $L_y = 1003$ nm. The spectra show **E** field polarisation angles varying between $\theta = 0°$ and $\theta = 90°$ in increments of 15°. (b), (d) and (f) Numerical simulation of the transmission, reflection and absorption of the measured structures. (g) and (h) Measured and simulated (respectively) transmission spectra of a symmetric cruciform array with aperture dimensions $g_x = g_y = 368$ nm and $L_x = L_y = 1264$ nm. Reproduced from Thompson *et al.* [6].

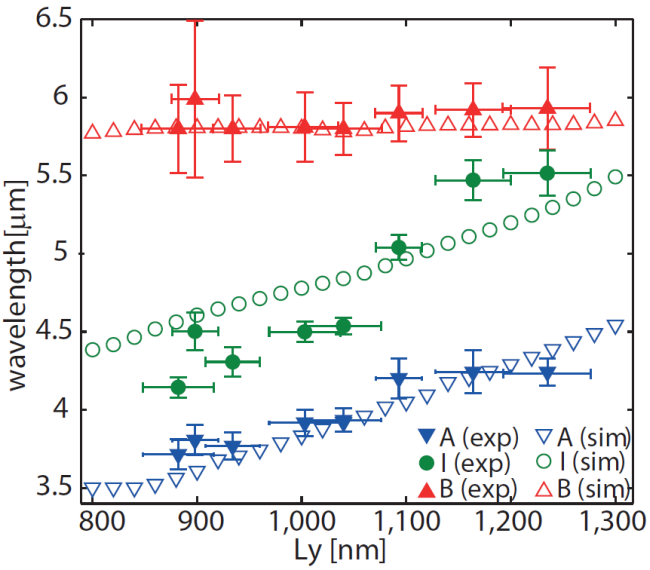


Figure 1.5: $L_y$ dependence of the transmission of the cruciform structure at resonances A (blue), B (red) and the isosbestic point I (green), coresponding to the features labeled A, B and I in Figure 1.4 (a) and (b). Solid points are experimental measurements, hollow points are taken from numerical simulations. Error bars in $L_y$ correspond to standard deviation of fabricated device dimentions. Reproduced from Thompson *et al.* [6].

#### Additional Resonance Tuning Techniques

As well as sensitivity to polarised light, there are other methods of tuning the resonance of a plasmonic device *in situ*. These methods involve physically altering the structure in some way, *e.g.*, by changing the spacing of metallic components or altering the devices' electronic properties. In 2006 Chen *et al.* investigated an active terahertz metamaterial consisting of an array of Schottky diodes in which the transmission of the metamaterial at approximately 1 THz increases with gate voltage bias [20]. Xiao *et al.* used temperature to tune the resonance of a metamaterial consisting of gold nanostrips coated with a nematic liquid crystal [21]. In this design increasing temperature from 20 °C to 50 °C caused a phase change in the liquid crystals which is linked to a change in refractive index, this change alters the resonance of the metallic strips. Temperature change has also been used to alter the electrical properties of an array of split ring resonator made of $YBa_2Cu_3O_{7-\delta}$ (YBCO), a high-temperature superconducting material [22]. At a frequency of 0.6 THz the transmission of the structure decreases from ∼60% at 100 K to ∼5% at 20 K.

The complexity of these additional tuning techniques illustrates the advantage of using the polarisation of incident light as our tuning mechanism. It is the simplest method which allows *in situ* tuning of the plasmon resonance, requiring only a polarisation filter or a quarter or half wave plate.

### 1.1.3 The Fano Resonance in Plasmonic Structures

Plasmonic systems can be engineered to possess narrow and broad resonances which can interfere with each other and with other resonant systems which are placed close to them, *eg.* molecular resonances. The interference of narrow and broad resonances may be described by the Fano formula which

was originally developed to explain asymmetric peaks observed during the autoionization of noble gases by Fano in 1961 [23]. The Fano resonance is discussed in Section 2.4. As the interaction of a tunable plasmonic resonance and a molecular vibrational mode is the primary focus of this work we will now review existing investigations into this phenomenon.

Interaction between broad and narrow resonances in a plasmonic structure may be split into two types. In one the plasmon field couples to a molecule, whereas the other involves the coupling of bright and dark plasmonic modes. We shall introduce bright and dark mode coupling and observation of the Fano resonance in these structures. Following this we introduce plasmon-molecule coupling and the observation of the Fano resonance in these configurations.

### Bright and Dark Modes

Stockman *et al.* theoretically investigated the surface plasmons (eigenmodes) formed on random planar composites [24]. In addition to surface plasmons that are excited by the far-field they predicted the formation of surface plasmons that do not couple to far-field propagating waves and which cannot radiate. Stockman *et al.* named the two plasmonic modes luminous and dark; they are also referred to as bright and dark or radiative and non-radiative plasmon modes in other texts. The dark modes may only be excited from the near-field zone within the system, indicating that dark modes may be excited by coupling to the near-field of the externally excited bright modes.

Zhang *et al.* proposed a plasmonic structure containing metallic elements that support bright and dark modes in 2008 [25]. If the bright and dark structures are placed close together, the electric fields produced by

the structures' surface plasmons were predicted to interact. The combined structure formed of the two elements is referred to as a metamolecule.

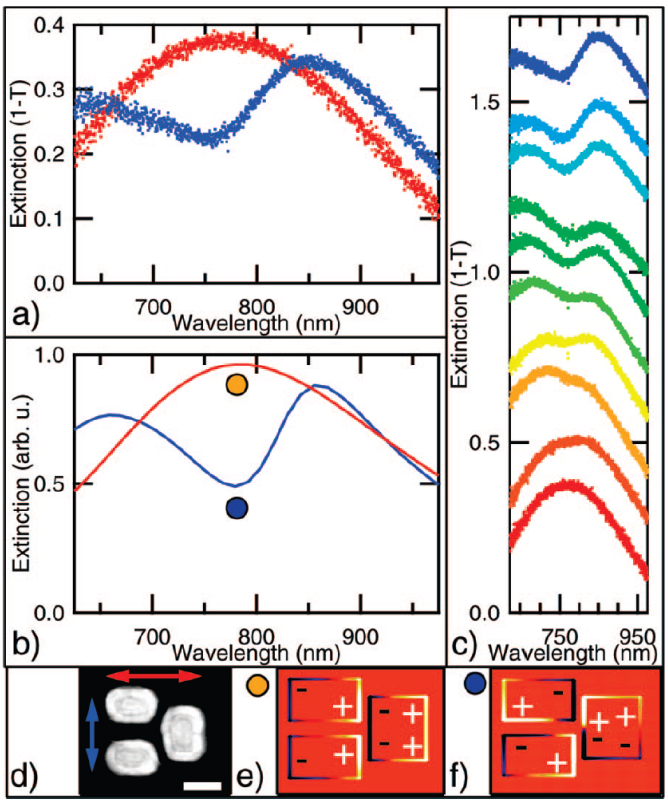


Figure 1.6: (d) A dolmen-type structure, the scale bar is 100 nm. The red arrow shows an **E** field polarisation of 0°, the blue arrow shows a polarisation of 90°. (e) (f) Calculated surface charge distributions for the dolmen structure at **E** field polarisations 0° and 90° respectively. (a) Measured extinction of the dolmen structure, (b) theoretical simulation of the same structure; incident **E** field polarisations are 0° (red) and 90° (blue) in both plots. (c) Measured extinction of the dolmen structure in 10° intervals from 0° (red) to 90° (blue), axis shifted. Reproduced from Verellen *et al.* [26].

Figure 1.6 (d) shows the metamolecule as fabricated by Verellen *et al.* in 2009 [26]. The structure, widely referred to as dolmen-type, contains three metallic rectangles and is sensitive to the incident **E** field polarisation. Two metallic rectangles that lie parallel to each other (on the left of the figure) constitute the dark element; this element cannot couple to incident light

with an **E** field polarisation perpendicular to the two rectangles' long axis at the wavelength which excites the bright element. The bright element is a single metallic rectangle (on the right of the figure) that can couple to incident light with **E** field polarisation parallel to its long axis. Therefore the structure is sensitive to the polarisation of incident light and must be illuminated with **E** field polarisation parallel to the long axis of the bright element for this element to be excited and couple to the dark mode. The polarisation sensitivity of the metamolecule is shown in Figure 1.6 (c) where the extinction of the structures relative to the incident **E** field polarisation is shown in 10° steps. Plates (a) and (b) show respectively the measured and calculated extinction from an array of the dolmen-type structures. The surface charge distribution on the structures is shown in plates (e) and (f) for **E** field polarisations 0° and 90° respectively. Because the resonance of the dark mode is much narrower than the resonance of the bright mode the metamolecule was predicted to form an asymmetric Fano resonance. In the same paper Verellen *et al.* also investigate an alternative geometry containing a ring and a circle of gold which operates on the same principles. Similar results were produced by Hao *et al.* in 2007 and 2008 [27, 28] and Sonnefraud *et al.* in 2010 [29], who both use concentric gold ring and circle structures. In this geometry the metallic ring supports a bright mode and the metallic circle in its center supports a dark mode. The interaction of the two modes produces a Fano resonance. The Fano resonance has also been observed in self-assembled plasmonic nanoparticle clusters [30, 31].

The Fano resonance formed by the bright and dark modes of a plasmonic structure was investigated theoretically by Gallinet and Martin in 2011 [32]. They applied Fano's quantum mechanical idea to electromagnetic scattering from a metallic object imbedded in a dielectric background. They applied

this theory to the bright and dark modes of the dolmen-type plasmonic metamolecule. In addition they model the system mechanically by applying the work of Alzar *et al.* who used mechanical oscillators to model electromagnetically induced transparency in 2002 [33] and Joe *et al.* who modeled the Fano resonance using a mechanical oscillator in 2006 [34]. Gallinet and Martin were able to show that this mechanical analogue is equivalent to their electromagnetically derived Fano formula. For a detailed discussion of the Fano resonance and its mechanical analogue please see Sections 2.4.1 and 2.4.2.

Wu *et al.* have applied the narrow Fano resonance produce by coupled bright and dark modes in plasmonic structures to biosensing [35].

### Plasmon Molecule Interactions

SSP and LSP resonances are associated with an increase in electromagnetic fields near the surface of the supporting metal. This effect is exploited by surface enhanced Raman spectroscopy [2, 36], and has been studied using second harmonic generation [37]. The electromagnetic field enhancement in sub-wavelength apertures was first predicted by theoretical calculations [38, 39], and confirmed using a near-field scanning optical microscope [40].

The enhanced fields produced by SPPs during extraordinary transmission have been used to enhance the infrared absorption of molecules [41, 42] and have been applied to surface enhanced infrared absorption spectroscopy [3]. Williams *et al.* coated 1-dodecanethiol onto a nickel mesh that had been shown to support extraordinary transmission and observed an increase in infrared absorption at wavelengths associated with C-H stretching [41]. They postulated that the absorption increase was caused by an increase in path length produced by SPPs. Other studies however suggest that this

interpretation is erroneous and the actual mechanism is an increase in field amplitudes [43, 44, 45] or reduction in group velocity of light travelling through the holes [46].

Dintinger *et al.* analyzed the interaction of dye (J-aggregate) molecules suspended in a polyvinyl alcohol (PVA) films and SPPs produced by an aperture array in a silver film [43]. The energy of the surface plasmon polaritons was varied by creating a number of samples with different aperture period and by changing the angle of incidence of light falling on an array. Both methods indicated a strong coupling regime between the dye and the enhanced fields produced by the array. Sugawara *et al.* observe an increase in absorption of J-aggregate placed with spherical nanovoids in a gold film and conclude that the absorption spectra show strong coupling between the dye and localised surface plasmons [45]. Coupling between plasmons and molecules has also been observed in gold nanorods [47], noble metal nanocrystals [48, 49] and bowtie nanoantenna [50].

Neubrech *et al.* designed gold nanowires with length $\sim$1.5 $\mu$m and diameter $\sim$100 nm that have a plasmonic resonance of approximately 3.6 $\mu$m, which is close to the resonant wavelength of octadecanthiol [ODT, $CH_3(CH_2)_{16}CH_2SH$] which has vibration modes at approximately 3 $\mu$m wavelength [48]. These nanowires act as half wavelength dipole nanoantennas. They found that following the adsorption of a monolayer of ODT onto the nanowires, coupling between the plasmonic and molecular resonances enhanced the detection of the molecular vibration when using IR microspectroscopy. The nanowires absorbed light with wavelength $\sim$3.6 $\mu$m when the incident **E** field polarisation was parallel to the nanowires (light with **E** field polarisation perpendicular to the nanowires was not absorbed). The infrared transmission through the nanowires showed a five orders of

magnitude increase in the spectroscopy signature of the molecules compared to the same number of molecules on a plain gold surface. The interaction of the broad resonance of the nanowires and the narrow resonance of the ODT was seen to produce an asymmetric Fano line shape in the extinction cross section.

Pryce *et al.* have made plasmonic structures with resonances that can be tuned mechanically by flexing an elastomeric substrate [51]. By straining the substrate, the separation of resonant plasmonic elements is altered and the resonance of the structure is modified. Dolmen type structures containing 100 nm thick gold features chemically bonded to a 1 mm thick polydimethylsiloxane (PDMS) substrate were fabricated using electron beam lithography (EBL). The sections of the dolmen resonators were stretched apart when the substrate is deformed, causing the optical resonance to change. The PDMS substrate contains a C=H bond that stretches at 3.37 $\mu$m and the resonators may be engineered to have resonance at this wavelength. Figure 1.7 shows the tuning of the plasmon resonance and the interaction of the plasmon and molecular resonances. The stretching of the substrate causes the Fano resonance produced by the interaction of bright and dark plasmonic modes formed by the dolmen structures to change. Split ring resonator arrays were also measured.

Giannini *et al.* also consider the interaction of nanoantennas with molecules [52]. They produce a parameter free modeling approach based on Fano's work (a description of this model is included in Section 4.4.2). To test their model they fabricate an array of gold strips on a barium fluoride substrate using EBL. The width of the strips is 100 nm and they are 20 nm thick. The lengths $L$ vary from 1 to 2 $\mu$m, with the resonance of the structures being dependent on this parameter. The strips are arranged in an array with a

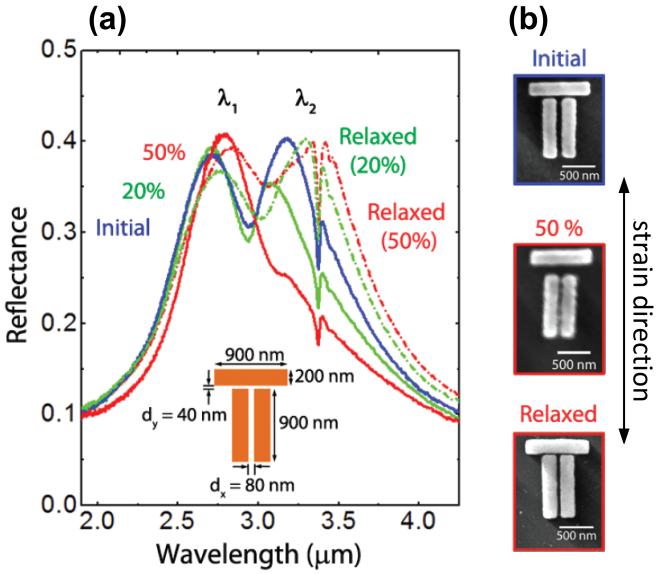


Figure 1.7: (a) Measured reflection spectrum from a dolmen type structure fabricated on an elastomeric substrate at various substrate strains. Inset shows the dolmen geometry. (b) SEM micrographs showing representative structures of those measured in (a) at different strains. Reproduced from Pryce *et al.* [51].

lateral spacing of 1.2 $\mu$m and 50 nm spacing from tip to tip. The strips are coated with Poly(methyl methacrylate) which has a carbonyl bond resonance at 1729 cm$^{-1}$ (approximately 5.8 $\mu$m wavelength) [53]. Figure 1.8 shows the extinction of the structure for varying values of $L$. The broad peaks are formed by the absorption of the nanoantennas. The local peak at 1729 cm$^{-1}$ is formed by the interaction of the broad plasmon resonance and the narrow carbonyl bond resonance. Their parameter free theoretical description is also applied to the bright and dark modes of a dolmen-type structure.

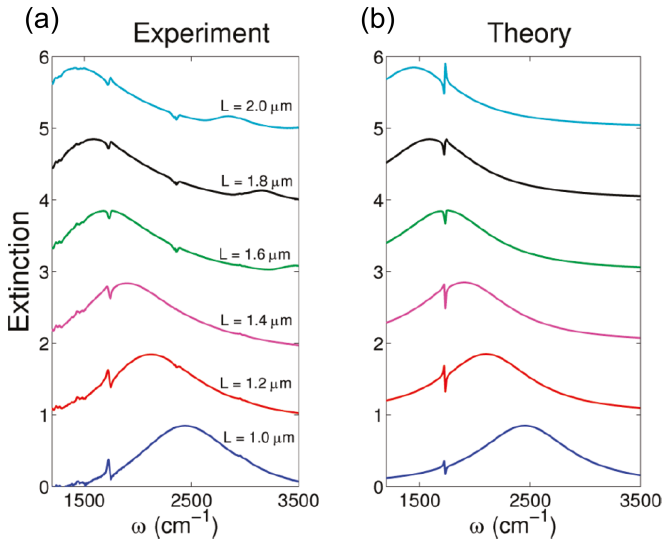


Figure 1.8: (a) Experimental measurement of the extinction of nanoantenna of length $L$ covered with PMMA. (b) Theoretical prediction of the extinction of the measured structures based on Fano formula with no fitting parameters. The extinction axis in both plots is shifted. Reproduced from Giannini *et al.* [52].

Hutchison *et al.* have observed plasmon-molecule interactions that result in an increase in transparency at the wavelengths at which the molecules absorb strongly [54]. This effect is called absorption-induced transparency (AIT). Figure 1.9 shows the transmission spectrum of an array of 100 nm

diameter apertures in a 200 nm thick silver film arranged in a square with a pitch of 250 nm in $x$ and $y$. The black curve shows the transmission of the aperture array in air. The red curve shows the transmission of the aperture array after a 30 nm layer of the green dye cyanine J-aggregate was adsorbed on the surface. A large increase in the array transmission at 697 nm wavelength is discernible in the red curve; this wavelength is associated with the absorption spectrum of the molecular layer. The experiment has also been carried out with a random arrangement of apertures. In this case there was very little transmission from the apertures in air (as the SPPs cannot form without a periodic aperture array); however, following the addition of the dye the large transmission peak at 697 nm wavelength appeared. This suggests that LSPs are involved in the interactions between the incident light, the molecules, and the metallic film. The coupling of electron charge oscillations in the dye and electrons in the metal excites plasmons which radiate at the excitation frequency of the dye.

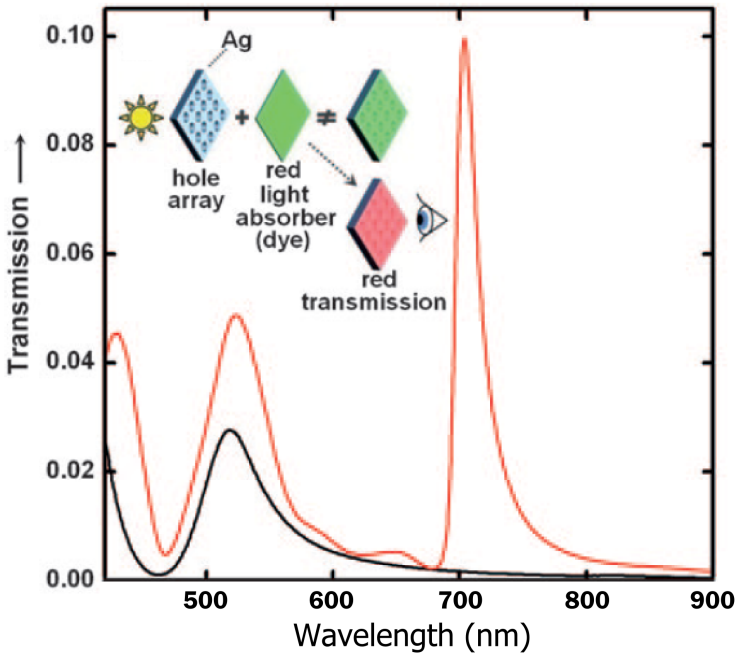


Figure 1.9: Transmission of a sub-wavelength aperture array. The black curve shows the transmission in air, the red curve shows the transmission when the array is coated with cyanine J-aggregate. The inset shows a cartoon depicting absorption-induced transparency (AIT). Reproduced from Hutchison *et al.* [54].

### 1.1.4 Second Harmonic Generation in Plasmonic Structures

When high intensity light illuminates a material, nonlinear optical effects such as harmonic generation, frequency mixing and intensity-dependent refractive indices may occur [55]. Harmonic generation produces light at multiples of the fundamental frequency of the illuminating light and is sometimes referred to as frequency doubling, tripling *etc.* depending on the harmonic. The origin of harmonic generation, with special attention paid to second harmonic generation (SHG), is discussed in Section 3.2.2. The intense optical fields required to produce nonlinear optical effects meant that they only became experimentally accessible following the development of the laser. SHG was first observed experimentally by Franken *et al.* in 1961 when a fundamental laser of wavelength 6943 Å was shone through crystalline quartz, producing SHG at ∼3472 Å [56].

Even with a high intensity laser light source SHG is not guaranteed as the propagation of the second harmonic may be prevented by the physical properties of the material. In the case of bulk SHG the material must be transparent at both the fundamental and second harmonic frequencies and have a non-centrosymmetric atomic arrangement, which allows the SHG to propagate through the material without destructively interfering with itself. These conditions are met in a number of materials and SHG has been observed in periodically poled semiconductors, nonlinear crystals, polymers containing poled chromophores and some Langmuir-Blodgett films [55, 57, 58].

The surfaces of centrosymmetric materials may also produce SHG as the symmetry of the bulk material is broken at the surface, making this region inherently non-centrosymmetric. Surface-SHG from a centrosymmetric material was first observed by Terhune *et al.* in 1962 when they illuminated a

calcite crystal with a one Joule pulsed ruby laser [59]. A detailed theoretical discussion of the phenomenon, along with experimental observations of surface-SHG from silicon, germanium and gold, was presented by Bloembergen *et al.* in 1968 [60]. Surface-SHG is extremely sensitive to surface composition and the effect may be used to monitor the adsorption of material with a thickness of one monolayer and surface dynamics with sub-picosecond time resolution [61, 62].

The intensity of surface-SHG produced by metals is very sensitive to the roughness of the surface, or sub-wavelength surface pattering. In 1981 Chen *et al.* observed a $10^4$ enhancement of the surface-SHG from an electrolytically roughened silver film in comparison with a the surface-SHG produced by a smooth silver film [63]. The increase in surface-SHG intensity is caused by electric field lines being confined at sharp points on the metal surface (the lightning rod effect) and by SPP and LSP resonances which are supported by surface structures. The LSPs and SPPs produce surface areas with increased charge density which leads to large **E** field enhancements. The enhancements are inhomogeneous and referred to as the near-field, with the individual near-field enhancements contributing to the total enhancement of surface-SHG observed in the far-field.

Smolyaninov, Zayats and Davis have used a scanning near-field optical microscope (SNOM) to measure the near-field SHG of a rough metallic surface [64, 65]. In this experimental arrangement the surface is illuminated by either S or P linearly polarised laser light and a fine uncoated fibre optic filament is scanned over the surface using a three axis piezo-tube. Light collected by the tip of the fibre optic is passed to a photomultiplier through a filter which removes the fundamental wavelength. The near-field SHG is inhomogeneous for both S and P polarised light. SHG was found to be

dependent on the surface topology for S-polarised light. However, when illuminated with P-polarised light the SHG was found to be more complicated. When a P-polarised fundamental was used, bright spots were found to be a similar size to regions of enhanced near-field produced by SPPs. In 2000 the same method was used by Zayats *et al.* to measure an order of magnitude increase in the SHG from micrometer size defects on a gold surface [66]. Rossi *et al.* used the techneque to measure the near-field SHG of metallic particles fabricated by EBL in 2008 [67].

Other techniques have been used to detect the SHG from particles, including two-photon microscopy which has been used to image the local SHG of granular gold structures [68] and the hyper-Rayleigh scattering of gold particles embedded in gelatin [69].

With increased access to nanofabrication techniques more work has been carried out to investigate the SHG produced by nano-patterned surfaces. This topic is interesting because the surface-SHG can be engineered by tailoring the SSP and LSP resonances of the surface, allowing greater control over the enhancement than a random rough surface. The pattering of a surface also allows control over the position of SHG hot spots. Patterns have been created by self-organisation of metallic nanowires [70, 71] and by semiconductor fabrication techniques including EBL.

### Second Harmonic Generation Microscopy of Nanopatterned Surfaces

Two-photon microscopy led to the development of SHG microscopy for use in the biological sciences [72] and this technique was applied to random metal nanostructures in 2003 [73]. SHG microscopy will be used in this work and we review its application to the investigation of patterned metallic surfaces

below. The experimental arrangement and technique is discussed in Section 3.2.2.

Chiral patterned surfaces have been investigated in the linear energy regime in the far-field since 2003 [74]. In 2009 Valev *et al.* investigated the SHG produced by chiral structures in the far- and near-fields [75]. Their structures consist of a repeating G shaped pattern made of a 25 nm gold layer on top of a 200 nm $SiO_2$ layer on an Si(100) substrate; the gold structures were fabricated using EBL. Figure 1.10 (a) and (b) shows scanning electron microscope (SEM) micrographs of the investigated structures referred to as G and mirror-G shape respectively. Figure 1.10 (c) shows the unit cell components rearranged in a linear-G pattern; the gold regions in the micrograph are outlined in yellow. Each micrograph contains four unit cells, and each unit cell contains four G shaped structures. Plates (d), (e) and (f) show the SHG intensity of G, mirror-G and linear-G structures respectively in the far-field as a function of the elliptical polarisation produced by a quartier wave plate illuminated with linearly polarised light. The 45° and 225° rotation of the quarter wave plate produce right hand circular polarisation whereas the 135° and 315° produce left hand circular polarisation (from the point of view of the source). The G structures produce maximum SHG when illuminated by right handed light and the mirror-G structures produce maximum SHG when illuminated by left handed light. This shows SHG circular dichroism is a macroscopic property of the patterned surface. The linear-G structures produce the same SHG intensity for both right and left handed light. Valev *et al.* investigated the optical characteristics of the structure in the near-field using SHG microscopy (see Section 3.2.2). Near-field SHG intensity maps of the three structures are shown in plates (g) to (l). Plates (g), (h) and (i) correspond to right handed fundamental polarisation; plates (j), (k)

and (l) correspond to left hand fundamental polarisation. SHG hotspots are visible in all six plates as yellow and red regions. The SHG distribution in the near-field is dependent on the handedness of both the structure and the incident light as would be expected from the far-field measurements of circular dichroism. The near-field intensity maps show a distinct change in the SHG distribution for the G and mirror-G structures, with G structures producing a central hotspot when illuminated by right handed fundamental and the mirror-G structures producing a similar SHG distribution when illuminated with left handed fundamental. The linear-G structures produce a SHG distribution which is independent of the handedness of incident light.

Following this work Valev *et al.* thoroughly investigated a series of structures using SHG microscopy, producing a rich body of work which was reviewed by Valev in 2012 [76]. In 2010 they found that the G structures produced circularly polarised light when illuminated with a linearly polarised fundamental [78]. In 2011 they observed the formation of lumps on the G patterned surface following its illumination with a linearly polarised fundamental [77]. Figure 1.11 (a) shows an SEM micrograph of the unit cell before SHG microscope imaging, (b) shows the near-field SHG intensity when the unit cell is illuminated with 800 nm linearly polarised fundamental and (c) shows the unit cell following SHG microscopy. In (c) there are four light areas that are not present in (a). (d) shows the unit cell relief mapped using an atomic force microscope (AFM), the light regions in (c) are higher than the surrounding metal film and are not charge artifacts. As the lumps are co-located with the near-field SHG hotspots it was thought that their origin was laser induced atomic desorption caused by the LSPs which form the hotspots.

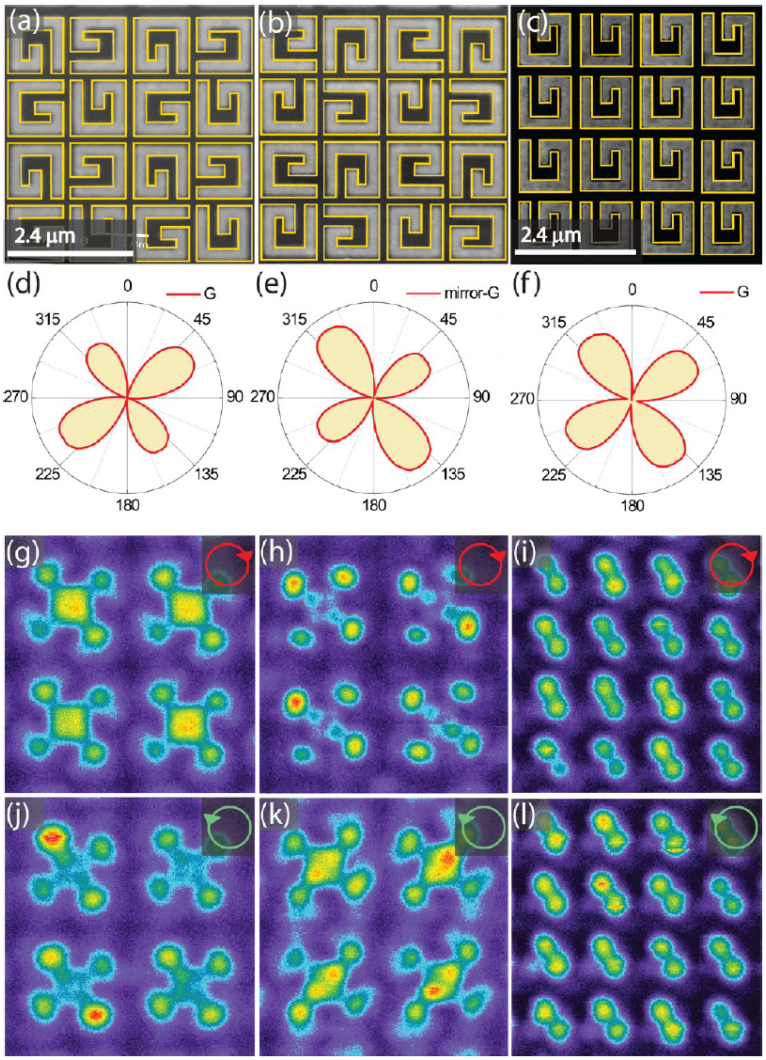


Figure 1.10: (a), (b) and (c) scanning electron microscope micrographs of G, mirror-G and linear-G patterns respectively, gold regions are outlined in yellow. (d), (e) and (f) the far-field SHG intensity as a function of quarter wave plate rotation. (g), (h) and (i) measured SHG microscope intensity maps where the structures were illuminated with right handed fundamental light, panels correspond to G, mirror-G and linear-G patterns respectively (the colour scale from low to high SHG intensity is purple, blue, green, yellow, red). (j), (k) and (l) measured SHG microscope intensity maps where the structures were illuminated with left handed fundamental light, panels correspond to G, mirror-G and linier-G patterns respectively. Figure reproduced from Valev [76], showing results from Valev *et al.* [75].

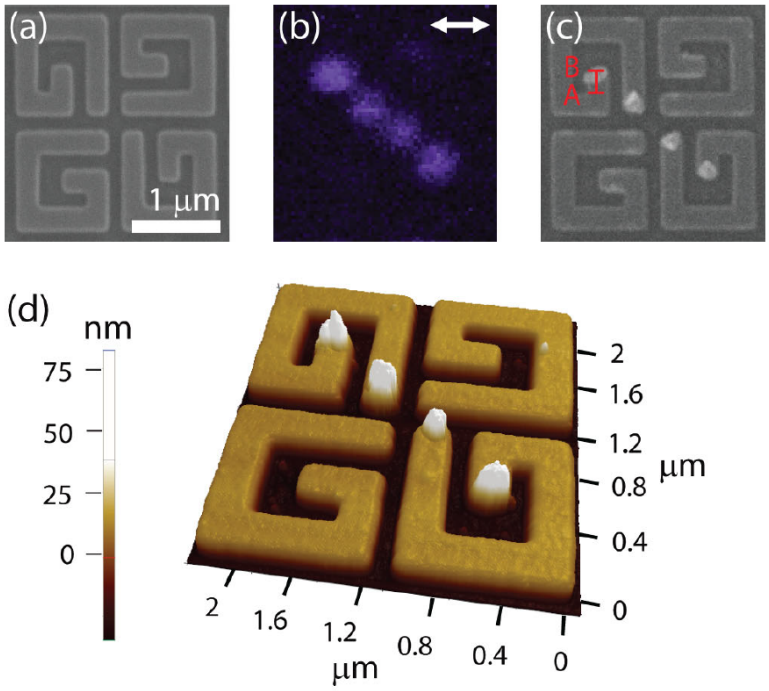


Figure 1.11: (a) SEM micrograph of the G unit cell before illumination. (b) SHG microscope near-field intensity map of the unit cell being illuminated by linearly polarised light (**E** field orientation shown by inset arrow). (c) SEM micrograph of the G unit cell following illumination. (d) AFM relief map of the unit cell surface. Figure reproduced from Valev *et al.* [77].

# Chapter 2

# Theoretical Introduction

This work investigates the enhanced fields which form when light couples to electrons in a subwavelength aperture in a metallic film or to electrons in subwavelength metallic strips.

The mechanism by which light is able to couple to a metallic film covered with periodic subwavelength apertures is reviewed by a number of authors including Weiner [79], Maier [80] and Novotny and Hecht [81]. As subwavelength apertures in opaque dielectric films do not allow extraordinary optical transmission, the sea of free electrons present in a metal have been cited as playing a critical role in the phenomenon [1]. We therefore present the Drude model of the motion of electrons in a metal which can be used to explain some of the optical characteristics of a metallic surface. This is followed by a mathematical explanation of the coupling of light incident upon the metal surface to a propagating density wave of electrons on the surface of the metal, the surface plasmon polariton (SPP). Following this we discuss the localisation of the electrons in a bound geometry, the localised surface plasmon.

The Fano resonance is key to describing measurements of the reflection,

transmission and absorption of the plasmonic structure when it interacts with a discrete resonance. We therefore describe the origin of the Fano resonance and discuss its characteristics. The formation of the resonance is then elaborated using a mathematical description of a classical mechanical oscillator system.

Finally the rigorous coupled-wave analysis method of grating simulation used in the design of the investigated plasmonic system is briefly outlined.

## 2.1 Drude Dielectric Function

Drude's model for the motion of an electron in a metal applies the kinetic theory of gases to electrons, assuming that electrons are free to move in a material which has positive charge located in immobile positive particles [82, 83]. The Drude model for the average motion of an electron in the presence of a driving force caused by a spatially uniform electric field $\mathbf{E}$ is

$$\frac{d}{dt}\mathbf{p}(t) = -\frac{\mathbf{p}(t)}{\tau} - e\mathbf{E}(t) \tag{2.1}$$

where $\mathbf{p}$ is the electron's momentum, $\tau$ is the relaxation time (*i.e.* the average time elapsed from the last electron collision) and $e$ is the electron charge. As electrons have mass $m_e$ the momentum $\mathbf{p}(t) = m_e\mathbf{v}(t) = m_e\frac{d}{dt}\mathbf{r}(t)$. Putting $\Gamma = 1/\tau$ we can write

$$m_e\frac{d^2}{dt^2}\mathbf{r}(t) = -m_e\frac{d}{dt}\mathbf{r}(t)\Gamma - e\mathbf{E}(t) \tag{2.2}$$

If the electric field is of amplitude $\mathbf{E}_0$ oscillating with angular frequency $\omega$, then this may be written as

$$m_e \frac{d^2}{dt^2}\mathbf{r}(t) + m_e \frac{d}{dt}\mathbf{r}(t)\Gamma = -e\mathbf{E}_0 \mathrm{e}^{-i\omega t} \tag{2.3}$$

A solution for this equation is $\mathbf{r}(t) = \mathbf{r}_0 \mathrm{e}^{-i\omega t}$. Inserting this into (2.3) and solving results in

$$\mathbf{r}_0 = \frac{e}{m_e(\omega^2 + i\Gamma\omega))}\mathbf{E}_0 \tag{2.4}$$

This equation shows the oscillation amplitude $\mathbf{r}_0$ which contributes to the macroscopic polarisation $\mathbf{P}$ of the electrons in the metal. $\mathbf{P}$, the dipole moment per unit volume, is related to the oscillation amplitude by $\mathbf{P} = -ne\mathbf{r}_0$ where $n$ is the number of electrons of charge $e$. This term is related to the electric displacement $\mathbf{D}$ from Maxwell's equations for an isotropic, linear material

$$\mathbf{D} = \epsilon_0\mathbf{E} + \mathbf{P} = \epsilon_0\epsilon\mathbf{E} \tag{2.5}$$

where $\epsilon_0$ is the permittivity of free space and $\epsilon$ is the relative permittivity of the metal [84]. Hence

$$\mathbf{P} = -\frac{ne^2}{m_e(\omega^2 + i\Gamma\omega)}\mathbf{E}_0 \tag{2.6}$$

Taking this expression for the polarisation we can rewrite (2.5) as

$$\mathbf{D} = \epsilon_0\mathbf{E} - \frac{ne^2}{m_e(\omega^2 + i\Gamma\omega)}\mathbf{E}_0 \tag{2.7}$$

The plasma frequency of a free electron gas is defined by the relation $\omega_p^2 \equiv ne^2/\epsilon_0 m_e$ [85]. We can therefore rewrite (2.7)

$$\mathbf{D} = \epsilon_0 \mathbf{E}_0 \left( 1 - \frac{\omega_p^2}{(\omega^2 + i\Gamma\omega)} \right) \tag{2.8}$$

Using $\mathbf{D} = \epsilon_0 \epsilon \mathbf{E}$ from (2.5) we can produce a complex term for the relative permittivity of the metal

$$\epsilon(\omega) = 1 - \frac{\omega_p^2}{(\omega^2 + i\Gamma\omega)} \tag{2.9}$$

This is the Drude dielectric function. It can be split into real and imaginary parts in the form $\epsilon(\omega) = \epsilon_1(\omega) + i\epsilon_2(\omega)$ as follows

$$\epsilon(\omega) = 1 - \frac{\omega_p^2}{\omega^2 + \Gamma^2} + i\frac{\Gamma\omega_p^2}{\omega(\omega^2 + \Gamma^2)} \tag{2.10}$$

The Drude dielectric function may be used to interpret the dispersive optical response of a metal. Figure 2.1 shows the real and imaginary parts of (2.10) calculated using values for gold: $\hbar\omega_p = 8.95$ eV and $\hbar\Gamma = 65.8\times10^{-3}$ eV [86].

The refractive index of a material

$$n = \sqrt{\epsilon\mu} \tag{2.11}$$

where $\epsilon$ and $\mu$ are the relative permittivity and relative permeability respectively. For most materials $\mu$ is close to unity and the refractive index is therefore dependent upon the dielectric function. We see from Figure 2.1 that the real part of (2.10) is negative. The refractive index calculated using (2.11) will therefore have a large imaginary part, implying that light can only penetrate a small distance into the metal. More qualitatively, the

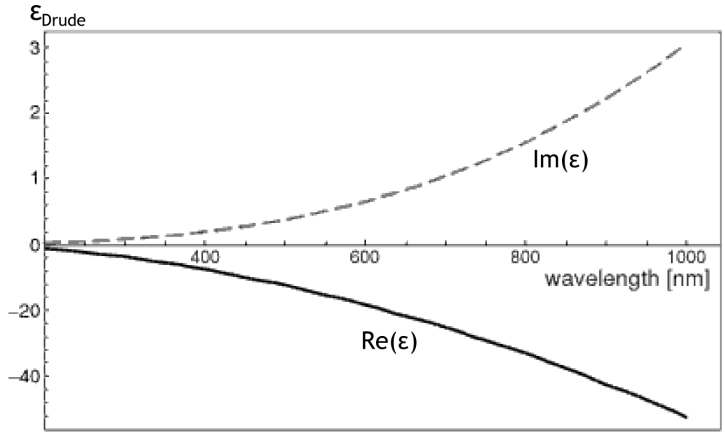


Figure 2.1: The real and imaginary parts of the dielectric constant for gold calculated using the Drude model. Reproduced from Novotny and Hecht [86].

dissipation of energy by electrons in a metal is related to the imaginary part of $\epsilon$. When there is a large dissipation of electron energy in a metal light can only travel a small distance into it as the energy of the light is transferred to electron motion.

## 2.2 Surface Plasmon Polaritons

The magnetizing field $\mathbf{H}$ in a nonmagnetic, isotropic linear material is related to the electric displacement field $\mathbf{D}$ in the material by the following Maxwell equation

$$\nabla \times \mathbf{H} = \frac{\partial \mathbf{D}}{\partial t} \tag{2.12}$$

and the constitutive relations

$$\mathbf{H} = \frac{1}{\mu_0}\mathbf{B} \qquad \mathbf{D} = \epsilon\epsilon_0\mathbf{E} \tag{2.13}$$

A polarised electromagnetic wave incident at arbitrary angle on a surface

described by the $x$ $y$ plane and having only **H** field component $H_y$ will have **E** field components $E_x$ and $E_z$ (see Figure 2.2). This wave is refered to as a transverse magnetic (TM) wave because the magnetic field is aligned perpendicular to the plane of incidence. A transverse electric (TE) wave has the electric field aligned perpendicular to the plain of incidence. We will consider TM polarised light only as it has been shown that TE surface waves cannot exist because for them to do so would require a magnetic charge [87]. The wave may also be described using momentum components $k_x$ and $k_z$.

$$\begin{aligned} E_x &= E_{0x}\mathrm{e}^{i(k_x x + k_z z - \omega t)} \\ E_z &= E_{0z}\mathrm{e}^{i(k_x x + k_z z - \omega t)} \\ H_y &= H_{0y}\mathrm{e}^{i(k_x x + k_z z - \omega t)} \end{aligned} \tag{2.14}$$

This wave travels through a space consisting of a non dispersive dielectric material in the region $z < 0$ and a metal with dispersive dielectric function in the region $z > 0$.

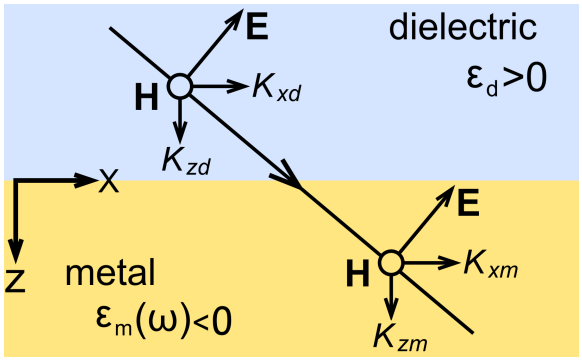


Figure 2.2: A transverse magnetic polarised electromagnetic wave travelling from a non-dispersive dielectric with positive real dielectric constant to a dispersive metal with a negative dielectric constant.

The continuity conditions at the dielectric metal interface are

$$E_{xd} = E_{xm}, \qquad \epsilon_d E_{zd} = \epsilon_m E_{zm}, \qquad H_{yd} = H_{ym} \tag{2.15}$$

where the subscripts $d$ and $m$ denote dielectric and metal respectively. For this electromagnetic wave polarisation (2.12) becomes

$$\nabla \times \mathbf{H} = \widehat{\mathbf{x}} \left( -\frac{\partial H_y}{\partial z} \right) + \widehat{\mathbf{z}} \left( -\frac{\partial H_y}{\partial x} \right) = \widehat{\mathbf{x}} \left( \frac{\partial D_x}{\partial t} \right) + \widehat{\mathbf{z}} \left( \frac{\partial D_z}{\partial t} \right) \tag{2.16}$$

We initially consider the dielectric material half space. The $\widehat{\mathbf{x}}$ and $\widehat{\mathbf{z}}$ components from (2.16) are written separately and (2.13) is introduced producing

$$-\frac{\partial H_{yd}}{\partial z} = \frac{\partial D_{xd}}{\partial t} = \epsilon_d \frac{\partial E_{xd}}{\partial t} \qquad \text{and} \qquad \frac{\partial H_{yd}}{\partial x} = \frac{\partial D_{zd}}{\partial t} = \epsilon_d \frac{\partial E_{zd}}{\partial t} \tag{2.17}$$

Solving these two equations after substituting in the field components for the electromagnetic wave (2.14) produces the following expressions for the electric field components in the dielectric half space

$$E_{0xd} = \frac{H_{yd} k_{zd}}{\epsilon_d \omega} \qquad \text{and} \qquad -E_{0zd} = \frac{H_{yd} k_{xd}}{\epsilon_d \omega} \tag{2.18}$$

Following the same procedure for the metallic half space produces the following expressions for the electric field components in that region

$$E_{0xm} = -\frac{H_{ym} k_{xm}}{\epsilon_m \omega} \qquad \text{and} \qquad -E_{0zm} = -\frac{H_{ym} k_{xm}}{\epsilon_m \omega} \tag{2.19}$$

At the boundary between the dielectric and metal half spaces the continuity conditions (2.15) indicate that the $E_{0x}$ expressions from (2.18) and (2.19) are equal. Equating these two expressions and writing the continuity condition for $H$

$$\begin{aligned} \tfrac{H_{yd} k_{zd}}{\epsilon_d \omega} + \tfrac{H_{ym} k_{zm}}{\epsilon_m \omega} &= 0 \\ H_{yd} - H_{ym} &= 0 \end{aligned} \tag{2.20}$$

we see that these expressions are coupled and will only have nontrivial so-

lutions if

$$\frac{k_{zd}}{\epsilon_d \omega} = -\frac{k_{zm}}{\epsilon_m \omega} \tag{2.21}$$

An electromagnetic wave has momentum $k(\omega) = \frac{\omega}{c}\sqrt{\epsilon(\omega)}$. The momenta $\mathbf{k}_d$ and $\mathbf{k}_m$ in the dielectric and metal respectively (see Figure 2.2) are therefore

$$k_{xd}^2 + k_{zd}^2 = \left(\frac{\omega}{c}\right)^2 \epsilon_d \tag{2.22}$$

and

$$k_{xm}^2 + k_{zm}^2 = \left(\frac{\omega}{c}\right)^2 \epsilon_m \tag{2.23}$$

As momentum is conserved following the waves passage from the dielectric to the metal $|\mathbf{k}_d|^2$ is equal to $|\mathbf{k}_m|^2$. Rearranging equation (2.22) for $k_{zd}^2$ and (2.23) for $k_{zm}^2$, dividing these two equations and substituting equation (2.21) to express $k_{zd}/k_{zm}$ in terms of $\epsilon_d$ and $\epsilon_m$ leads to

$$k_x = \left(\frac{\omega}{c}\right)\sqrt{\frac{\epsilon_d \epsilon_m}{\epsilon_d + \epsilon_m}} \tag{2.24}$$

This is the experssion for the propagation parameter of the SPP wave, $k_{SP}$. Figure 2.3 shows the dispersion curve given by (2.24) at the boundary between the dielectric and perfect metal half spaces and the dispersion curve of light in the dielectric half space. In a perfect metal $\epsilon_m$ is the real part of the Drude dielectric function and losses produced by electron scattering in a real metal, represented by the imaginary part of (2.10), are not taken into accont. The two dispersion curves do not cross and $k_{SP}$ is always greater than the wave vector of light $k = \omega/c$ in the adjacent dielectric. It is therefore impossible for light to couple directly to the SPP. This is because the $x$ component of the momentum of photons incident on the surface, $k_{xd}$, is always smaller than $k_{SP}$, prohibiting phase-matching.

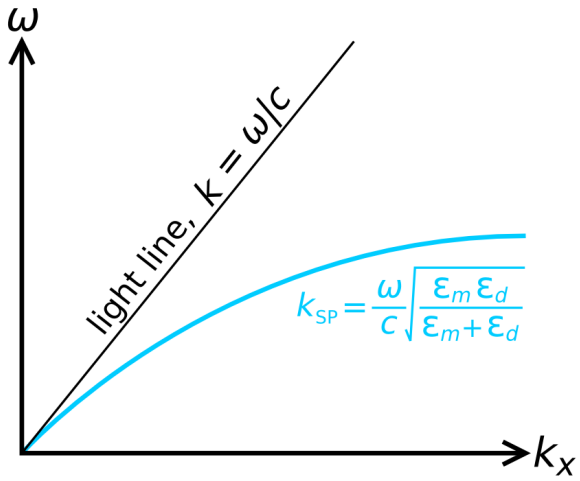


Figure 2.3: Dispersion curve of the surface plasmon polariton wave propagating at the interface between dielectric and metal half spaces. The light line shows the dispersion curve of a photon in the dielectric half space.

In order for the SPP to be excited, phase matching of the incident light and the SPP must be achieved. There are a number of methods which allow phase matching including prism coupling and the structuring of surfaces [88]. An example of phase matching using a structured surface is the grating coupling. The surface of a metal film is patterned with a periodic array of grooves, shown schematically in Figure 2.4. Phase matching occurs whenever

$$k_{SP} = k_d \sin\theta \pm ng \tag{2.25}$$

where $n$ is an integer and $g = 2\pi/a$ is the reciprocal vector of the grating.

SPPs are propagating density waves of the electron plasma of a conductor. They are confined to the interface between a conductor and a dielectric and they are dispersive. There is another plasmonic excitation that needs to be considered - the localised surface plasmon, which will be discussed in the following section.

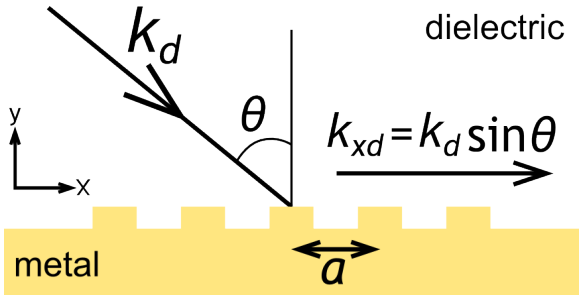


Figure 2.4: Light with wave vector $k_d$ incident upon a metal grating with lattice constant $a$.

## 2.3 Localised Surface Plasmons

The localised surface plasmon (LSP) is a non-propagating excitation of the electron plasma in a bound geometry [89]. Bound geometries take the form of metal particles or voids in metallic structures, the size and shape of which determine the resonant frequencies of the supported LSP [90]. When light of appropriate frequency and polarisation is incident upon a particle or void an LSP is excited irrespective of the wave vector of the incident light; LSPs therefore decay with the emission of light [91]. In the following section we will derive the condition for resonance of a dipole LSP and show that this resonance is sensitive to the refractive index of the dielectric surrounding the metallic structure. This sensitivity of LSP resonances to refractive index is observed in the investigated structures, *e.g.* in Figure 4.12.

To demonstrate the resonant frequency of an LSP we consider a metallic sphere with radius $a$ in a uniform static electric field, $\mathbf{E} = E_0\hat{\mathbf{x}}$, as shown in Figure 2.5. If the characteristic size of the particle $d \leq \lambda/(4\pi\sqrt{\epsilon})$ (the skin depth of the metal) then all parts of the particle oscillate in phase and the electrostatic approximation may be used. To calculate the resonance we must then solve Laplace's equation $\nabla^2\Phi = 0$. We first write the Laplace

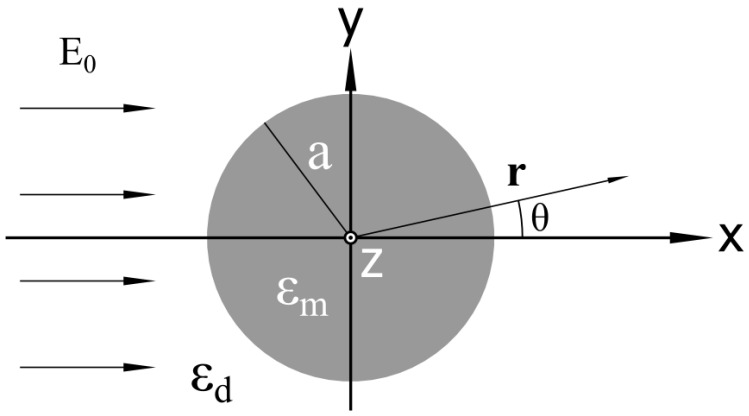


Figure 2.5: Homogeneous metallic sphere with radius $a$ in a uniform electrostatic field $E_0$. $\theta$ is the angle between the position vector $\mathbf{r}$ and the $x$ axis.

operator in spherical coordinates

$$\nabla^2 \equiv \frac{1}{r^2}\frac{\partial}{\partial r}\left(r^2\frac{\partial}{\partial r}\right) + \frac{1}{r^2\sin\theta}\frac{\partial}{\partial\theta}\left(\sin\theta\frac{\partial}{\partial\theta}\right) + \frac{1}{r^2\sin^2\theta}\frac{\partial^2}{\partial\varphi^2} \tag{2.26}$$

As a result of the symmetry of the applied electric field and the metallic sphere the solution is independent of the azimuthal angle $\varphi$ and the general solution is

$$\Phi(r,\theta) = \sum_{l=0}^{\infty}\left(A_l r^l + \frac{B_l}{r^{l+1}}\right)P_l^m(\cos\theta) \tag{2.27}$$

[84], where $P_l^m(\cos\theta)$ is an associated Legendre polynomial. As potentials must not go to infinity at the origin or at infinite distance the potentials inside the and outside the metallic sphere can be written as

$$\Phi_{in}(r,\theta) = \sum_{l=0}^{\infty} A_l r^l P_l(\cos\theta) \tag{2.28}$$

and

$$\Phi_{out}(r,\theta) = \sum_{l=0}^{\infty}\left(B_l r^l + \frac{C_l}{r^{(l+1)}}\right)P_l(\cos\theta) \tag{2.29}$$

respectively. $\Phi_{out} = \Phi_{scatter} + \Phi_0$ where $\Phi_{scatter}$ is the potential scattered by the sphere and $\Phi_0$ is the potential at $r \to \infty$. As the incoming electric field is homogeneous and directed along the $x$ axis, $\Phi_0 = -E_0 x = -E_0 r P_1^0(\cos\theta)$. The boundary conditions at $r \to \infty$ and at the surface of the sphere $r = a$ are used to determine the coefficients $A_l$, $B_l$ and $C_l$. At the surface of the sphere equality of the tangential components of the electric field imply

$$\left.\frac{\partial \Phi_{in}}{\partial \theta}\right|_{r=a} = \left.\frac{\partial \Phi_{out}}{\partial \theta}\right|_{r=a} \tag{2.30}$$

and the equality of the normal components of the electric field displacement imply

$$\epsilon_m \left.\frac{\partial \Phi_{in}}{\partial r}\right|_{r=a} = \epsilon_d \left.\frac{\partial \Phi_{out}}{\partial r}\right|_{r=a} \tag{2.31}$$

The evaluation of coefficients when $l = 1$ leads to

$$\Phi_{in} = -E_0 r \cos\theta \frac{3\epsilon_d}{\epsilon_m + 2\epsilon_d} \tag{2.32}$$

$$\Phi_{out} = -E_0 r \cos\theta + \frac{\epsilon_m - \epsilon_d}{\epsilon_m + 2\epsilon_d} E_0 a^3 \frac{\cos\theta}{r^2} \tag{2.33}$$

The electric fields inside and outside the sphere can be calculated using the relation $E = -\nabla\Phi$

$$\mathbf{E}_{in} = E_0 \frac{3\epsilon_d}{\epsilon_m + 2\epsilon_d} (\cos\theta \hat{\mathbf{r}} - \sin\theta \hat{\boldsymbol{\theta}}) \tag{2.34}$$

$$\mathbf{E}_{out} = E_0(\cos\theta \mathbf{n}_r - \sin\theta \mathbf{n}_\theta) + \frac{\epsilon_m - \epsilon_d}{\epsilon_m + 2\epsilon_d} \frac{a^3}{r^3} E_0(2\cos\theta \hat{\mathbf{r}} + \sin\theta \hat{\boldsymbol{\theta}}) \tag{2.35}$$

The second term in 2.35 is equivalent to the electric field of a point electric dipole. The dipole moment $\mathbf{p} = \epsilon_d \alpha \mathbf{E}_0$ therefore allows us to determine the

polarisability of the sphere

$$\alpha = 4\pi\epsilon_0 a^3 \frac{\epsilon_m - \epsilon_d}{\epsilon_m + 2\epsilon_d} \tag{2.36}$$

There is an enhancement in the polarisability when $|\epsilon_m + 2\epsilon_d|$ is minimum. If the imaginary part of $\epsilon_m$ is small or changes slowly then this polarisability enhancement is achieved when

$$\mathrm{Re}\left[\epsilon_m(\omega)\right] = -2\epsilon_d \tag{2.37}$$

This is known as the Fröhlich condition. In an oscillating field the mode associated with this resonance is the dipole surface plasmon of the metallic sphere [89]. For larger spheres higher multipoles may also be excited, that is when $l > 1$ [91].

In a Drude metal, when the system is lightly damped the relaxation time is large so $\Gamma \to 0$, the real part of equation (2.10) may be used to find the frequency at which the Fröhlich condition is satisfied

$$\omega_0 = \frac{\omega_p}{\sqrt{2\epsilon_d + 1}} \tag{2.38}$$

As the relative permittivity of the dielectric increases, $\omega_0$ decreases, indicating a red shift of the resonance of the sphere. The resonance of a local surface plasmon is therefore sensitive to the refractive index in which the supporting metallic structure is placed, with an increase in refractive index causing the resonant wavelength of the structure to red shift.

## 2.4 The Fano Resonance

The asymmetric resonance formed during the autoionization of noble gases was first described mathematically by Fano [92, 23]. The distinctive asymmetric energy profile of electrons ejected from an atom during autoionization was shown by Fano to be the result of the interference occurring between two alternative mechanisms of excitation.

Although the subject of autoionization may at first appear extraneous, there is a universality in the Fano formula. This is because it describes an interference phenomenon that is indifferent to the nature of the constituting waves. Fano's asymmetric line shapes produced by the interaction of a narrow and broad resonance may be applied to many areas of physics, including plasmonic structures.

A complete derivation of the Fano resonance formula is beyond the scope of this thesis; for a detailed derivation see Fano's 1961 paper [23]. We will discuss the main result of this paper and give a qualitative description of its origin in the following section.

### 2.4.1 The Fano Formula

There are a number of ways that an atom can ionize; two of the mechanisms are photoionization and autoionization [93]. Photoionization occurs when a photon excites an electron from a bound state to an energy above the ionization threshold of an atom, causing the electron to enter the continuum. The photoionization mechanism may be represented by $A + \hbar\nu \rightarrow A^+ + e$. Autoionization may occur if a photon excites an electron into a bound state of an atom which has an energy greater than the first ionizing energy. This results in an excited atom that may spontaneously ionize by ejecting the excited electron into the continuum. The autoionization mechanism is

represented by $A + \hbar\nu \rightarrow A^* \rightarrow A^+ + e$. Figure 2.6 shows the two ionization paths schematically. There are two distinct paths form the initial bound state $|i\rangle$ that will result in the ejection of the exited electron into the unperturbed continuum $|\psi_E\rangle$, one direct and one via the discrete state $|e\rangle$. The superposition principle of quantum mechanics states that the total probability of ionization is given by the interference of the two wavefunctions which describe the two alternative paths.

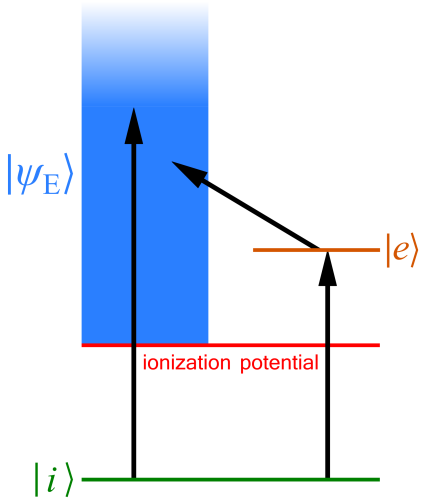


Figure 2.6: Energy level schematic showing two atomic ionization routes where an electron moves from the initial bound state $|i\rangle$ to the continuum of states $|\psi_E\rangle$. The first route is direct ionisation; the second is autoionisation via the discrete state $|e\rangle$.

Fano used perturbation of the continuum to describe a stationary state $\Psi_E$ which is a configuration that contains a mixture of a modified discrete state above the first ionization level, $\Phi$, and the unperturbed continuum of states $\psi_E$. Fano saw that, irrespective of the excitation mechanism the probability of the transition from a bound state $i$ to the continuum (either perturbed or unperturbed), the probability of excitation may be represented by a transition operator $T$. The Fano line shape is the ratio of the transition

probability along the path through the discrete state to the continuum and the path direct to the continuum. This ratio forms a family of curves that make up the Fano resonance and are represented by

$$\sigma = \frac{|\langle \Psi_E | T | i \rangle|^2}{|\langle \psi_E | T | i \rangle|^2} = \frac{(q+\epsilon)^2}{1+\epsilon^2} \tag{2.39}$$

where

$$\epsilon = 2(E - E_0)/\Gamma \tag{2.40}$$

Here $q$ is interpreted as an asymmetry parameter which Fano gave as the ratio of $\Phi$ and $\psi_E$. $E_0$ the energy of the autoionization state and $\Gamma$ its the state's spectral width. $E$ is the energy of a stationary state formed by the mixing of the discrete state and the continuum. Figure 2.7 shows the line shapes produced by Equations (2.39) and (2.40) when constants $E_0$ and $\Gamma$ are both equal to one and $q$ is varied such that $q = 0,\ 0.5,\ 1,\ 1.5,\ 2$. When $q = 0$ there is no transition to the discrete state and the resonance has a symmetrical dip which reaches a minimum at $E_0$; this is referred to as an antiresonance. When the ratio of the two transition probabilities to the continuum is unity, $q = 1$ and the line shape is at its most asymmetric; there is a dip in the resonance when $E < E_0$ and a peak when $E > E_0$. As the transition to the continuum becomes less probable $q$ increases and the line shape moves towards that of a discrete resonance centred on $E_0$.

The asymmetry of the resonance profile with increasing $q$ may be illustrated with the normalised Fano profile

$$\sigma_{norm} = \frac{\sigma}{1+q^2} = \frac{1}{1+q^2}\frac{(q+\epsilon)^2}{1+\epsilon^2} \tag{2.41}$$

Figure 2.8 plots $\sigma_{norm}$ when $E_0 = 1$ and $\Gamma = 1$ for three $q$ values. When

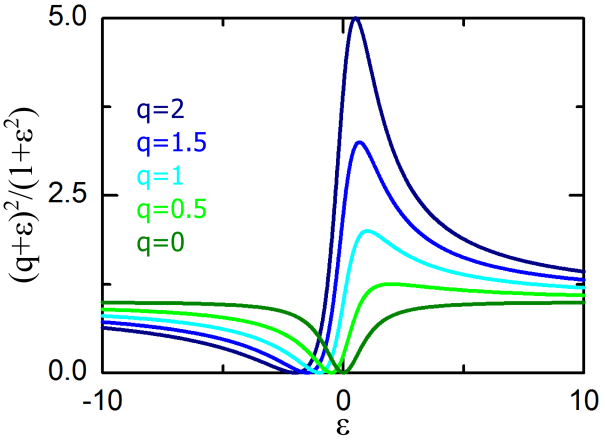


Figure 2.7: Plot of Equation (2.39) showing the Fano line shape formed for different values of $q$ when $E_0 = \Gamma = 1$.

$q = 0$ the symmetric antiresonance is formed (green). When $q = 1$ the characteristic asymmetric line shape is formed (blue). As $q \to \infty$ the transition to the continuum tends to zero and the Lorentzian profile of an unperturbed discrete state is formed.

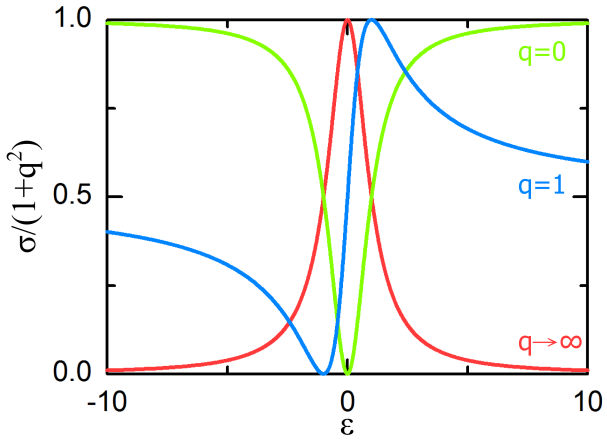


Figure 2.8: The normalised Fano profile (Equation 2.41) when $q = 0,\ 1$ and $q \to \infty$, constants $E_0 = \Gamma = 1$.

The Fano line shape has been described qualitatively. It is apparent from Figure 2.8 that the Fano profile is able to produce both symmetric and

asymmetric curves. The profile may be used to characterise the interference of a two-channel mechanism of excitation. Also, as the resonance is based on the interference of waves it is applicable to many physical systems apart from autoionization. This will be discussed in the next section where we consider the Fano resonance produced by a classical damped oscillator system.

### 2.4.2 Classical Analogue

The Fano resonance may be produced by classical systems, for example coupled harmonic oscillators [34]. As in the quantum system a narrow resonance (the discrete state) is coupling to a broad resonance (the continuum). The line shape produced by this classical system has been shown to be equivalent to that produced by Fano's quantum system by Gallinet and Martin [32] who applied both models to plasmonic nanostructures. To demonstrate this system, which will later be used to interpret experimental results, we begin by showing the showing the equation of motion of a single harmonic oscillator.

Figure 2.9 (a) shows a damped harmonic oscillator represented by a ball attached to two immovable walls by massless springs. The ball moves under the influence of a linear restoring force, experiences viscous damping proportional to its velocity given by coefficient $\gamma$ and has a natural frequency $\omega_0$. The ball is forced to vibrate by an external harmonic driving force of amplitude $F$ and frequency $\omega$. The displacement $x$ of the ball from its equilibrium position at time $t$ is described by the following differential equation

$$\ddot{x} + \gamma\dot{x} + \omega_0^2 x = F\cos\omega t \tag{2.42}$$

Using Euler's formula the driving force may be rewriten in complex form $f(\mathrm{e}^{i\omega t} + \mathrm{e}^{-i\omega t})$ where $f = F/2$. The solutions of Equation (2.42) contain

both positive and negative frequencies. As only positive frequencies are of interest we can neglect the $e^{-i\omega t}$ solution and write

$$\ddot{x} + \gamma\dot{x} + \omega_0^2 x = f e^{i\omega t} \tag{2.43}$$

It is apparent that Equation (2.43) has solution $x(t) = je^{i\omega t}$. After inserting this solution, differentiating and rearanging we find the complex amplitude

$$j(\omega) = \frac{f}{(\omega_0^2 - \omega^2) + (i\gamma\omega)} \tag{2.44}$$

The modulus of $j(\omega)$ gives the displacement of the ball

$$|j(\omega)| = \frac{f}{\sqrt{(\omega_0^2 - \omega^2)^2 + (\gamma\omega)^2}} \tag{2.45}$$

The phase of the oscillator with respect to the driving force, $\phi(\omega)$, is the argument of $j(\omega)$ which may be calculated thus

$$\phi(\omega) = \begin{cases} \tan^{-1}(\frac{\gamma\omega}{\omega_0^2 - \omega^2}) & \omega < \omega_0 \\ \pi + \tan^{-1}(\frac{\gamma\omega}{\omega_0^2 - \omega^2}) & \omega > \omega_0 \end{cases} \tag{2.46}$$

Figure 2.9 (b) shows the ball's displacement (green) and its phase with respect to the driving force (orange). The plotted displacement and phase are calculated by Equations (2.45) and (2.46) respectively when constants $\omega_0 = 10$, $\gamma = 0.04$ and $f = 1$ are used. The oscillator displacement is maximised when $\omega = \omega_0$. The large displacement of the ball is explained by its phase with respect to the driving force which moves from zero to $\pi$. As the phase reaches $\phi = \pi/2$ the largest displacement of the oscillator by the driving force is achieved; this occurs at the natural frequency of the oscilator.

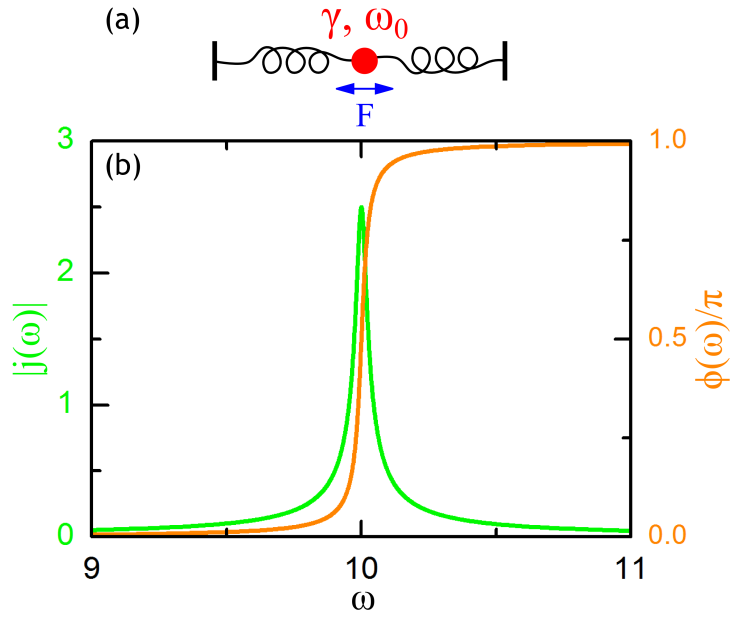


Figure 2.9: (a) Schematic showing the single mechanical oscillator system. (b) The amplitude $|j(\omega)|$ and phase $\phi(\omega)/\pi$ of the oscillator shown in (a) are plotted

We now introduce a second ball into the system. Figure 2.10 (a) shows the ball and spring system with the addition of a second ball and a third spring. The two balls are denoted $a$ and $b$ and are attached to the immovable walls by two independent massless springs and to each other by the third spring. The balls therefore have independent natural frequencies $\omega_a$ and $\omega_b$ and damping coefficients $\gamma_a$ and $\gamma_b$. The equations of motion of the two oscillators are produced by adding a coupling term $\kappa_{ab}$, which is dependent on the third spring, to Equation (2.43). Ball $a$ is driven by forced vibrations $\mathrm{F}_a = f_a \mathrm{e}^{i\omega t}$, and ball $b$ is purely excited by coupling to ball $a$.

The equations of motion of the two ball system are

$$\begin{aligned} \ddot{x}_a + \gamma_a \dot{x}_a + \omega_a^2 x_a + \kappa_{ab} x_b &= f_a \mathrm{e}^{i\omega t} \\ \ddot{x}_b + \gamma_b \dot{x}_b + \omega_b^2 x_b + \kappa_{ab} x_a &= 0 \end{aligned} \tag{2.47}$$

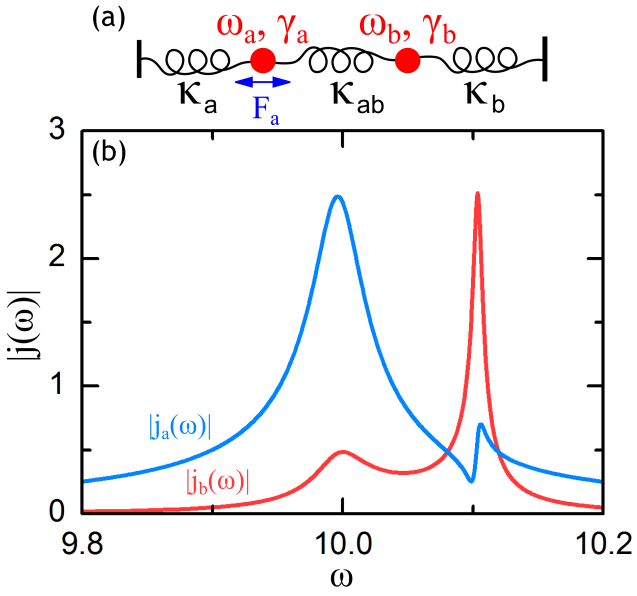


Figure 2.10: (a) Schematic showing two coupled mechanical oscillators $a$ and $b$. (b) The amplitudes $|j_a(\omega)|$ and $j_b(\omega)$ of the two oscillators shown in (a) are plotted.

We insert the solutions $x_a(t) = j_a e^{i\omega t}$ and $x_b(t) = j_b e^{i\omega t}$ into 2.47, differentiate and rearrange to

$$\begin{aligned} j_a\left(\omega_a^2 - \omega^2 + i\omega\gamma_a\right) + \kappa_{ab} j_b &= f_a \\ \kappa_{ab} j_a + j_b\left(\omega_b^2 - \omega^2 + i\omega\gamma_b\right) &= 0 \end{aligned} \tag{2.48}$$

The complex amplitudes of the oscillators displacement may be found by applying Cramer's rule [94, 95] and are

$$j_a = \frac{f_a(\omega_b^2 - \omega^2 + i\omega\gamma_b)}{(\omega_a^2 - \omega^2 + i\omega\gamma_a)(\omega_b^2 - \omega^2 + i\omega\gamma_b) - \kappa_{ab}^2} \tag{2.49}$$

and

$$j_b = \frac{f_a\kappa_{ab}}{(\omega_a^2 - \omega^2 + i\omega\gamma_a)(\omega_b^2 - \omega^2 + i\omega\gamma_b) - \kappa_{ab}^2} \tag{2.50}$$

Figure 2.10 (b) shows the displacement of the balls $a$ (blue) and $b$ (red) in

the case $\omega_a = 10$, $\omega_b = 10.1$, $\gamma_a = 0.04$, $\gamma_b = 0.006$, $F_a = 1$ and $\kappa_{a,b} = 0.4$. The balls now have two distinct eigenmodes at approximately $\omega_a$ and $\omega_b$ (there is a small shift from the natural frequency of two independent balls which is caused by their coupling). The displacement of ball $a$ contains a similar global resonance to that seen in Figure 2.9 (b). There is an additional feature that appears close to the natural frequency of ball $b$. This has the characteristic asymmetric Fano line shape. The displacement of ball $b$ shows two eigenmodes - there is a local maximum close to $\omega_a$ and a global maximum close to $\omega_b$.

The resonant characteristics of the two balls may be better understood by calculating their phases. As in the single ball case, the phases of the two balls, $\phi_a(\omega)$ and $\phi_b(\omega)$, are the arguments of the corresponding complex amplitudes, $j_a(\omega)$ and $j_b(\omega)$. Figure 2.11 shows the phase of ball $a$ (blue) and ball $b$ (red) relative to the driving force. Ball $b$ shows similar behaviour to the single oscillator case, with the displacement maxima shown in Figure 2.10 occurring when the driving force and oscillator are $\pi/2$ out of phase. Ball $a$ shows the same phase characteristics at frequency $\omega_a$, corresponding to the global maximum seen in Figure 2.10. However, at frequencies close to $\omega_b$ the phase of ball $a$ changes rapidly. This corresponds to the position of the asymetric resonance seen in Figure 2.10.

The rapid phase change and asymmetric amplitude is observed when the driving frequency is close to $\omega_b$ because ball $a$ is effectively being driven by two competing forces. The first force is the external driving force. The second force is that which is exerted by the momentum of ball $b$ and applied to ball $a$ through the coupling spring. At driving frequencies smaller than $\omega_b$ ball $b$ is damping ball $a$, when driving frequencies are higher than $\omega_b$ ball $b$ excites ball $a$; it is this constructive and destructive interference effected

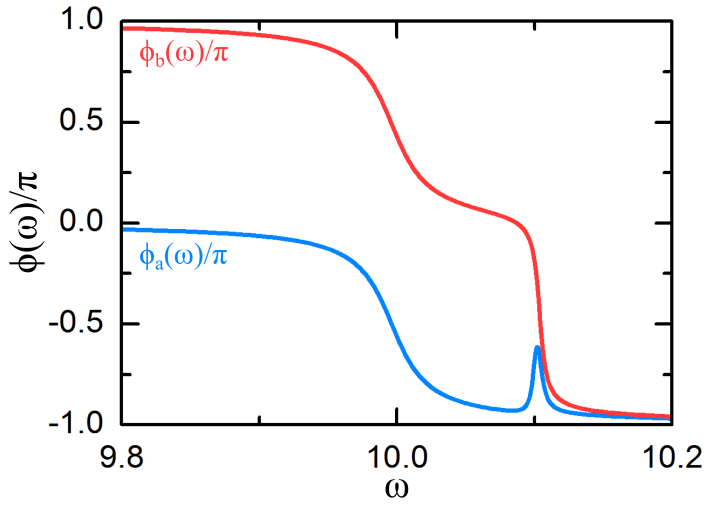


Figure 2.11: Phase of ball $a$ and ball $b$. The system is shown in Figure 2.10 (a).

by the superposition of the two driving forces that produces the asymmetric resonance. The phase change characteristics shown in Figure 2.11 always occur in the driving oscillator even if the damping of both balls is equivalent, although the asymmetric resonance only becomes discernible when the damping of ball $b$ is lower than the damping of ball $a$.

In this section we have seen how the amplitude of a driven oscillator will follow an asymmetric line shape when it is coupled to a second undriven oscillator. The asymmetric resonance is produced by the interference of resonances which is independent of the medium in which these resonances form. This universality of interference allows such a mechanical system to be used to model more complex physical systems which contain a coupled interaction of broad and narrow resonances. This has allowed the mechanical system to be applied to the modeling of plasmonic systems, *e.g.* dolmen-type plasmonic structures [32] and plasmonic nanoclusters [96].

## 2.5 The Rigorous Coupled-Wave Analysis Method

Numerical simulations are used during the initial design of the structures to predict the reflection, transmission, absorption and field distribution of different sized geometries. Here we adumbrate the method used in the numerical simulation.

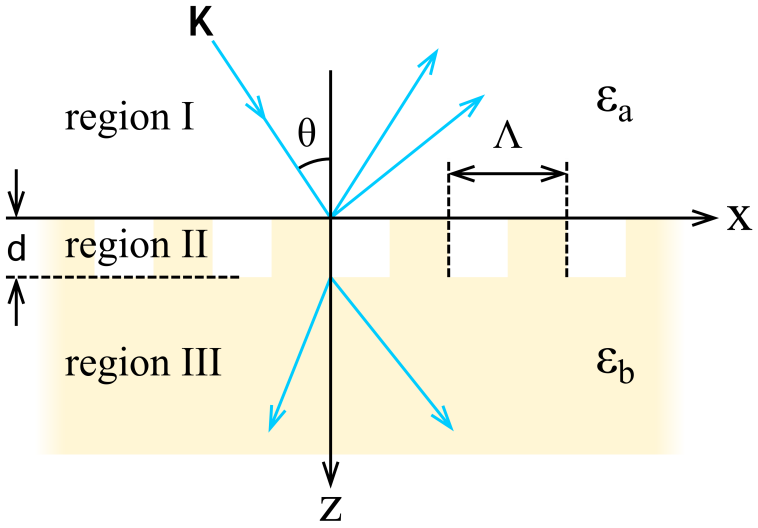


Figure 2.12: Schematic of a two dimensional grating that can be analysed using RCWA. Incoming plane wave **K** and forward and backward diffracted waves are shown in blue.

Rigorous coupled-wave analysis (RCWA) was first applied to metallic gratings by Moharam and Gaylord [97]. They considered a two dimensional periodic metallic rectangular-groove grating illuminated with polarised light. Figure 2.12 shows the grating schematically. The grooves are of depth $d$ and pitch $\Lambda$ and the incident light has wave vector **K**. The two dimensional space is split into three regions. Region I constitutes the space above the grating, region II the grating itself and region III the space below the grating. Region I is a homogeneous dielectric with permittivity $\epsilon_a$ and region III is a homogeneous material with complex permittivity $\epsilon_b$. Region II contains

a periodic distribution of the two materials that make up the grating. As the grating is periodic the permittivity of region II $\epsilon_p$ may be described as a function of $x$ and $z$ by a Fourier series

$$\epsilon_g(x,z) = \epsilon(x+\Lambda,z) = \sum_n \epsilon_{g,n}(z)\mathrm{e}^{in(2\pi/\Lambda)x} \tag{2.51}$$

The RCWA method calculates the total electric field in the three regions that make up the space. The total electric field in region I, $E_I$, is calculated as the sum of the incident and backwards diffracted waves. Similarly the total electric field in region III, $E_{III}$, is calculated as the sum of forward diffracted waves. In the grating region, the field $E_{II}$ is expressed in terms of spatial harmonic components that are allowed by the periodic grating structure. The components that make up $E_{II}$ are matched to the diffraction orders allowed in regions I and III, constraining the electric fields in the region II. $E_{II}$ must also satisfy the wave equation

$$\nabla^2 E_{II} + k^2 \epsilon_p E_{II} = 0 \tag{2.52}$$

The wave equation is dependent on $E_{II}$, which is coupled to $E_I$ and $E_{III}$,and also on the permittivity of region II ($\epsilon_p$), which is a function of the grating period $\Lambda$. It is this coupled wave equation that may be solved to determine the electric field in regions I and III as a function of the incident light wave and the structure of the grating.

As the wave equation is dependent on $\epsilon_g$ it is apparent that the number of terms of the Fourier series $n$ in Equation (2.51) will affect the accuracy of the solution. This is accounted for in the technical implementation of RCWA by a harmonic parameter $M$ which is the total number of expansions of the finite sum. The number of diffraction orders $N$ determines the required number

of expansions, where $M = (2N+1)^2$. Increasing the diffraction orders leads to a more accurate result; however an increase also results in a substantial lengthening of computation time and we therefore cannot simply choose a very large number of $N$. As the sum will converge we choose the number of diffraction orders which produces a suitably small change in the simulation output. In the case of the simulations used in the design of the investigated structure the number of diffraction orders is eight which corresponds to 289 harmonics. An increase to nine diffraction orders typically changes the output by less than 5% [5].

The RCWA equations are solved at specific wavelengths of incident light to produce the reflection and transmission spectra of the grating. Absorption is then extracted from the calculated spectra using the relation $A = 1-T-R$.

The RCWA method is available in several software packages which can implement the method in three dimensions. We use commercially available software, DiffractMOD created by RSoft Design Group, as a design tool that can predict the transmission, reflection and absorption of our geometry before fabrication. We also use the software to predict the distribution of the enhanced electric field produced by the structures.

# Chapter 3

# Experimental Procedure and Apparatus

The fabrication methods used in this investigation are introduced in the first section. The two principal methods are focused ion beam milling and electron beam lithography.

The characterisation of the fabricated devices is introduced in the second section. Spectroscopic measurements of asymmetric cruciform apertures were made using Fourier transform infrared spectroscopy. Second harmonic generation microscopy was used to investigate the nonlinear behaviour of nano-patterned surfaces.

## 3.1 Fabrication

### 3.1.1 Substrate: calcium fluoride

For transmission measurements a substrate should be chosen that is chemically stable, transparent in the wavelength range of aperture transmission and allows metal to be deposited upon it. We aimed to investigate sub-

wavelength apertures that have resonance in the 1-10 $\mu$m range. Suitable substrate materials that transmit in this range include magnesium fluoride (which is birefringent), silicon (which has a high refractive index and therefore large reflective losses) and calcium fluoride (which is soft and therefore hard to polish flat).

Calcium fluoride ($CaF_2$) was chosen. It is transparent in the wavelength range 0.2 - 9 $\mu$m and has a refractive index ranging from 1.43 at 1 $\mu$m to 1.34 at 8.6 $\mu$m [98, 99].

$CaF_2$ windows prepared for ultra violet transmission were purchased in order to minimise surface roughness and ensure better surface regularity. The windows used measured 25 mm in diameter and were 1 mm thick. Before processing they were cleaned in an acetone bath, followed by an isopropyl alcohol bath and then a deionised water rinse.

### 3.1.2 Substrate: silicon/silicon dioxide

When making measurements of nonlinear optical processes an additional constraint is that the substrate must not contribute a nonlinear signal of its own. We aimed to measure second harmonic generated by a fundamental wavelength of 800 nm or 1 $\mu$m. Bulk silicon dioxide does not generate a second harmonic and is transparent in the wavelength range of interest. For reflection measurements silicon dioxide can be easily grown on a silicon wafer substrate by heating the wafer in an oxygen rich environment, producing a flat homogeneous surface. When making transmission measurements in the investigated wavelength range a whole silicon dioxide substrate may be used. In this case the material is a glassy form of quartz and is referred to as fused silica. Fused silica is transparent in the wavelength rage 0.18 - 2.2 $\mu$m and has a refractive index ranging from 1.47 at 0.4 $\mu$m to 1.45 at 0.8 $\mu$m [100].

Rectangular fused silica windows, polished flat on both sides and measuring approximately 13 × 24 × 1 mm, were used as substrates.

### 3.1.3 Metal Layer Fabrication: chromium and gold

Gold and silver are commonly chosen for plasmonic structures because they allow strong evanescent fields to form at the metal dielectric interface due to the relatively large values of the real part of their dielectric constants [8]. Gold is used in this investigation because of its high chemical durability. Gold has low adhesion to the surface of glass and silicon dioxide and the same is thought to be true of $CaF_2$. Therefore a layer of chromium was used to promote adhesion between the $CaF_2$ substrate and the gold layer. Chromium has however been found to reduce the grain size of the gold, resulting in lower conductivity of a thin gold layer [101].

The chromium and gold films were deposited in a vacuum chamber using thermal evaporation. Chromium sublimes at 1857±20 °C (2130±20 K) and gold melts at 1064 °C (1337 K) [102]. The material is held by a resistive element, the temperature of which is controlled by adjusting the magnitude of a current which passes through it; the temperature of this element in turn determines the material deposition rate. A shutter located between the material source and the substrate prevents deposition during source heating and enables fast termination of the deposition layer.

The rate and total deposited film thickness was determined using a standard crystal monitor which was only exposed to the coating source during deposition. This device monitors the deposited film thickness indirectly by detecting the change in resonant frequency of a piezoelectric crystal as the evaporated material is deposited upon it and automatically terminates deposition by closing the shutter once the desired thickness has been reached.

Following cleaning, the $CaF_2$ substrate was attached to a microscope slide using Kapton tape and mounted in the coating chamber. The tape also masked an area of the substrate from metal deposition, allowing it to be used as a background sample during spectroscopic transmission measurements. The coating chamber was then pumped until a base pressure in the $10^{-7}$ mbar range was achieved.

Initially the chromium adhesion layer was deposited. Pellets of chromium held in a tungsten filament basket were resistively heated with a current of approximately 4.2 A at 30 V potential difference. After gradually ramping the current to 4.2 A and waiting a few seconds for the chamber pressure to stabilise the shutter was opened. A deposition rate of approximately 0.3 nm/s was maintained until a 5 nm thick layer of chromium was recorded on the crystal monitor, after which the layer was terminated.

Following chromium deposition the gold source was brought into position beneath the sample. Gold wire lying in a molybdenum boat was resistively heated with a current of approximately 4 A at 10 V potential difference. Following ramping of the current to 4 A the shutter was opened and a deposition rate of approximately 2 nm/s was maintained until a 35 nm thick layer of gold was recorded on the crystal monitor and the layer was terminated.

Following metal deposition the sample was left in the chamber for five to ten minutes allowing the apparatus to cool. The chamber was then vented and the sample removed. The Kapton tape was then pealed off and the thickness of the deposited layer measured using a stylus profilometer. The measured thickness is used to calibrate the crystal monitor to increase the accuracy of future depositions.

### 3.1.4 Focused Ion Beam

To fabricate apertures material must be removed from the metal layer. Initially focused ion beam (FIB) milling was used to create the apertures. FIB milling is a resistless process which allows rapid adjustment of milling parameters and some *in situ* micrograph assessment of the process outcome.

FIBs were initially developed from sources of charged particles designed for electrostatic propulsion. These beams were refined for high brightness and applied to micromachining where the ions remove materials from a surface by sputtering. Several ion sources are available, with the most common being helium and gallium. Helium is used for imaging because the low ion mass produces minimum sample damage. For micro-and nano-machining the higher mass gallium ions are used to increase sputter yield. Gallium ions are produced using a liquid metal electrohydrodynamic (EHD) source also known as a liquid-metal ion source (LMIS) [103, 104]. Gallium is used because of its many favourable properties including low melting point (29.8 °C [102]), low vapour pressure and high brightness when compared to other candidate materials (*e.g.* cesium and mercury) [105].

To form the ion beam a reservoir of gallium is heated to melting and the liquid metal allowed to flow over a tungsten needle which has a tip radius of 2 - 5 $\mu$m. A circular extraction aperture is used to produce a $10^{10}$ $\mathrm{Vm}^{-1}$ electric field which forces the gallium to a circular area approximately 5 nm in diameter. The potential difference produced by the extractor pulls gallium from the tip and ionises it by field evaporation. The gallium ions are accelerated using a kilovolt potential difference through the ion column and focused into a beam by a series of electrostatic lenses. The ion-beam current reaching the sample is controlled by apertures that are placed in the beam path and block some of the beam. Our system uses a 30 kV acceleration

voltage. The available ion beam currents range from 1 pA to 50 nA.

The momentum of the gallium ion beam results in sputtering when the ions collide with the sample surface. If the ion beam is scanned over a surface, material will be selectively removed from the areas scanned by the ion beam. Different materials sputter at different rates, with gold being easily sputtered. Therefore imaging with FIB of gold areas which are to be milled must be minimised in order to avoid metal layer degradation. Figure 3.1 shows the result of scanning a 1 pA gallium ion beam over a film containing 5 nm chromium and 30 nm gold layers on a $CaF_2$ substrate. The SEM micrographs labelled (a), (b), (c), (d), (e), (f), (g) and (h) show trenches produced by ion beam line doses of 1, 2, 3, 4, 5, 10, 15 and 20 pC/$\mu$m respectively. The gold is removed at lower doses, followed by the chromium layer, and then the surface of the $CaF_2$ substrate.

Figure 3.1 (i), (j) and (k) show schematic mill profiles which illustrate this milling process. The mill profile shown in (i) depicts the initial removal of the easily sputtered gold layer. Mill profile (j) shows the removal of the chromium adhesion layer, along with additional sputtering of the gold layer, which causes a widening of the milled trench. Finally, mill profile (k) shows the milling of the $CaF_2$ substrate, whilst the continued FIB exposure causes further widening of the milled trench which now cuts through the gold and chromium layers. These processes are discernible in the SEM micrographs, in which the gold is shown as a light grey area. Following the complete milling of the gold layer and resultant exposure of the chromium layer a dark grey strip running down the centre the gold area is formed. Following the complete milling of the chromium layer and exposure of the $CaF_2$ substrate a grey/black strip, which runs down the centre of the exposed chromium, is shown. The dark grey strip, caused by the complete milling of the gold

layer, widens as we move from plate (a) to (h), whereas the grey/black strip caused by the complete milling of the chromium layer is not fully visible in the micrographs before plate (f), and is clearly visible, and wider, in plate (h). It would be possible to investigate this further using an atomic force microscope (AFM).

The widening of the trench in Figure 3.1 demonstrates the effect of the of ion beam current distribution. As the ion dose increases in the trench width also increases. This is because areas of the surface that are scanned by the lower ion density tails of the ion beam profile require a higher total dose to be completely removed. The investigation of the ion beam dose required to remove the metal layer is detailed in Section 4.2.1.

### 3.1.5 FIB SEM Cross Beam

A scanning electron microscope (SEM) and FIB are combined in a two-beam system. A vacuum chamber with both SEM and FIB systems attached in fixed positions that allow the two beams to have a coincident point where they may both be focused. A sample mounted on a movable stage may then be placed at this coincidence point. Imaging of the sample may then be undertaken using SEM, avoiding unintentional sputtering of the sample by the FIB.

Following cleaning of the substrate and deposition of the metal layer the sample was mounted on a movable stage located within the FIB/SEM vacuum chamber. The sample was grounded to prevent charge acumulation from the both the FIB and SEM beam. Either silver paste or carbon tape were used to provide the electrical contact. Carbon tape was preferred as the removal of silver paste causes particles of silver to be deposited on the sample surface, potentially ruining the fabrication.

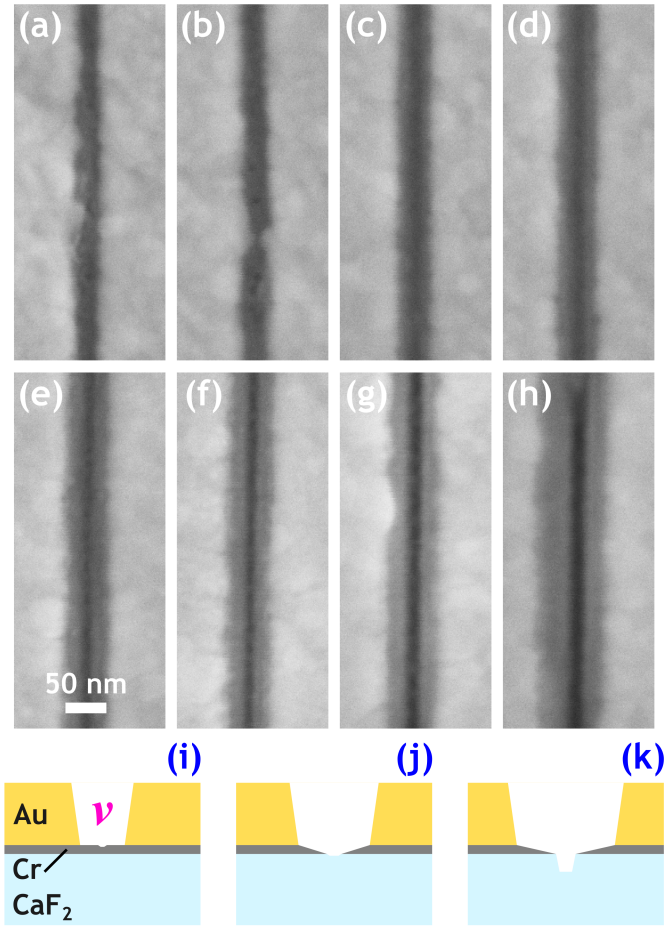


Figure 3.1: SEM micrographs showing the effect of milling a 30 nm gold and 5 nm chromium film on a calcium fluoride substrate with a 1 pA gallium FIB line scan. Line doses from (a) to (h) are 1, 2, 3, 4, 5, 10, 15 and 20 pC/$\mu$m. (i), (j) and (k) show schematic mill profiles across the line scan at three milling stages, the label $v$ shows the void in the film and substrate caused by the FIB milling.

The pattern to be scanned was created using the Inkscape vector graphics editor and exported as a bitmap. In the case of an aperture array a single aperture area was created and then reproduced in a matrix. Only the ratio of the array dimensions were considered during pattern design as the physical size of the pattern was determined by the magnification of the FIB at the milling stage. The magnification of the SEM was set so that the scanned area matched the desired size of the array. An area free of surface iregularity was then chosen using the SEM and a single scan of this are made by the FIB. A bitmap of the array was created and imported into the FIB milling software (Carl Zeiss FeatureMill Version 1.0.2), which controlled the scanning of the FIB during milling. This software has a fixed resolution of (1024,768) pixels. Hence, if the imported bitmap has a higher resolution, aliasing of the pattern occurs, creating variation in the aperture dimensions. The bitmap pattern used to fabricate the investigated apertures was therefore limited to 16 $\times$ 16 unit cells. The mill time, ion beam current and milling area was then selected and the milling started. The software scanned the FIB in a pattern corresponding to the bitmap image. Once complete the resultant apertures were assessed *in situ* using the SEM.

### 3.1.6 Electron Beam Lithography

Electron beam lithography (EBL) is a resist-based process where an electron beam is used to chemically alter resist coating a sample [106]. The exposed resist is then removed in the case of positive tone resist, or remains on the sample in the negative tone case. The remaining resist then acts as a mask during the subsequent processes. When compared to available UV optical lithography the electrons used in EBL have a much smaller wavelength than ultraviolet light and sub 50 nm features may be fabricated. Since no optical

mask is required the cost of the process is reduced when compaired to small batch optical lithography processing of the same resolution features and the speed of pattern iteration is increased.

When compared to FIB milling of aperture arrays, EBL has several advantages. Some of the advantages are the result of superior software and design of our EBL system when compared to the available FIB tool. The EBL can expose features over an area of 10000 $\mu$m$^2$ without stitching (the FIB process produced arrays of approximately 1000 $\mu$m$^2$). This allows the creation of much larger arrays, allowing a larger area to be illuminated during spectroscopic characterisation resulting in an improvement of the signal to noise ratio.

Poly(methyl methacrylate) (PMMA) resist was used. Upon exposure to the electron beam PMMA changes chemically (cracks) and becomes more soluble in the developing solvent methyl isobutyl ketone (MIBK).

The process used to fabricate raised metallic features using EBL is (i) PMMA resist coating of a bare substrate, (ii) EBL exposure of the metallic feature pattern, (iii) removal of exposed PMMA revealing the underlying substrate, (iv) deposition of the metal features using thermal evaporation, (v) removal of any remaining resist including its metal coating. This process is referred to as liftoff.

The process used to fabricate apertures using EBL is (i) PMMA resist coating of a metal coated substrate, (ii) EBL exposure of the aperture pattern, (iii) removal of exposed PMMA revealing the underlying metal layer, (iv) removal of the exposed metal layer using argon ion milling, (v) removal of any remaining resist. These steps may be repeated following a pattern alignment procedure if additional PMMA coating/removal is required. For additional pattern exposures a mask alignment procedure must

be performed. Details of the EBL based aperture fabrication procedure are given in Appendix A.

Figure 3.2 shows the layout of a typical EBL exposure pattern used in the investigation. The crosses in the four corners are alignment markers used in multiple step exposures. A matrix of cruciform aperture arrays is located in the labeled aperture array area. The columns contain arrays of different sized apertures and the rows correspond to different electron beam doses. Letters and numbers indicate the position of the aperture arrays in the matrix. A region of the metal layer measuring $300 \times 300$ $\mu$m or bigger is also removed to allow the measurement of transmission through the substrate for normalisation (shown in green in the diagram). The blue and green regions are exposed, developed and ion milled first. The sample is then imaged using SEM to assess the quality of the fabrication and determine the fabricated aperture dimensions. The aperture arrays are then measured spectroscopically using FTIR (see Section 3.2.1).

If the apertures are to be filled with PMMA (to investigate the interaction of localised surface plasmons and the PMMA carbonyl bond) a second exposure is required. This removes the PMMA from the regions used for measuring the transmission (green) and reflection (red) normalisation signals. The sample is first recoated with PMMA and the placed in the EBL. Alignment marks are used to position the sample and the green and red regions are exposed and developed. The sample should not be imaged using SEM following this process as this will degrade the PMMA layer. No additional argon ion milling is required following the second exposure.

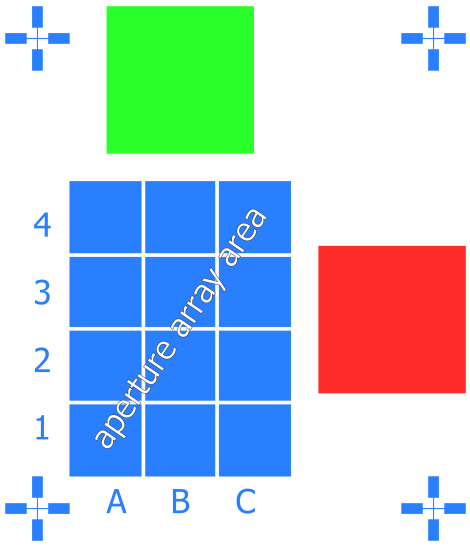


Figure 3.2: Layout of a typical EBL exposure pattern used in the investigation. Blue and green regions are exposed, developed and ion milled first; if a second exposure is required the green and red regions will be exposed and developed.

### 3.1.7 Argon ion milling

To remove material from the metal layer following EBL we use a broad-beam argon ion miller. A broad-beam of accelerated atoms mechanically removes (sputters) atoms when it collides with a surface. The beam is produced by accelerating ionised gas using a potential difference. A gas is introduced into a discharge chamber and its atoms are ionised. A potential difference then accelerates the ions towards the sample. They are then neutralised to prevent charging of the sample [107]. As the accelerated atoms are not focused they can remove material from a much larger area than the FIB discussed in Section 3.1.4.

Figure 3.3 shows a gridded broad-beam ion source schematically. A current is passed through the cathode which emits electrons through thermionic emission. A potential difference between the cathode and the anode accel-

erates the emitted electrons towards the anode. The potential difference between the cathode and the anode is called the beam voltage, $V_b$, and the current flowing between them is called the beam current, $I_b$. Argon gas flows into the discharge chamber at a constant rate. Some of the argon atoms collide with the accelerated electrons and are ionised. Magnets about the chamber affect the movement of the electrons and ions, causing the electrons to follow longer paths to the anode so that they are exposed to more atoms to increase the ion yield. Some of the ions travel to the ion optics which consist of a screen grid and acceleration grid. The screen grid, which is held at the cathode potential, is used to protect the acceleration grid from ion damage. The accelerator grid is held at a negative potential, $V_a$, called the accelerator voltage. Ions passing through the screen grid are accelerated by the acceleration grid voltage towards the sample. A filament located next to the accelerator grid, the neutraliser, emits thermal electrons which neutralise the ion beam to prevent charging of the substrate. The accelerated argon atoms then travel to the sample where they sputter the surface atoms.

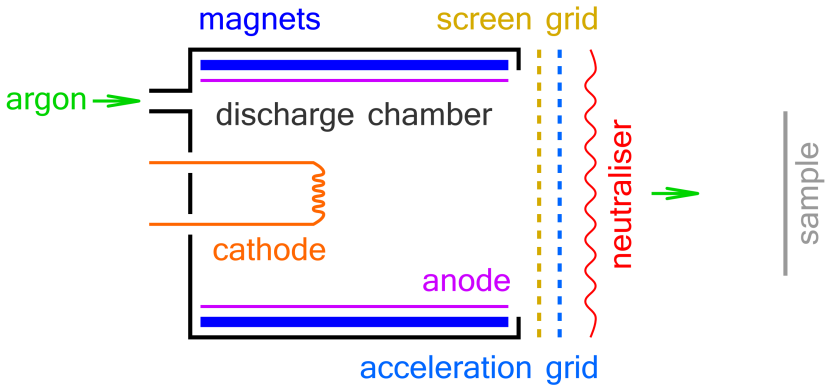


Figure 3.3: Schematic diagram of a gridded broad-beam ion source.

The sample is mounted on a carbon plate using Kapton tape; the plate is

attached to a water cooled assembly to prevent sample heating. The argon ion miller chamber is then evacuated to a base pressure in the $10^{-7}$ mBar range. Argon is injected into the discharge chamber at a rate of 5 standard cubic centimeters per minute (SCCM). After switching on the cathode the system is left for ten minutes before switching on the accelerator grid so that the screen and accelerator grids can expand to the same size. The sample stage is rotated at 20 RPM to prevent shadowing of the mill area. A shutter between the ion gun and the sample prevents sputtering during beam stabilisation. The shutter is opened to allow milling and closed to terminate the process.

The parameters used in our argon ion milling are as follows: $V_b = 200$ V, $I_b = 10$ mA, $V_a = 390$V. The neutraliser is adjusted automatically to produce an emission current 1.25 times the beam current. The beam diameter at the sample is 30 mm, resulting in a current density of $14 \times 10^{-3}$ mA/mm$^2$.

To determine the gold mill rate a 150 nm gold film and 5 nm chromium adhesion layer were deposited on two calcium fluoride substrates. The gold surfaces were partially masked using Kapton tape so that a step would form during milling. The first sample was exposed to the argon ion beam for 600 seconds; the second sample was exposed for 1200 seconds. Following the exposures, seven stylus profilometer measurements were made on each sample and the mean step height taken. The gold mill rate was found to be $0.088 \pm 0.003$ nm/s.

A single sample was used to determine the approximate mill rate of the PMMA mask. EBL was carried out on an 85 nm thick PMMA mask coating 5 nm chromium and 35 nm gold layers on a calcium fluoride substrate. This formed several $0.5 \times 0.5$ mm areas of exposed metal surrounded by the PMMA mask. An exposure time of 798 seconds was used and the

PMMA mask/sample step measured four times using a stylus profilometer, the PMMA was then removed and the same step measured again. The PMMA had a mill rate of $\sim 0.06$ nm/s; this limits the maximum exposure time of the EBL sample made with 80 nm PMMA resist to approximately 23 minutes.

The chromium milling rate is approximately 0.35 times that of gold (taken from a data sheet supplied by Oxford Applied Research Ltd.). The total mill time was therefore set at 10 minutes to ensure complete metal layer removal. Following milling the ion gun was switched off and the system left to cool for 10 minutes before the apparatus was vented and the sample removed.

## 3.2 Characterisation

### 3.2.1 Fourier Transform Infrared Spectroscopy

Fourier Transform Infrared Spectroscopy (FTIR) [108, 109] was used to measure the transmission and reflection spectra of the fabricated cruciform aperture samples in the 2 - 8 $\mu$m wavelength range.

The FTIR is based on the Michelson interferometer, first used in the Michelson and Morley experiment in 1887 which disproved the theory of the luminiferous ether [110]. Figure 3.4 shows the Michelson interferometer schematically.

If we consider monochromatic light source of wavenumber $\bar{\nu}$ and spectral intensity $B(\bar{\nu})$, passing through the Michelson interferometer with the mirror moving at constant velocity, then the light intensity, $I'$, at the detector varies

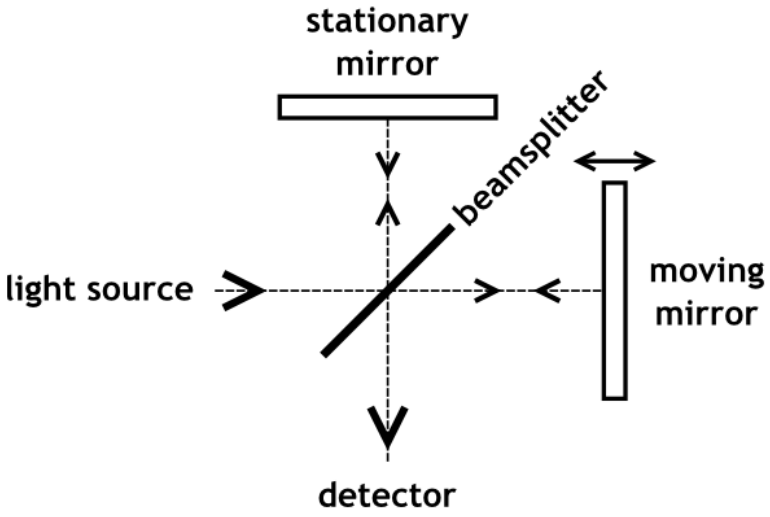


Figure 3.4: Schematic representation of a Michelson interferometer.

as a function of the displacement $\delta$ of the mirror

$$I'(\delta) = B(\bar{\nu})[1 + \cos 2\pi\bar{\nu}\delta] \tag{3.1}$$

When the source contains multiple frequencies $I'(\delta)$ becomes

$$I'(\delta) = \int_{-\infty}^{\infty} B(\bar{\nu})[1 + \cos 2\pi\bar{\nu}\delta]\ d\bar{\nu} \tag{3.2}$$

This is the signal reaching the detector. There is a constant term which can be discarded, leaving the expression for the interferogram

$$I(\delta) = \int_{-\infty}^{\infty} B(\bar{\nu}) \cos 2\pi\bar{\nu}\delta\ d\bar{\nu} \tag{3.3}$$

(An example of an interferogram is shown in Figure 3.6 (b).) As the interferogram is the cosine Fourier transform of $B(\bar{\nu})$, the spectrum of the light

reaching the detector can be recovered using the inverse Fourier transform

$$B(\bar{\nu}) = \int_{-\infty}^{\infty} I(\delta) \cos 2\pi\bar{\nu}\delta \; d\delta \tag{3.4}$$

The sample is placed between the interferometer output and the detector and the interferogram recorded.

As the fabricated structures have an area between approximately 1100 and 10000 $\mu m^2$ a microscope is used in combination with the FITR apparatus to focus light onto and collect light from the sample. Figure 3.5 shows the relative positioning of the components in the FTIR microscope. A 633 nm wavelength helium neon (He-Ne) laser is used to monitor the position of the moving mirror. The laser beam passes through the Michelson interferometer and interference causes a sinusoidal intensity change of the laser light as a function of mirror position (see Equation 3.1). The moving mirror position is recorded as a function of the zero crossings of this sinusoidal signal. In transmission mode a condenser lens focuses the interferometer output onto the sample, an objective lens then collects the transmitted radiation after which it is passed to the detector. In reflection mode the interferometer output is reflected by a mirror into the objective lens where it is focused onto the sample; reflected light then passes back through the objective lens and past the mirror to the detector. A liquid nitrogen cooled mercury cadmium telluride (MCT) detector was used to measure the spectral intensity.

A movable sample stage allows precise positioning of the sample and an apertures located between the objective lens and the detector enables selection of the sampling area.

A calcium fluoride ($CaF_2$) wire grid polariser manufactured by Specac Limited was placed in the light path before the sample to polarise the beam.

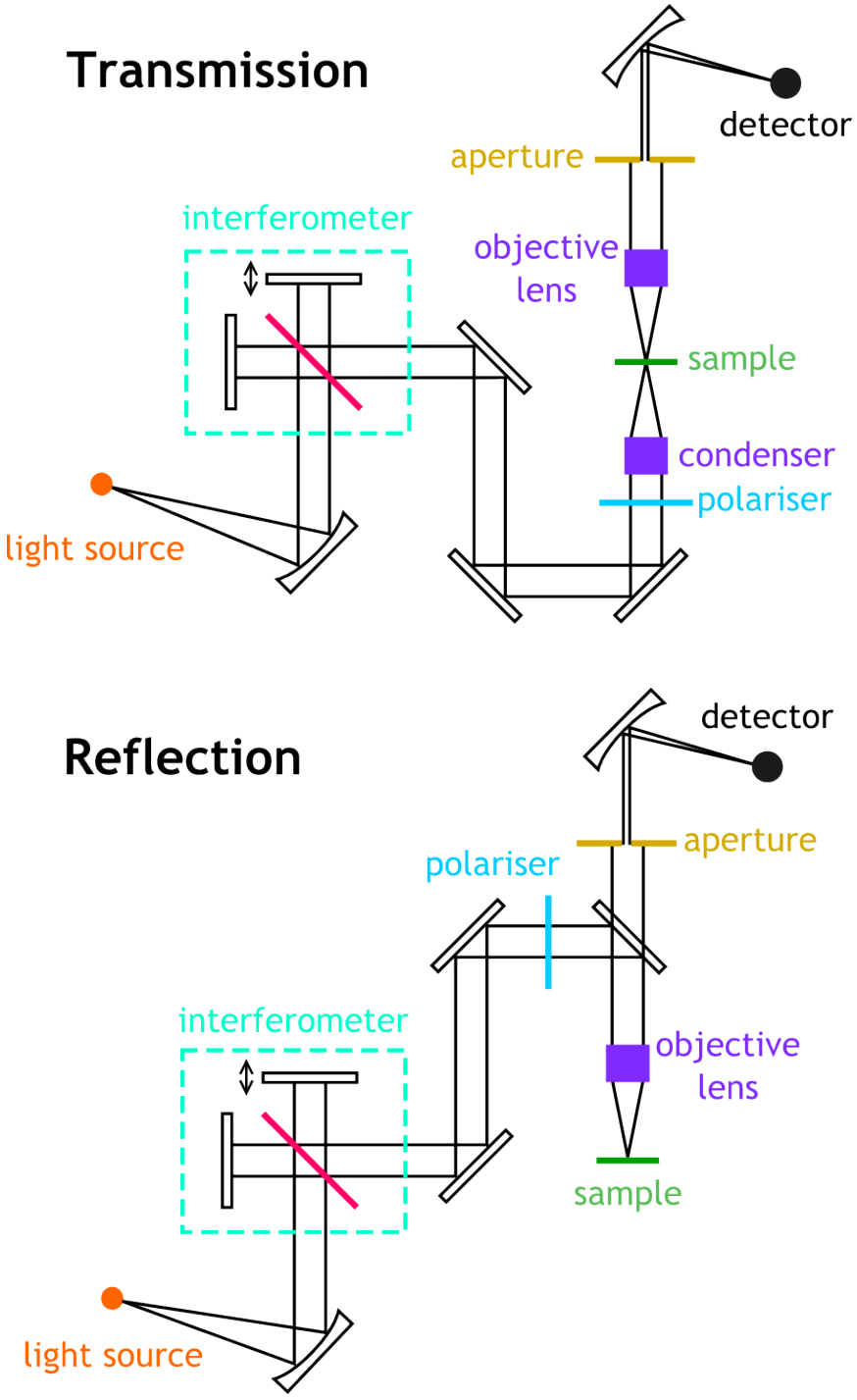


Figure 3.5: Schematic representation of an FITR microscope in transmission and reflection modes.

The polariser is specified as having an extinction ratio of 314:1 at 5 $\mu$m wavelength. To alter the **E** field polarisation incident on the sample the sample stage was rotated.

A water cooled glowbar was used as the light source. Figure 3.6 (a) shows the spectral intensity produced by the glowbar. There is a variation in spectral intensity resulting from the spectral variation of the glowbar radiation, the wavelength sensitivity of the MCT detector and the absorption of radiation by chemical species in the atmosphere. The intensity minimum at wavelength 4.2 $\mu$m is caused by carbon dioxide absorption and the minima between 5.3 and 7.7 $\mu$m are produced by water vapor absorption. This intensity variation is removed by normalising the sample spectrum to a background spectrum. For a transmission measurement the background spectrum is taken through the substrate; for reflection measurements the background is taken from the gold surface.

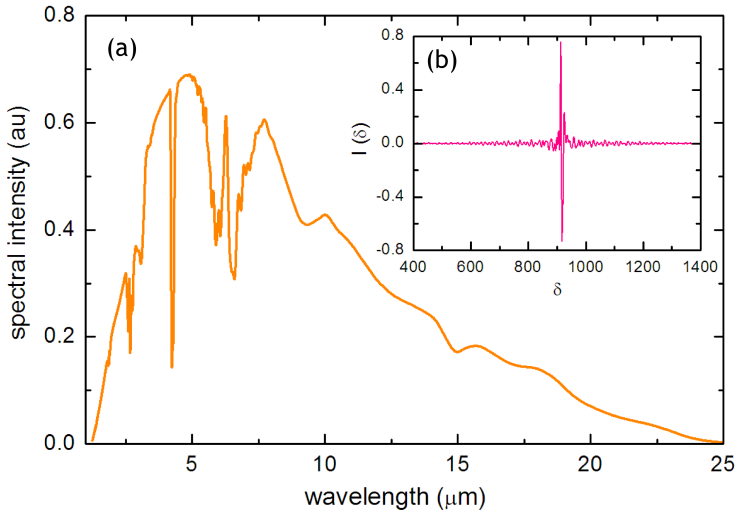


Figure 3.6: (a) The spectral intensity of the glowbar used in the FTIR measurements. (b) Part of the interferogram measured by the FTIR which was used to generate (a).

Figure 3.7 shows the improvement of the signal to noise ratio attained

by increasing the FTIR sampling area. The local transmission minimum at wavelength 4.2 $\mu$m is produced by a change in the carbon dioxide concentration near the sample between the background and sample measurements. The red line plots the transmission spectrum from an EBL fabricated aperture array measured using an FTIR aperture which selects a 30 $\mu$m diameter sample area; this is compared with the black line which plots the transmission spectrum from the same aperture array measured using an FTIR aperture which selects a 79 $\mu$m diameter sample area. The sample was not repositioned between measurements and the incident light was not polarised. As FIB fabricated arrays measured 33 $\mu$m $\times$ 33 $\mu$m only the 30 $\mu$m diameter aperture could be used, resulting in a noisier spectrum than can be obtained using larger area EBL fabricated arrays.

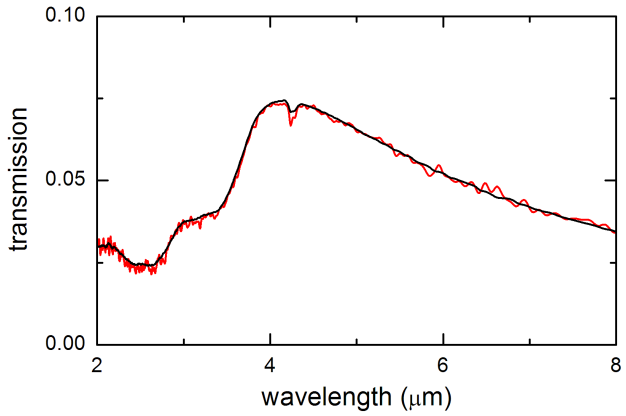


Figure 3.7: Transmission spectrum produced from an EBL fabricated array. The measurement is made using a 30 $\mu$m diameter aperture (red) and a 79 $\mu$m diameter aperture (black).

### 3.2.2 Second Harmonic Generation Microscopy

When light travels through a material the electrons in the material oscillate in response to the changing **E** field. This is the origin of the macroscopic polarisation $\mathbf{P} = \epsilon_0 \chi \mathbf{E}$ where $\epsilon_0$ is the permittivity of free space and $\chi$ is the susceptibility of the material. When the electron oscillations are small **P** is directly proportional to the **E** field and higher order contributions can be ignored, however at higher **E** field magnitudes the oscillations become increasingly anharmonic and higher order contributions must be considered. The susceptibility is modified to the general case and

$$P_i = \epsilon_0(\chi^{(1)}_{ij} E_j + \chi^{(2)}_{ijk} E_{jk} + \chi^{(3)}_{ijkl} E_{jkl} + \ldots) \tag{3.5}$$

using the Einstein summation convention [58]. The linear polarisation term includes $\chi^{(1)}$, the second order nonlinear polarisation term includes $\chi^{(2)}$ and so on. An intense laser beam has an **E** field that can induce a nonlinear polarisation in the material. One of the optical effects produced by the second order nonlinear polarisation is the production of a coherent wave at exactly half the incident wavelength. This second harmonic generation (SHG) occurs in noncentrosymmetric materials, on rough metal surfaces and at metal dielectric interfaces.

The nonlinear optical response of a material may be used to image structural inhomogeneity which might not be accompanied by a change in refractive index but which creates a large variation in the nonlinear response of the material [111]. This, and the availability of laser scanning microscopes for two photon excited fluorescence microscopy, has allowed SHG microscopy to be developed for use in the biological sciences [72, 112]. SHG microscopy has also been used to directly observe the localised SHG enhancement in random

metal nanostructures [73]. We have used SHG microscopy to measure the near-field SHG produced by plasmonic nano-structures.

Figure 3.8 shows the SHG microscope schematically. Femtosecond pulses with wavelength $\lambda_f$ are generated by a tunable titanium sapphire (Ti:sapphire) laser. The pulses pass through the laser scanning mirror assembly. Movement of the mirrors alters the beam path and allows scanning of the sample by the laser (this assembly is not shown). The pulses are then polarised and reflected by a dichroic mirror towards the sample. The polarisation of the laser beam is adjusted by placing a half-wave plate (for linearly polarised light) or a quarter wave plate (for circularly polarised light) in the laser beam path. A 100× oil immersion objective with a 1.46 numerical aperture focuses the laser to a spot on the sample. Light reflected from the sample is collected by the objective and passes back through the wave plate to the dichroic mirror. Reflected light with the fundamental wavelength $\lambda_f/2$ passes through the mirror and then through a short pass filter to ensure the removal of the light with wavelength $\lambda_f$. The remaining light, which is produced by SHG is detected by a photomultiplier tube. The intensity of the SHG signal is recorded as a function of the laser spot position, allowing an SHG intensity map to be produced.

An example of the near-field SHG produced by a patterned metal surface is shown in Figure 3.9. I fabricated four nano-patterned metallic surfaces using EBL. The metallic features contain 5 nm chromium and 35 nm gold layers arranged in 200 nm wide strips. Figure 3.9 (a) shows SEM micrographs of the four different unit cells used in the four surface patterns. These patterns were scanned by the SHG microscope using two incident **E** field polarisations, $\theta = 0°$ and 90°. Figure 3.9 shows the SHG intensity maps produced by the four unit cell paterns. The regions of high SHG intensity,

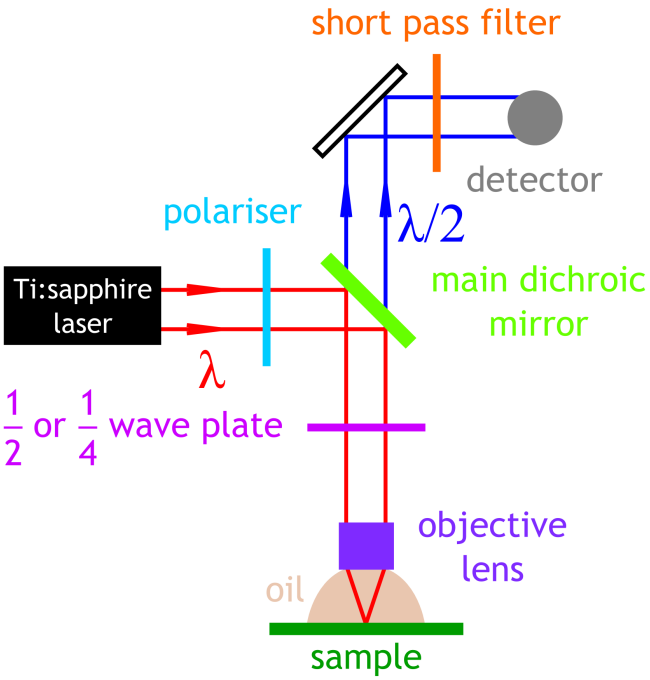


Figure 3.8: Schematic diagram showing the SHG microscopy apparatus.

referred to as SHG hotspots, are polarisation sensitive. Figure 3.9 (c) shows an overlay of the SEM and SHG micrographs for **E** field polarisation $\theta = 90°$, linking the SHG hotspots to areas of the metallic structure.

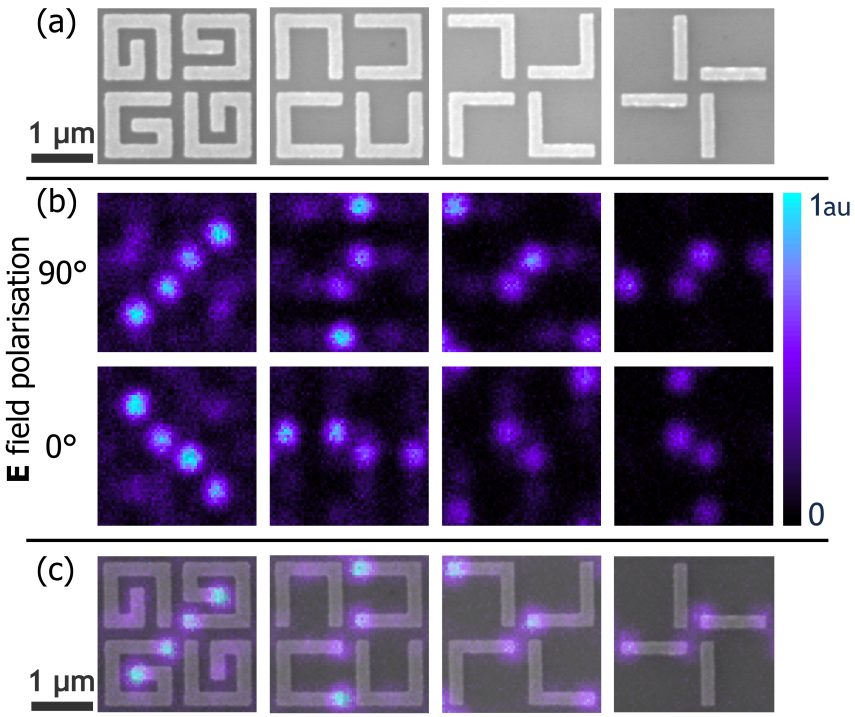


Figure 3.9: (a) SEM micrographs showing unit cells of a metallic structures on a silicon dioxide substrate. (b) Scanning laser microscope SHG intensity maps of the structures shown in (a). The intensity maps are recorded at incident **E** field polarisations $\theta = 0°$ and $\theta = 90°$. (c) Overlay of the SEM micrographs shown in (a) and the SHG intensity maps shown in (b). Measurements were performed by Dr V. K. Valev, KU Leuven.

# Chapter 4

# Experimental Results and Analysis: Linear Optical Response

The transmission peaks produced by sub-wavelength apertures occur when the resonant frequency of the plasmonic structure matches the frequency of incident light. In the case of a sub-wavelength aperture array the resonance can be tuned by altering a number of variables, allowing the array's transmission spectrum to be engineered. In the case of surface plasmon polaritons (SPPs) the aperture dimensions, aperture pitch, surrounding dielectric constant and the incident angle of light as well as the plasmon supporting material may be adjusted to produce a desired resonance. Localised surface plasmon (LSP) resonances are insensitive to aperture pitch but their resonance may be tuned by altering aperture dimensions, the surrounding dielectric constant or the plasmon supporting material.

At the resonant frequency of the plasmonic structure there is a large electron displacement with an associated electromagnetic field concentration

[113]. The field enhancement associated with the resonant frequency of a plasmonic structure can produce an increase in the optical absorption of materials located within the region of the enhanced electromagnetic field. As it is possible to alter the resonant frequency of a sub-wavelength aperture by changing its dimensions it is possible to engineer an aperture with a resonance and associated field enhancement that matches that of a molecular bond. If the transmission peaks are engineered to be in the spectral region of the resonance of a material (eg. an organic bond), the interaction of the plasmonic system and the material may be investigated. In the case of asymmetric cruciform apertures the interaction can be tuned *in situ* by varying the incident **E** field polarisation [5, 6].

This chapter details our investigation of nano-scale asymmetric cruciform apertures. We use two fabrication methods to produce the apertures, focused ion beam (FIB) milling of a gold film and electron beam lithography (EBL) followed by argon ion milling of a gold film. The results produced by these two fabrication methods are detailed in separate sections. The final section details our investigation into the coupling of the plasmonic meta-molecules formed by the apertures with the carbonyl bond of the polymer poly(methyl methacrylate) (PMMA). Two models that were produced to describe this system are presented. The first is a classical coupled resonator model, the second a quantum mechanical model.

As both the FIB and EBL fabricated structures use the PMMA carbon oxygen double bond in their investigation this material is introduced in the following section.

## 4.1 Optical Properties of Poly(methyl methacrylate)

Molecular bonds have resonant frequencies which are determined by the bond structure and surrounding molecular forces. Light encountering a bond is absorbed if its frequency matches the resonant frequency of the bond. This results in material specific absorption spectra which are the basis of infrared spectroscopy.

The PMMA carbon oxygen double bond (carbonyl bond) produces a distinct narrow-band absorption caused by bond stretching at 1729 $cm^{-1}$ (5.784 $\mu$m) [53]. The attenuation of the PMMA film produced by our spin coating process was measured using FTIR. A solution of PMMA dissolved in anisole was spun onto a $CaF_2$ substrate that had been partially coated with gold and the anisole removed by heating, leaving a PMMA film of thickness 85 nm. Part of the PMMA film was then removed from the $CaF_2$ and gold surfaces using EBL. Figure 4.1 shows the sample arrangement schematically. The normalised transmission spectrum of PMMA is $T_{PMMA} = S_T/B_T$ and the normalised reflection spectrum of PMMA is $T_{PMMA} = S_R/B_R$, where the regions used to measure $S_T$, $B_T$, $S_R$ and $B_R$ are defined in Figure 4.1. Figure 4.2 shows the measured transmission and reflection spectrum of the PMMA film. There is a transmission minimum at $5.79 \pm 0.03$ $\mu$m that is consistent with the carbonyl bond resonant wavelength quoted in [53]; this transmission minimum can therefore be attributed to the stretching of the PMMA carbonyl bond.

Asymmetric cruciform apertures were engineered so that the wavelength of the transmission peak produced when the incident polarisation $\theta = 90°$ matched the transmission minimum of the PMMA carbonyl bond. PMMA was then

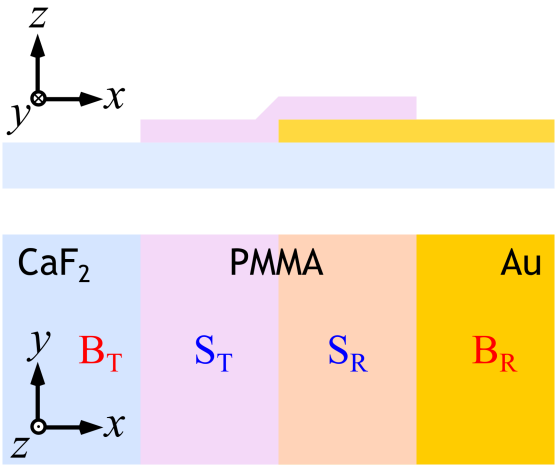


Figure 4.1: Schematic cross section (top) and plan (bottom) of the PMMA characterisation sample. The background signal was taken from regions B and the samples signal from regions S. Reflection and transmission sample regions are indicated by subscripts R and T respectively.

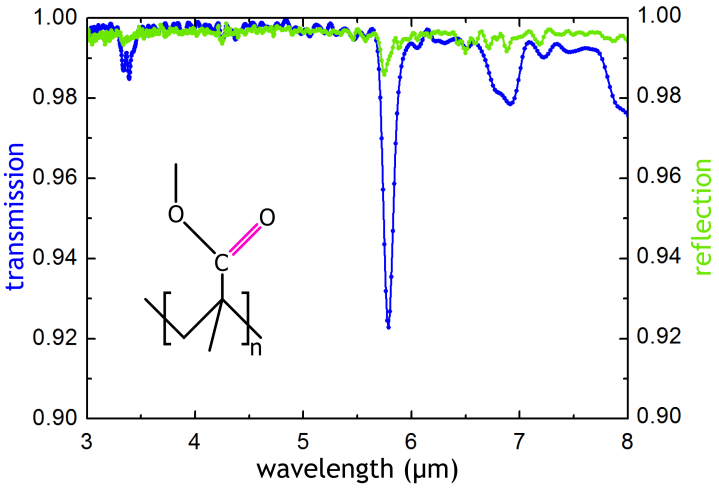


Figure 4.2: Transmission (blue) and reflection (green) spectra of an 85 nm thick film of PMMA. The transmission minimum at wavelength 5.79 $\mu$m is associated with the PMMA carbonyl bond. The inset shows the atomic structure of the PMMA monomer with the carbonyl bond highlighted in pink.

introduced to the apertures by spin coating. In the following sections we investigate the effect of tuning the plasmonic resonance of these apertures *in situ* by varying the **E** field polarisation of incident light. The interaction of the PMMA carbonyl bond resonance with the varying plasmonic modes is investigated.

## 4.2 Focused Ion Beam Fabrication of Asymmetric Cruciform Apertures

Arrays of asymmetric cruciform apertures containing 16 × 16 unit cells were fabricated using FIB milling of a metal film consisting of (approximately) 35 nm thick gold and 5 nm thick chromium layers on a 1 mm thick calcium fluoride ($CaF_2$) substrate. Figure 4.3 (a) and (b) show SEM micrographs of a typical array. The aperture geometry is shown in Figure 4.3 (c); the aperture is defined by four dimensions $G_x$, $G_y$, $L_x$ and $L_y$. The array is defined by the aperture pitch in the $x$ and $y$ directions. The polarisation of light illuminating the apertures is given by $\theta$, defined as the angle between the **E** field component of the incident light and the $x$ axis.

The ion beam used to excavate the apertures has a finite milling resolution which is limited by the maximum achievable focus of the machine and the interaction of the ion beam with the surface (including redeposition of sputtered material). This results in variability of the aperture dimensions within the array. Each array dimension is therefore given as the mean measurements from ten randomly selected apertures. The apertures shown in Figure 4.3 (a) and (b) have mean dimensions $G_x = 470$ nm, $G_y = 260$ nm, $L_x = 1800$ nm, $L_y = 1250$ nm with pitch 2.1 $\mu$m in both $x$ and $y$; the whole array has an area of 1091 $\mu m^2$. The gold area milled during fabrication was

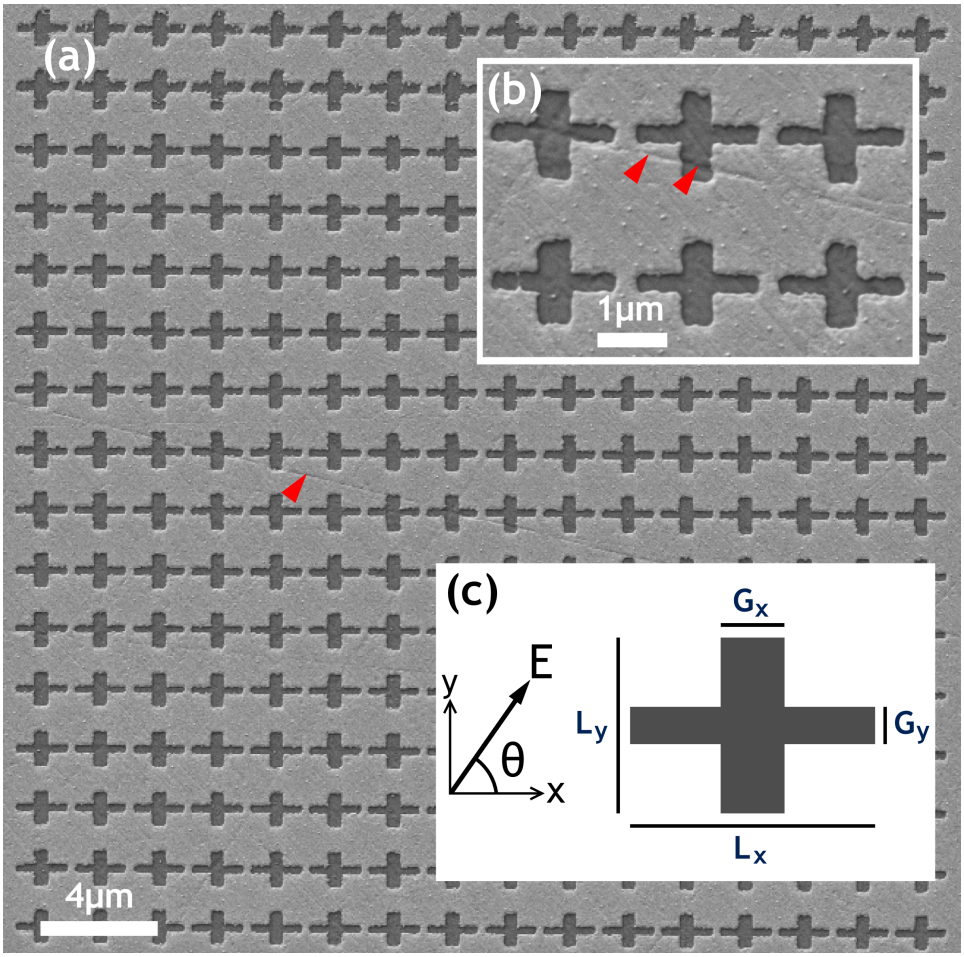


Figure 4.3: (a) SEM micrograph showing an asymmetric cruciform aperture array fabricated using a 161 pC/$\mu$m$^2$ ion beam dose. (b) 161 pC/$\mu$m$^2$ array detail. Red arrows indicate scratches on the gold film and $CaF_2$ substrate. (c) Aperture parameters. **E** field polarisation $\theta$ is given in degrees throughout.

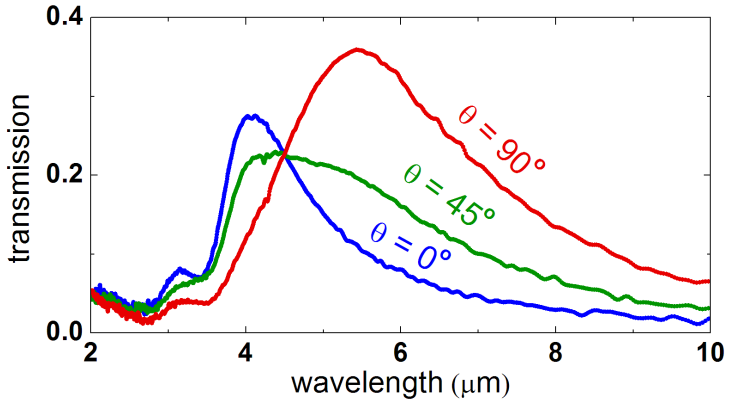


Figure 4.4: The transmission spectrum of an array of asymmetric cruciform apertures measured using FTIR at incident **E** field polarisations $\theta = 0°$, $\theta = 45°$ and $\theta = 90°$.

186 $\mu m^2$. Scratching, indicated in Figure 4.3 (a) and (b) by red arrows, is visible on both the gold surface and the $CaF_2$ substrate. As $CaF_2$ is soft and scratches easily these features are most likely to be artefacts of substrate lapping (polishing).

Figure 4.4 shows the transmission spectrum of the asymmetric cruciform aperture array at three incident **E** field polarisations, $\theta = 0°$, $\theta = 45°$ and $\theta = 90°$. There are two transmission peaks, one at wavelength 4.1 $\mu$m and one at wavelength 5.4 $\mu$m. The magnitude of these peaks is dependent upon the **E** field polarisation of the incident light. When $\theta = 0°$ the 4.1 $\mu$m peak is maximum whereas the peak at wavelength 5.4 $\mu$m is maximum when $\theta = 90°$. When $\theta = 45°$ the maximum aperture transmission is lower than that observed when $\theta = 0°$ or 90° at all wavelengths, this is expected because the eigenmodes of the plasmonic structure are not excited at this polarisation. At wavelength 4.5 $\mu$m the amplitude of the transmission is polarisation invariant and the spectra produced by all **E** field polarisations cross. This point is referred to as the isosbestic point by Roth *et al.* [5].

### 4.2.1 Dose Dependence of Array Transmission

The ion dose during array fabrication was thought to have an effect on the transmission of the aperture arrays. This is because too small a dose would result in insufficient material being removed from the metal layer, and too large a dose would result in excavation of the substrate, changing the refractive index near the apertures.

To determine the dose dependence of aperture transmission a series of nine aperture arrays was fabricated and the dose altered by changing the FIB milling time. Each aperture array had a total milling area of 186 $\mu m^2$. The FIB current was 50 pA and the acceleration voltage 30 kV. Milling times were 100, 200, 300, 400, 500, 600, 700, 800 and 900 seconds corresponding to ion beam doses of 27 pC/$\mu m^2$, 54 pC/$\mu m^2$, 81 pC/$\mu m^2$, 108 pC/$\mu m^2$, 134 pC/$\mu m^2$, 161 pC/$\mu m^2$, 188 pC/$\mu m^2$, 215 pC/$\mu m^2$ and 242 pC/$\mu m^2$.

Figure 4.5 shows the physical effect of dose increase that can be observed using a scanning-electron microscope (SEM). The metal layer appears to be thinned in Fig. 4.5 (a) with dose 27 pC/$\mu m^2$ where the crosses are visible as darker regions on the gold film. The calcium fluoride substrate becomes visible in Fig. 4.5 (b) with dose 54 pC/$\mu m^2$, however the metal layer is only partially removed. As the dose is increased more of the metal layer is removed. At doses of 161 pC/$\mu m^2$ and above (Fig. 4.5 (f) to (i)) the effect of increasing dose does not appear to change the appearance of the apertures in the SEM micrographs.

An increase in dose was expected to result in an increase in aperture size because of sputtering at the edge of the mill area. The ion beam has a bell shaped distribution with non-Gaussian tails. As the ion beam dose increases the width of the beam that has sufficient dose to remove the metal layer also increases. There is also more exposure to secondary ions that may

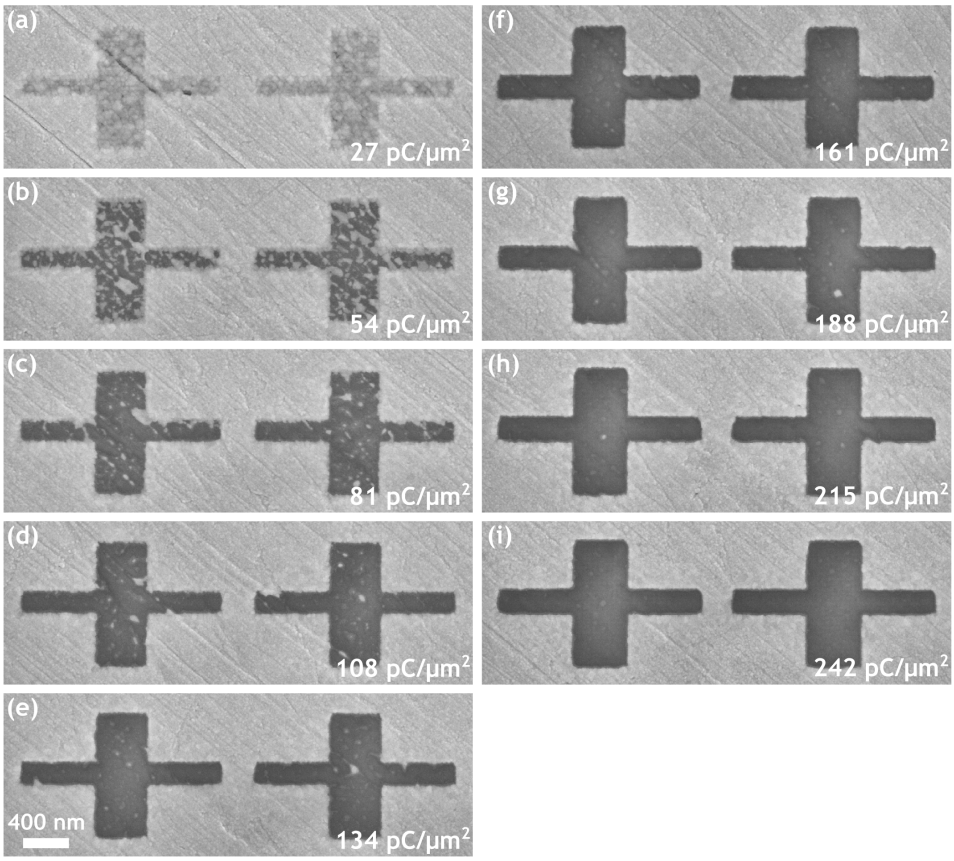


Figure 4.5: Scanning-electron micrographs showing typical cruciform apertures produced by FIB milling of a 5 nm chromium, 35 nm gold metal layer (light) on a calcium fluoride substrate (dark). The ion beam dose increases from 27 pC/$\mu$m$^2$ in (a) to 242 pC/$\mu$m$^2$ in (i).

sputter material at the edge of the mill area. This produces an increase in aperture dimensions with increased dose. To quantify the effect of increased dose on aperture dimensions the micrographs in Figure 4.5 were analysed quantitatively using the ImageJ 1.45s image processing software. The SEM micrographs are saved in the 8 bit grayscale TIFF format. A histogram of the micrograph grayscale intensities showed two peaks, one at low intensity (dark grey) corresponding to the $CaF_2$ substrate and one at high intensity (light grey) corresponding to the gold surface. The point between the two histogram peaks with the minimum number of counts was located at intensity 135; this was taken to be the boundary between areas of $CaF_2$ and gold. Therefore micrograph pixels with intensity values 0 - 135 are recorded as being milled areas and micrograph pixels with intensity values 136 - 255 are recorded as being unmilled areas. For each dose these measurements were made on six apertures and the mean taken. Figure 4.6 shows the increase in aperture area from 0.51 $\mu m^2$ at dose 54 pC/$\mu m^2$ to 0.87 $\mu m^2$ at dose 242 pC/$\mu m^2$, an increase in aperture area of 71%. However, from dose 188 pC/$\mu m^2$ to 242 pC/$\mu m^2$ the aperture area increase is 6%.

The arrays were measured using FTIR at **E** field polarisations $\theta = 0°$ and $\theta = 90°$. Figure 4.7 (a) shows the transmission spectra of these arrays at $\theta = 0°$. Figure 4.7 (b) shows the transmission spectra at $\theta = 90°$. The arrays transmit for ion beam doses exceeding 54 pC/$\mu m^2$. As the ion dose increases from 54 pC/$\mu m^2$ to 242 pC/$\mu m^2$ the transmission through the array increases for both **E** field polarisations.

As the ion beam dose increases the amplitude of the transmission spectrum for both polarisations increases and there is a blue shift in peak position. Figure 4.8 shows maximum transmission wavelength at **E** field polarisations $\theta = 0°$ and $\theta = 90°$ with increasing ion beam dose. The blue shift in

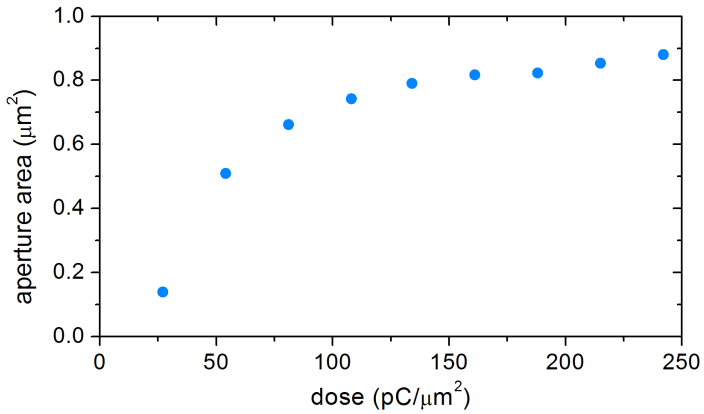


Figure 4.6: Dose dependence of cruciform aperture area. Points correspond to histogram threshold analysis of the SEM micrographs used to produce Figure 4.5 (a) to (i); the mean area taken from six analysed apertures is plotted.

maximum transmission wavelength as ion beam dose increases is present at both $\theta = 0°$ and $\theta = 90°$ polarisations. At both polarisations the change in blue shift decreases with increasing dose. Figure 4.6 shows that aperture areas are increasing with dose; this would be expected to produce a red shift in the spectra. Therefore another effect must be producing a blue shift which is stronger than the red shift produced by increasing aperture area. In addition to increasing aperture area FIB milling may produce two other changes in geometry during fabrication that will cause a change in the spectra. We refer to these two fabrication artefacts as under-milling and over-milling. Under-milling occurs when insufficient material is removed from the metal layer during milling; this produces the marked decrease in transmission at lower ion beam doses (see Figure 4.7). Over-milling occurs when material is removed from the substrate, this changes the refractive index immediately below the aperture. Figure 4.9 shows rigorous coupled-wave analysis (RCWA) simulations of an over-milled geometry. To determine the cruciform aperture dimensions used in the RCWA simulations, SEM micrographs

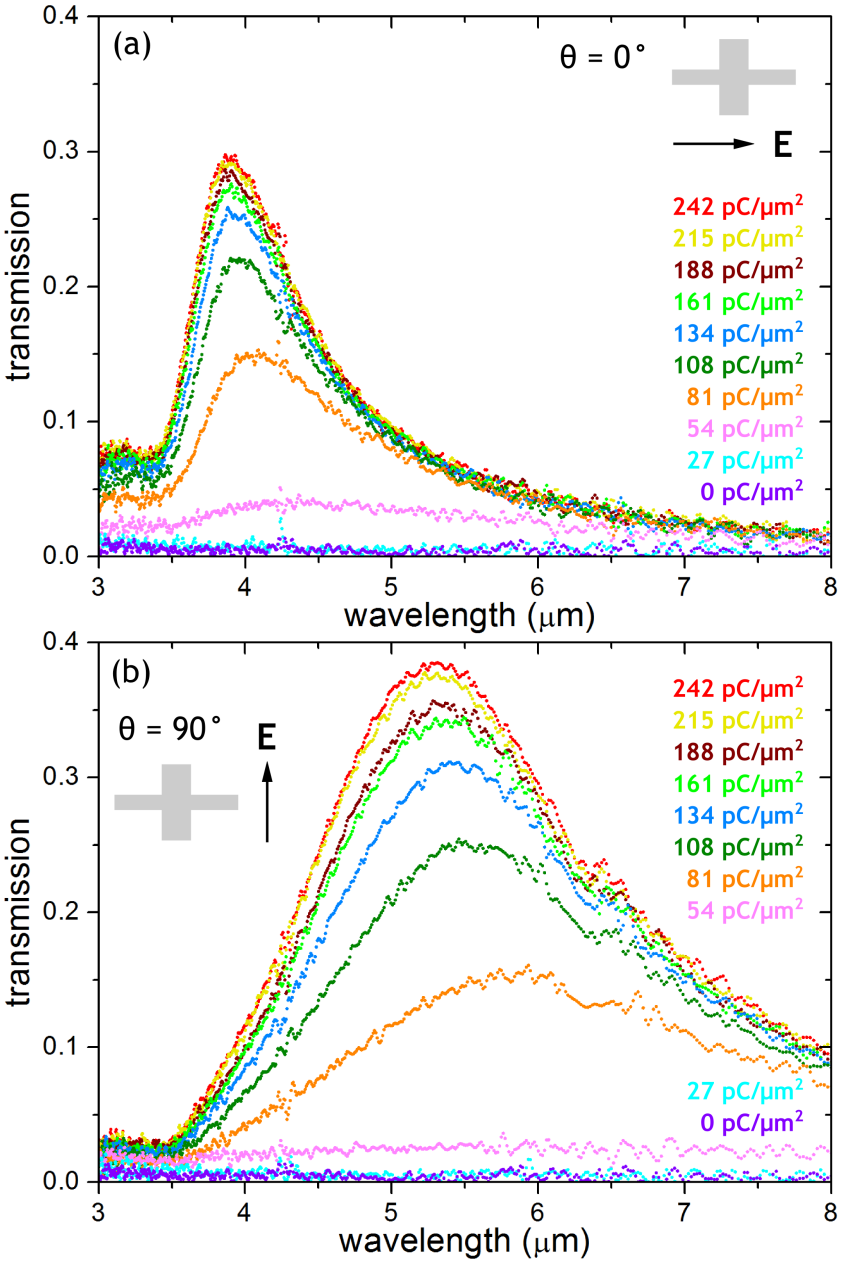


Figure 4.7: The transmission spectra of asymmetric cruciform aperture arrays fabricated using nine ion beam doses. Curve dose is indicated by labels of the same colour. (a) $\theta = 0°$ (b) $\theta = 90°$. The grey cruciform and arrow insets show the orientation of the incident **E** field to the aperture geometry.

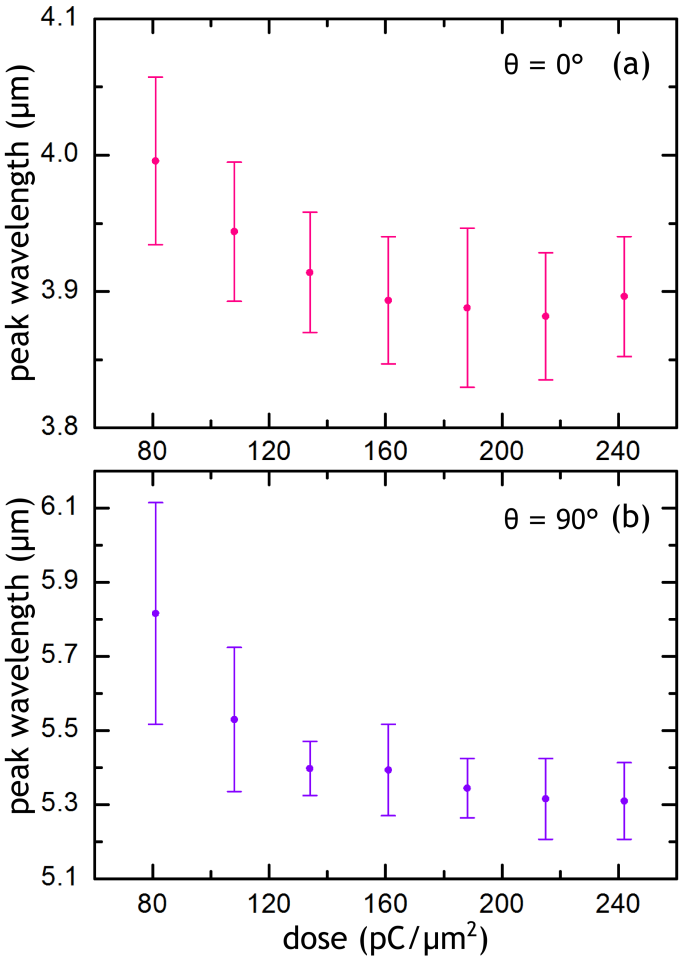


Figure 4.8: Transmission peak wavelength at ion beam dose of 81 pC/$\mu$m$^2$ and above at (a) polarisation $\theta = 0°$ and (b) polarisation $\theta = 90°$. The values are extracted from the spectra shown in Figure 4.7.

of apertures milled using an FIB dose of 242 pC/$\mu$m$^2$ were measured; the measured dimensions at this dose are $G_x$ = 490 nm, $G_y$ = 230 nm, $L_x$ = 1830 nm, $L_y$ = 1130 nm. In these simulations over-milling is defined as an increase in the parameter *d*, which is an extension of the aperture into the substrate. As $d$ increases a blue shift in the maximum transmission wavelength is observed. The blue shift magnitude decreases with increasing *d*. This is the same behaviour that we see in the experimental data; therefore the cause of the blue shift is most probably over-milling of the $CaF_2$ substrate. The absolute transmission peak values differ between the RCWA simulations and experimental results. This occurs partially because we have not increased the simulated aperture dimensions with dose, as occurs in the experiment. The variation between the simulated values and those of the apertures fabricated with an FIB dose of 242 pC/$\mu$m$^2$ suggests there may be other effects caused by gallium implantation which have resulted in the mismatch.

Figure 4.10 shows the maximum transmission at resonance as a function of dose for two **E** field polarisations, $\theta = 0°$ and $\theta = 90°$. There is zero transmission at zero dose as the metal film is opaque at the measured wavelengths. As the dose increases there is a large increase in transmission between dose 54 pC/$\mu$m$^2$ and 134 pC/$\mu$m$^2$. From dose 134 pC/$\mu$m$^2$ the maximum transmission then slowly increases. The initial rapid increase in transmission is caused by the removal of the metal layer. The maximum transmission through the array when $\theta = 0°$ is always less than the maximum transmission when $\theta = 90°$when the FIB dose is greater than 81pC/$\mu$m$^2$. This is because of geometry of the investigated aperture; $G_x$, the width of the cruciform arm which is aligned with incident **E** field when $\theta = 90°$, is greater than $G_y$, the width of the cruciform arm which is aligned

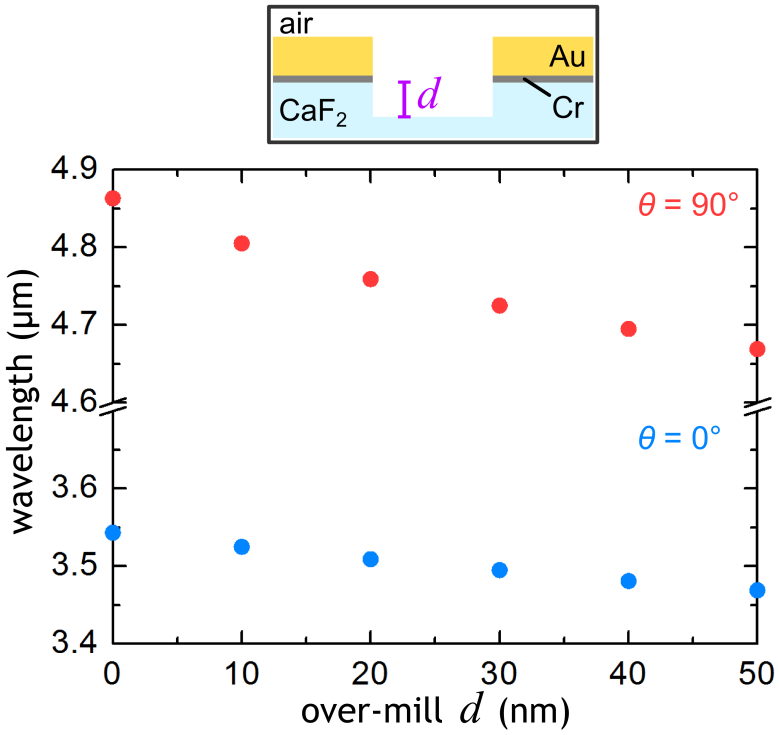


Figure 4.9: Transmission peak wavelength of the studied aperture geometry calculated using the rigorous coupled-wave analysis method for $\theta = 0°$ and $\theta = 90°$. $d$, the penetration into the $CaF_2$ substrate by over-milling, is varied. There is a break in the wavelength axis between 3.7 $\mu$m and 4.6 $\mu$m. The inset shows a schematic cross section of an over-milled aperture; the variable $d$ is shown in purple.

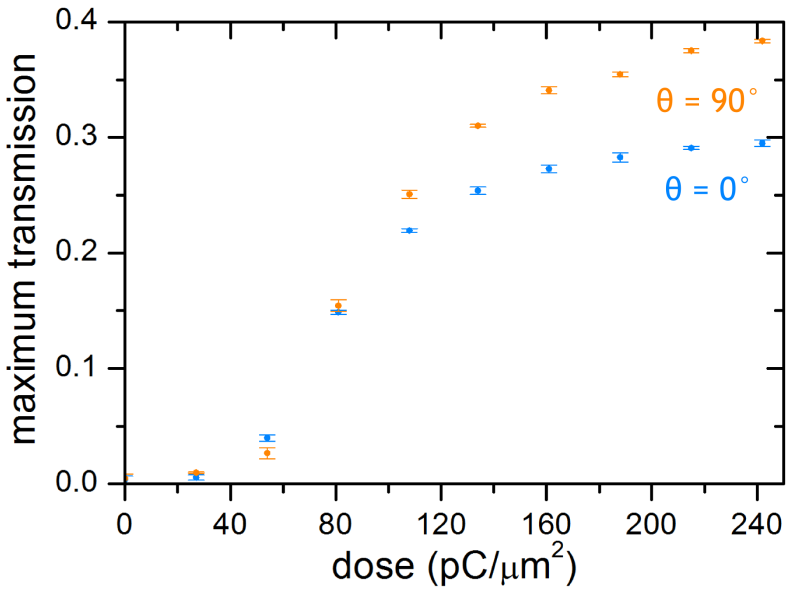


Figure 4.10: The maximum transmission through FIB fabricated arrays at $\theta = 0°$ (blue) and $\theta = 90°$ (orange) as a function of the FIB milling dose.

with the **E** field when $\theta = 0°$.

As we increase ion beam dose aperture area also increases (Figure 4.6). As this could be the cause of the steady increase in maximum transmission after the initial removal of the metal layers shown in Figure 4.10 we plot maximum transmission normalised to aperture area as a function of ion beam dose. Figure 4.11 shows the result of this normalisation. The transmission per unit area for polarisations $\theta = 0°$ and $\theta = 90°$ is seen to be approaching a maximum. This indicates that under-milling of the metal layer is the dominant form of attenuation for apertures of equal area.

The maximum transmission produced by FIB fabricated arrays is 38% which is small in comparison with arrays fabricated using the EBL/argon ion milling technique which have a maximum transmission of 79% (see Section 4.3). This may be caused by the differing interaction of the gallium and argon ions with the $CaF_2$ substrate as other changes in geometry are

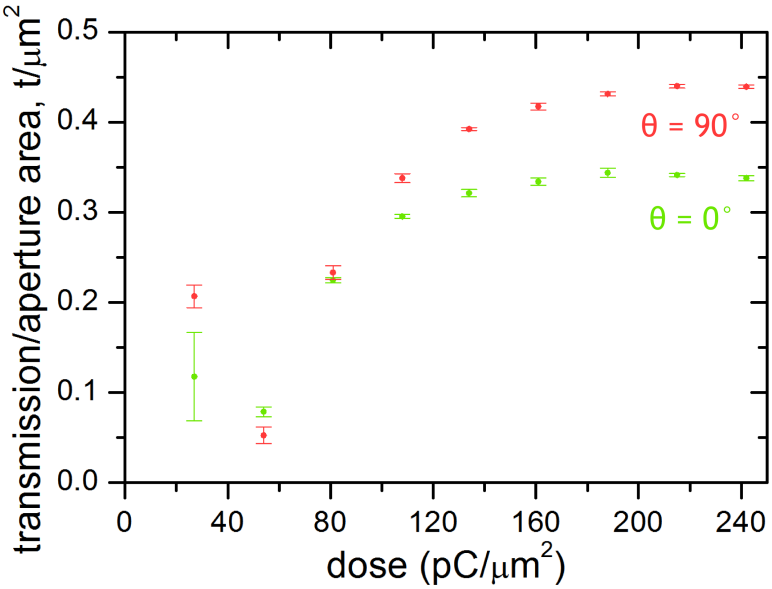


Figure 4.11: The maximum transmission through FIB fabricated arrays normalised to aperture area at $\theta = 0°$ (green) and $\theta = 90°$ (red) as a function of the FIB milling dose.

accounted for. This effect may be investigated quantitatively at some later date.

### 4.2.2 Resonance Matching Results

Following the fabrication of the asymmetric cruciform aperture array and the optical characterisation of its transmission spectrum detailed in Section 4.2 the array was spin coated with a solution of PMMA dissolved in anisole and baked to leave an 85 nm thick film of PMMA.

Figure 4.12 (a) shows the transmission spectrum of this asymmetric cruciform aperture array taken at two **E** field polarisations $\theta = 0°$ (green) and $\theta = 90°$ (blue). Broken lines show the transmission spectra of the uncoated aperture array, shown schematically in Figure 4.12 (b). Solid lines show transmission spectra from the aperture array coated with a 85 nm PMMA

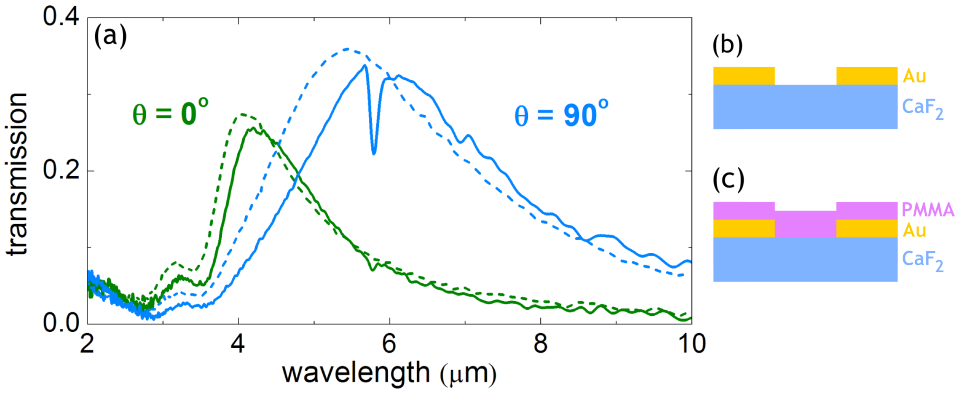


Figure 4.12: (a) Transmission spectra of an asymmetric cruciform aperture measured with **E** field polarisations $\theta = 0°$ (green) and $\theta = 90°$ (blue). For each polarisation there are two curves: the broken line shows the transmission of the uncoated array, the solid line shows the transmission of the array coated with PMMA. The local transmission minimum at wavelength 5.8 $\mu$m in the solid curves is produced by the PMMA carbonyl bond. (b) Schematic cross section of the uncoated array. (c) Schematic cross section of the coated array.

film, shown schematically in Figure 4.12 (c).

The transmission maximum of the apertures is present in the spectrum of both the coated and uncoated array for both polarisations. The transmission spectra of the PMMA coated array are red shifted with respect to the transmission spectra of the uncoated array. The red shift occurs because the addition of PMMA alters the refractive index of the surrounding dielectric medium from 1 (air) to approximately 1.48 (PMMA) [114]. Such index mediated red shifts of aperture transmission have been investigated experimentally using refractive index matching fluids [39]. The transmission maxima produced when $\theta = 0°$ and $\theta = 90°$ will be referred to as the global transmission maxima.

When the PMMA coated array is illuminated with $\theta = 90°$ polarised light the resultant transmission spectrum shows a local transmission minimum at wavelength 5.8 $\mu$m superimposed upon the global transmission maximum.

This local minimum is produced by the PMMA carbonyl bond and is not present in the spectrum of the uncoated arrays. The minimum may also be discernible in the $\theta = 0°$ transmission spectrum at 5.8 $\mu$m, however it is approaching the noise level.

To investigate the relation of the PMMA carbonyl bond spectrum to incident **E** field polarisation a series of transmission and reflection measurements were made at 22.5° intervals from $\theta = 0°$ to $\theta = 90°$. The transmission $T$ and reflection $R$ of the structure was measured using FTIR. Background measurements were taken through the $CaF_2$ substrate and from an uncoated area of gold film for measurements of transmission and reflection respectively. The absorption $A$ of the structure was extracted for each polarisation using the relation $A = 1 - T - R$. Both the reflection and transmission FTIR measurements were taken from the PMMA-coated face of the structure (see Figure 4.12 (c)).

Figure 4.13 shows the reflection, transmission and absorption spectra of the PMMA coated aperture array in the region of the carbonyl bond wavelength. The reflection spectrum of the PMMA coated array has a global minimum that occurs at a wavelength between 5.6 $\mu$m and 6 $\mu$m when $\theta = 90°$. This global reflection minimum, produced by the aperture array, reduces in magnitude as the polarisation is rotated away from $\theta = 90°$ and completely disappears when $\theta = 22.5°$. Superimposed upon the global reflection spectrum is the local reflection spectrum created by the PMMA carbonyl bond at wavelength 5.8 $\mu$m. When $\theta = 90°$ the carbonyl bond produces a reflection maximum, this maximum decreases in magnitude as the polarisation is rotated away from $\theta = 90°$ and then inverts at an **E** field polarisation between $\theta = 45°$ and $\theta = 22.5°$. At $\theta = 22.5°$ and $\theta = 0°$ the carbonyl bond produces a local reflection minimum. The reflectivity therefore

decreases with respect to the base line for small values of $\theta$, and increases above the base line for large values of $\theta$. This phenomenon we refer to as *absorption induced reflectivity*. This is the reflection analogue of absorption induced transparency, where transmission is seen to be larger than the base line value despite the presence of a lossy dielectric [54].

The transmission spectrum of the PMMA coated array has a global maximum that occurs at a wavelength between 5.6 $\mu$m and 6 $\mu$m when $\theta = 90°$. This global transmission maximum, produced by the aperture array, reduces in magnitude as the polarisation is rotated away from $\theta = 90°$ and disappears when $\theta = 45°$. Superimposed upon the global transmission spectrum is the local transmission spectrum created by the PMMA carbonyl bond at wavelength 5.8 $\mu$m. When $\theta = 90°$ the carbonyl bond produces a carbonyl mediated transmission minimum, which decreases in magnitude as the **E** field polarisation is shifted away from $\theta = 90°$ and is reduced to its smallest size at $\theta = 0°$.

The absorption spectrum of the PMMA coated array has a global maximum that occurs at a wavelength between 5.7 $\mu$m and 6.6 $\mu$m when $\theta = 90°$. The absorption in this wavelength range decreases as the **E** field polarisation is shifted away from $\theta = 90°$ and reaches a minimum value when $\theta = 0°$. Superimposed upon the global absorption spectrum is the local absorption spectrum produced by the PMMA carbonyl bond at wavelength 5.8 $\mu$m. In this data set the local carbonyl absorption has a maximum value at $\theta = 0°$, the absorption of the carbonyl bond decreases as the **E** field polarisation is rotated away from $\theta = 0°$ and appears to reach a minimum value at $\theta = 90°$.

To compare the experimental analysis of the array with theoretical predictions, a series of simulations was undertaken with the aim of modelling the fabricated device. The simulation of the device was initially done by Claudiu

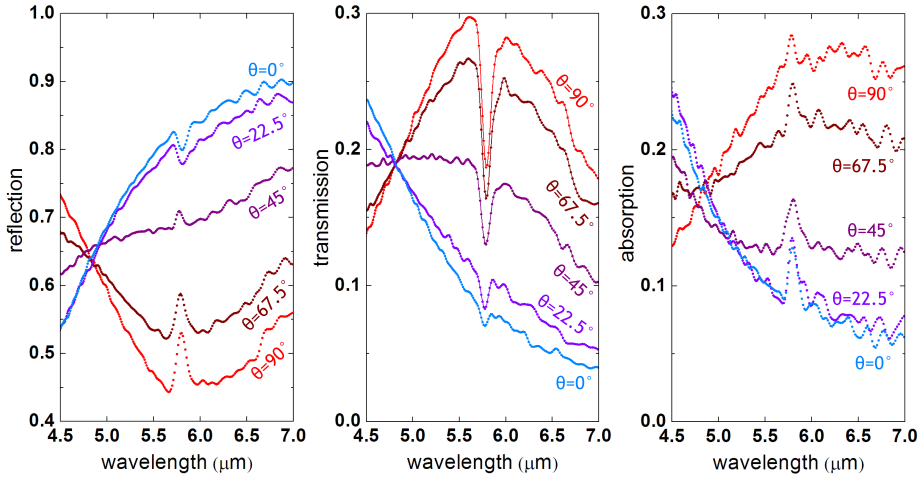


Figure 4.13: Reflection, transmission and absorption spectra of an aperture array coated with 85 nm PMMA film taken at 22.5° intervals from $\theta = 0°$ (blue) to $\theta = 90°$ (red). The reflection and transmission spectra were measured using FTIR. The absorption data were extracted for each polarisation using the relation $A = 1 - T - R$.

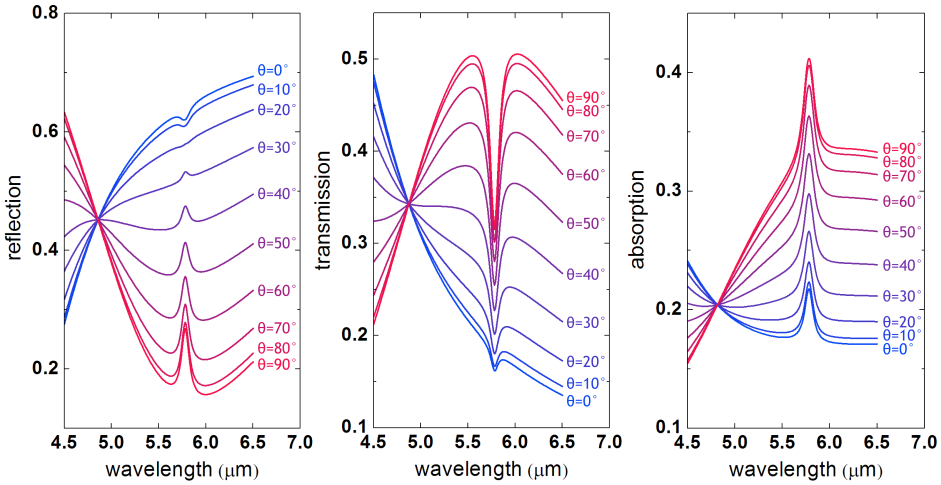


Figure 4.14: Reflection, transmission and absorption spectra of an aperture array coated with 85 nm PMMA film simulated using the rigorous coupled-wave analysis method. Spectra were calculated at 10° intervals from $\theta = 0°$ (blue) to $\theta = 90°$ (red).

Biris, University College London. He used the commercially available RSoft DiffractMOD software which implements the rigorous coupled-wave analysis method. The refractive index and dimensions of components of the device geometry were determined to create a numerical model. A constant refractive index of 1.4 was used for the $CaF_2$ substrate. To account for dispersion a Lorentz-Drude model for the refractive index of the gold and chromium layers was applied [115]. To model the attenuation at the carbonyl bond wavelength the PMMA layer was represented by a complex refractive index, $\tilde{n} = n + i\kappa$. The attenuation produced by the carbonyl bond was modelled by defining the imaginary part the Lorentz function

$$\kappa = P_1 + \frac{P_2}{\pi} \frac{P_3}{(\lambda - \lambda_0)^2 + P_3^2} \tag{4.1}$$

and fitting this to the measured transmission spectrum of an 85 nm thick PMMA film at the carbonyl bond wavelength, $\lambda_0 = 5.782\ \mu$m (the spectrum is shown in Figure 4.2). The $P$ parameters of the Lorentz function were adjusted using the least squares method until the transmission spectrum produced by the simulation closely matched that of the measured PMMA spectrum in the region of the carbonyl bond wavelength. Following the fitting the $P$ parameters were set as $P_1 = 0$, $P_2 = 0.216$ and $P_3 = 0.0465$. The refractive index at all other wavelengths was kept constant, $n = 1.4$. An SEM image of the array was used to determine the aperture dimensions that were used in the simulation. Rounded edges and surface roughness were neglected.

Figure 4.14 shows the results of these simulations. Reflection, transmission and absorption spectra were calculated at 10° intervals from $\theta = 0°$ to $\theta = 90°$.

The calculated reflection spectra show qualitatively similar features to those measured experimentally using FTIR. When $\theta = 90°$ there is a global minimum produced by the aperture array at approximately 6 $\mu$m wavelength, this minimum reduces in magnitude as $\theta$ is rotated towards $\theta = 0°$. The minimum at 6 $\mu$m completely disappears when $\theta = 20°$. When $\theta = 90°$ there is a local reflection maximum at wavelength 5.78 $\mu$m, this feature is produced by the complex refractive index model of the carbonyl bond. The magnitude of this local maximum reduces as the **E** field polarisation is rotated away from 90°. At $\theta = 20°$ the carbonyl bond reflection minimum is almost indistinguishable from the global spectrum produced by the aperture array. When $\theta = 10°$ and $\theta = 0°$ the carbonyl bond produces a local reflection minimum. The same behaviour is observed in the measured device where there is an inversion of the local feature produced by the carbonyl bond at similar **E** field polarisations.

The calculated transmission spectra also show qualitatively similar features to those measured using FTIR. However the spectral feature produced by the carbonyl bond resonance is a minimum at all polarisations and does not invert. In both the reflection and transmission spectra the magnitude of the global reflection minimum and transmission maximum measured using FTIR is less than that calculated numerically, this is because defects (*e.g.* surface roughness and ion beam damage) are not included in the model.

The absorption $A$ is extracted using the relation $A = 1 - T - R$. There is a local absorption maximum produced by the simulated carbonyl bond at wavelength 5.78 $\mu$m superimposed upon a global absorption spectrum produced by the apertures. Both the global aperture absorption spectrum and the local simulated carbonyl bond absorption are maximum when $\theta = 90°$. As the **E** field polarisation is rotated away from $\theta = 90°$ the absorption of

the structure and the simulated carbonyl bond decrease, with both reaching a minimum when $\theta = 0°$.

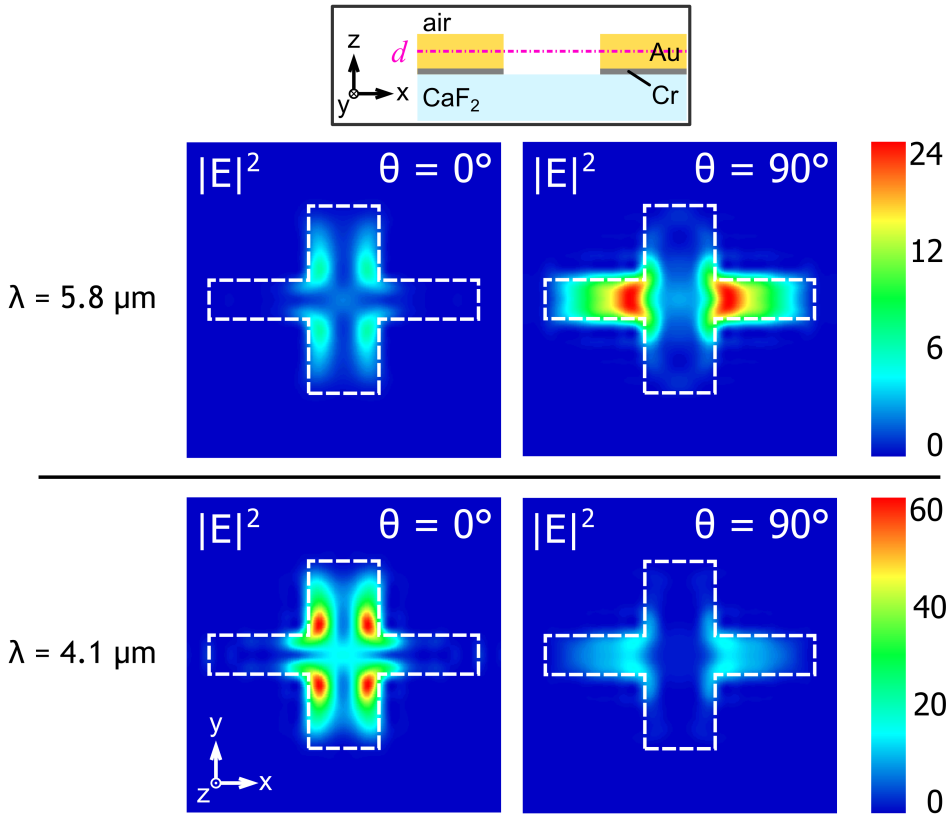


Figure 4.15: $|\mathbf{E}|^2$ distribution for two incident polarisations $\theta = 0°$ and $\theta = 90°$. The distributions are calculated at a plane intersecting the $z$ axis at $d = 23$ nm (half way through the gold layer), shown in the schematic cross section by the broken pink line, the $CaF_2$ substrate surface is at the origin of the $z$ axis. The dashed white lines placed on the field profiles show the aperture boundary. The fields are calculated at wavelengths 4.1 $\mu$m and 5.8 $\mu$m corresponding to the short and long wavelength transmission maxima produced by the aperture. Calculations were performed by Claudiu Biris.

The **E** field profiles produced by the apertures were also simulated. Figure 4.15 shows $|\mathbf{E}|^2$ at a cross section through the centre of an aperture at $\theta = 0°$ and $\theta = 90°$. The field profiles were calculated at wavelengths 4.1 $\mu$m and 5.8 $\mu$m corresponding to the two global transmission peaks produced by the aperture. The field profiles indicate that at wavelength 5.8 $\mu$m the

maximum field is produced when $\theta = 90°$ and at wavelength 4.1 $\mu$m the maximum field is produced when $\theta = 0°$. As the carbonyl bond is resonant at approximately wavelength 5.8 $\mu$m and the absorption of a material is directly proportional to $|\mathbf{E}|^2$ the bond absorption should be maximum when $\theta = 90°$. This concurs with the simulated absorption spectra shown in Figure 4.14. Although this trend is not reproduced in the experimental data shown in Figure 4.13 an increase in absorption that follows the trend is observed in samples produced by EBL (Figure 4.24 (a)). The low absorption observed in the FIB fabricated sample may be a result of noise when measuring an array of the limited size that can be fabricated by FIB milling or be an effect of gallium ion implantation during fabrication. In order to improve the signal to noise ratio and accuracy of the transmission and reflection measurements larger area arrays needed to be produced. EBL is an alternative fabrication technique that can produce larger area arrays. The results of this fabrication are shown in the following sections.

## 4.3 Electron Beam Lithography Fabrication of Asymmetric Cruciform Apertures

To improve the signal to noise ratio of the spectroscopic measurements we decided to alter the fabrication method. Our EBL system has a 10000 $\mu m^2$ write field allowing fabrication of apertures in arrays over nine times the area of the original FIB milled array. Arrays of asymmetric cruciform apertures consisting of 46 $\times$ 46 unit cells were fabricated using EBL and argon ion milling of an (approximately) 35 nm gold and 5 nm chromium metal layer on a 1 mm thick $CaF_2$ substrate. The metal layers were deposited using the same procedure as for the FIB fabrication process.

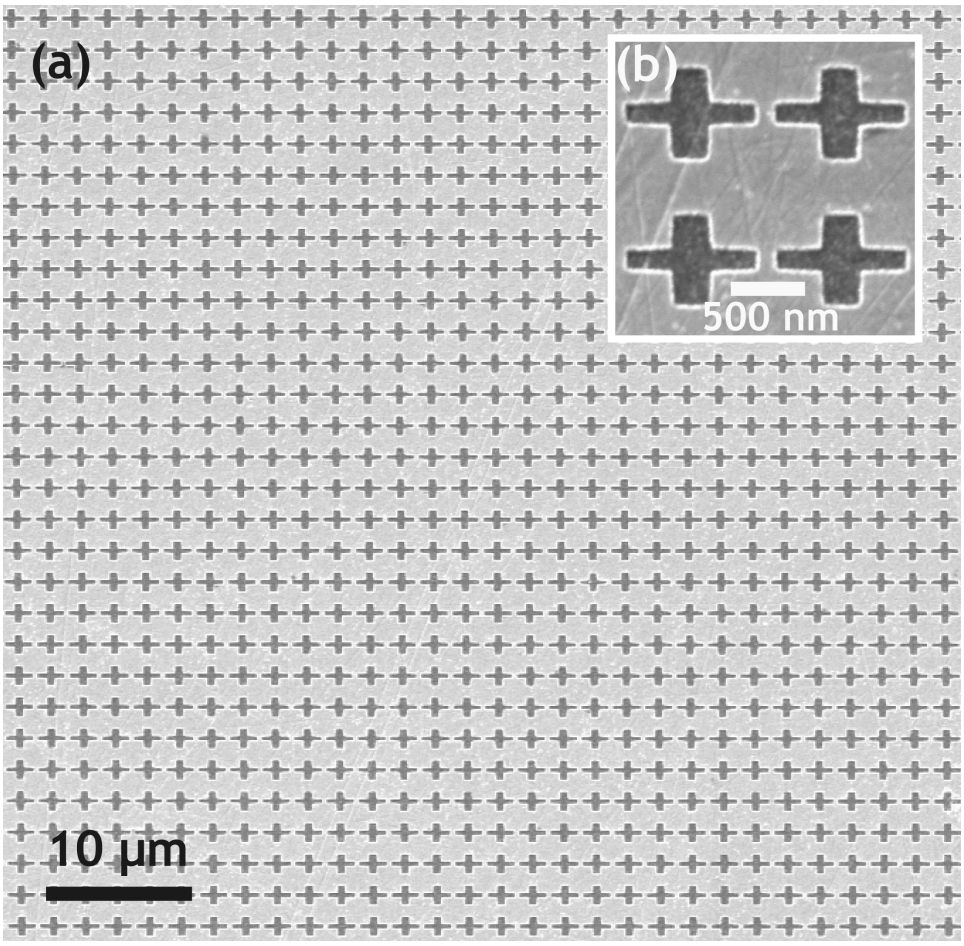


Figure 4.16: (a) Scanning-electron micrograph showing part of the cruciform aperture array fabricated using EBL and argon ion milling. The array is shown before PMMA coating. (b) Magnified detail of four apertures.

Figure 4.16 shows SEM micrographs of a typical aperture array produced by the EBL fabrication method. The apertures shown have mean dimensions $L_x = 1870$ nm, $L_y = 1290$ nm, $G_x = 520$ nm and $G_y = 270$ nm and pitch in $x$ and $y$ of 2100 nm. The standard deviation of dimension measurements taken from eight arrays fabricated by EBL is 8 nm, which compares favourably with the same measurements made for arrays fabricated by FIB which have a standard deviation of 21 nm. The increase in sample uniformity may improve the spectroscopic measurements; however this has not been investigated systematically.

Three different-sized apertures were fabricated using the EBL and argon ion milling technique. The apertures were arranged in three arrays, labelled A, B and C, with each array containing only one size of aperture. The size of aperture contained within each array increases from smallest in A, to largest in C. Measurements of the parameters $L_x$, $L_y$, $G_x$ and $G_y$ (see Figure 4.3 (c)) were taken from six apertures from each of the three arrays and their mean value calculated; the aperture pitch was 2100 nm in $x$ and $y$ in all cases. The resultant array aperture dimensions are shown in Table 4.1.

| Array | $L_x$ (nm) | $L_y$ (nm) | $G_x$ (nm) | $G_y$ (nm) | Spectra |
|---|---|---|---|---|---|
| A | 1520 | 1080 | 500 | 310 | Fig. 4.17 (a) |
| B | 1910 | 1350 | 620 | 390 | Fig. 4.17 (b) |
| C | 2290 | 1600 | 740 | 470 | Fig. 4.17 (c) |

Table 4.1: The dimensions of the apertures in arrays A, B and C, fabricated using the EBL and argon ion milling technique.

Figure 4.17 shows the transmission spectra of the three asymmetric cruciform aperture arrays. The spectra are taken at three **E** field polarisations $\theta = 0°$ (red), $\theta = 45°$ (green) and $\theta = 90°$ (blue). Broken lines show the transmission spectra of uncoated aperture arrays and solid lines show the

transmission of aperture arrays coated with an 85 nm PMMA film.

The EBL fabricated apertures arrays have qualitatively similar transmission characteristics to the apertures arrays produced by FIB milling (see Section 4.2.2 and Figure 4.12). There are two global transmission peaks, one produced when $\theta = 0°$ and one when $\theta = 90°$; the transmission of the PMMA-coated arrays is red shifted with respect to the uncoated arrays; and there is a local transmission minimum at wavelength 5.79 $\mu$m produced by the PMMA carbonyl bond. However the EBL fabricated arrays have a maximum transmission of 79% (array B, Figure 4.17 (b), $\theta = 90°$) compared with a maximum achieved transmission of 38% for the FIB fabricated arrays (Figure 4.7 (b) $\theta = 90°$ dose 242 pC/$\mu$m$^2$). This is thought to be the result of a larger volume of the $CaF_2$ substrate beneath the apertures becoming amorphous when scanned by the gallium ion beam used in the FIB process, and a smaller volume of the substrate becoming amorphous when exposed to the argon ions used in the EBL process. This is because the FIB gallium ions are much more energetic than the argon ions, resulting in a greater penetration depth and greater degradation of the substrate. The improved transmission of the EBL fabricated arrays and the increase in array area enabled by the EBL technique (resulting in an improvement in the signal to noise ratio) resulted in this fabrication technique being used for the rest of the investigation.

The relative size of the apertures is shown in the insets to Figure 4.17. An increase in aperture dimensions causes the resonant frequency of the apertures to shift to longer wavelength. This resonance shift is predominantly produced by changes in the length of the cross arms, $L_x$ and $L_y$. This was shown by Thompson *et al.*, who systematically varied the length of $L_y$ form 882 nm to 1236 nm whilst keeping other dimensions constant

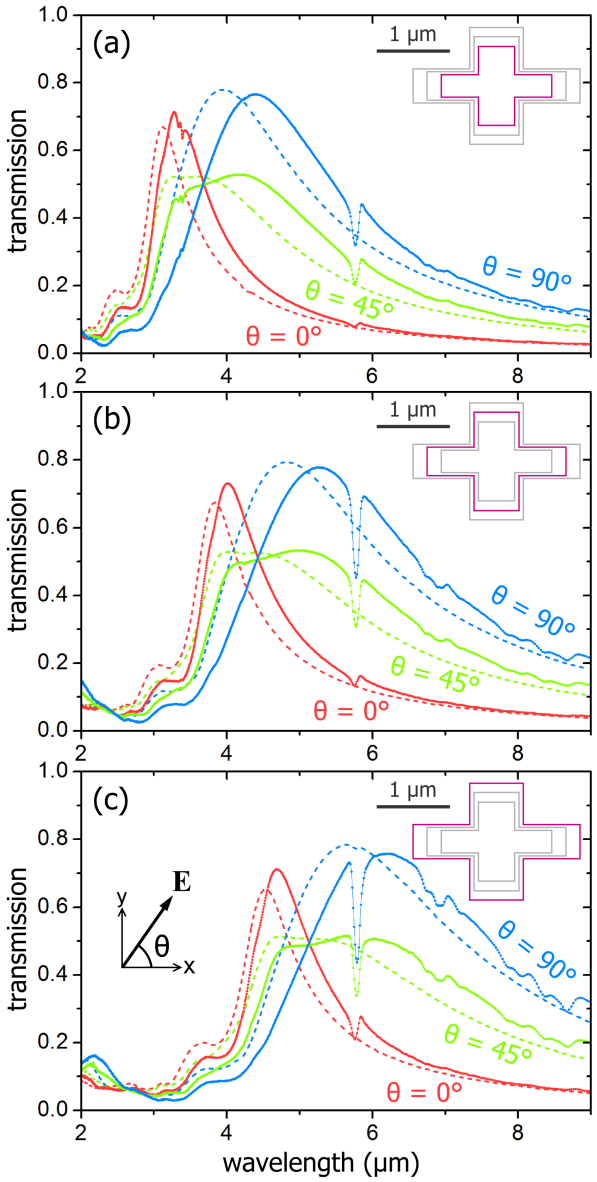


Figure 4.17: Transmission spectra of three asymmetric cruciform aperture arrays measured with **E** field polarisations $\theta = 0°$ (red), $\theta = 45°$ (green) and $\theta = 90°$ (blue). The broken lines show the transmission of the uncoated array, the solid lines show the transmission of the array coated with PMMA. (a) Apertures with mean area 0.85 $\mu m^2$. (b) Apertures with mean area 1.34 $\mu m^2$. (c) Apertures with mean area 1.91 $\mu m^2$. An inset showing a scale schematic of the geometry of the three apertures is placed in each panel, the geometry relevant to the panel spectra is highlighted in red. The **E** field polarisation angle in reference to the aperture geometry is shown by the vector schematic inset to (c).

and observed a red shift in the short wavelength ($\theta = 0°$) peak [6].

The shift in resonant frequency of the apertures also affects the interaction of the plasmonic system with the PMMA carbonyl bond. When the carbonyl bond resonance is far from the resonance of the excited plasmonic mode there is little change in the global transmission spectrum at the carbonyl bond wavelength 5.79 $\mu$m. If the excited plasmon mode is produced at a wavelength which is close to the carbonyl bond resonance then a pronounced change in the global transmission spectra at the bond wavelength will occur. This can be seen by comparing the spectra produced by apertures A and C when they are illuminated by light with **E** field polarisation $\theta = 0°$ (see Figure 4.17 (a) and (c) solid red curves). When array A is illuminated with polarisation $\theta = 0°$ the plasmon resonance produces maximum transmission at wavelength 3.28 $\mu$m, there is a very small feature in the spectrum at the carbonyl bond wavelength 5.79 $\mu$m. When array C is illuminated with polarisation $\theta = 0°$ the plasmon resonance produces maximum transmission at wavelength 4.68 $\mu$m, the local feature produced by the carbonyl bond is much larger than that seen in array A. This effect can also be seen in the $\theta = 90°$ plasmon resonance.

To further investigate the plasmon molecular interactions that forms the spectral feature seen at the carbonyl bond wavelength the system was modelled theoretically; this modelling is the subject of the following sections.

## 4.4 The Fano Resonance in Asymmetric Cruciform Apertures

### 4.4.1 Mechanical Modeling of Plasmon-Molecule Interactions

The interference of broad and narrow resonances may produce an asymmetric line shape. This resonance was first described theoretically by Fano [23]. Fano's description is discussed in the theoretical introduction. Classical analogies of Fano's quantum mechanical system use coupled resonators driven in simple harmonic motion to produce spectra that exhibit the Fano line shape [32, 34]. These systems consist of two masses coupled by springs (one of them is a highly damped oscillator driven by an external force, the other a lightly damped oscillator which is only excited by interaction with the other mass, see Section 2.4.2).

Our experimental system is characterised by two orthogonal plasmon modes, which are excited by incident radiation, and a molecular resonance which either interacts with the plasmonic fields only or with a combination of plasmonic field and external excitation. To investigate the interactions occurring within this plasmon-molecular system we have modeled the system using a classical coupled resonator model. In this model the broad plasmon modes are represented by the highly damped oscillators and the narrow molecular resonance by a lightly damped oscillator. To apply this classical resonator model to the investigated system the existing two-mass model was expanded to include an additional highly damped oscillator. Our model contains three masses: two externally driven masses representing the two plasmon resonances and one mass representing the molecular resonance.

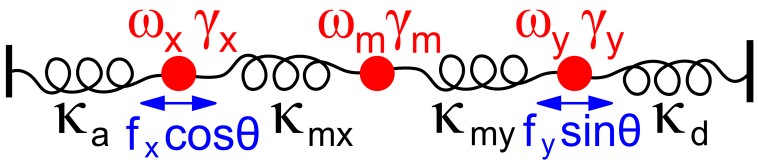


Figure 4.18: Mechanical representation of the classical resonators used to model the plasmonic system. Three balls (red) designated $x$, $y$ and $m$ with resonant frequencies $\omega_x$, $\omega_y$, $\omega_m$ and damping $\gamma_x$, $\gamma_y$, $\gamma_m$ respectively are attached to each other and two immovable walls by springs with spring constants $\kappa_a$, $\kappa_{mx}$, $\kappa_{my}$ and $\kappa_d$. Balls $x$ and $y$ are driven by driving force $f_x$ and $f_y$ respectively with magnitudes that are dependent on $\theta$.

### Mechanical Model Derivation

Figure 4.18 shows the mechanical system schematically. Three masses designated $x$, $y$ and $m$ have resonant frequencies $\omega_x$, $\omega_y$, $\omega_m$ and damping $\gamma_x$, $\gamma_y$, $\gamma_m$ respectively. The masses are attached in series to each other and to two immovable walls by four springs. The spring connecting masses $m$ and $x$ has spring constant $\kappa_{mx}$ and the spring connecting masses $m$ and $y$ has spring constant $\kappa_{my}$; masses $x$ and $y$ are connected to the immovable walls by springs with spring constants $\kappa_a$ and $\kappa_d$ respectively. Masses $x$ and $y$ represent the orthogonal plasmon modes and are driven by external excitations $\Phi_x$ and $\Phi_y$ with magnitudes $f_x$ and $f_y$:

$$\begin{aligned} \Phi_{x,y} &= F_{x,y}\mathrm{e}^{i\omega t}, \\ F_x &= f_x \cos\theta, \\ F_y &= f_y \sin\theta. \end{aligned} \tag{4.2}$$

$f_x$ and $f_y$ represent the coupling of the plasmon modes to incident light. $\theta$ is the **E** field polarisation of the incident light. As the plasmon modes are orthogonal a sinusoidal relationship between $f_x$, $f_y$ and $\theta$ was initially investigated. Mass $m$, which represents the carbonyl bond, is initially taken as interacting with masses $x$ and $y$ only and not the external environment,

hence $F_m = 0$. As only positive frequencies are of interest first order equations of motion may be used to determine the displacements $a_x$, $a_y$ and $a_m$ of the masses. The first order equations of motion of the system may be written using the complex form of simple harmonic motion; following the application of the conservation of energy (see Appendix B) this results in:

$$\begin{aligned} -i\dot{a}_x - i\gamma_x a_x - \omega_x a_x + i\kappa_{mx} a_m &= -f_x \cos\theta \mathrm{e}^{i\omega t} \\ -i\dot{a}_y - i\gamma_y a_y - \omega_y a_y + i\kappa_{my} a_m &= -f_y \sin\theta \mathrm{e}^{i\omega t} \\ -i\dot{a}_m - i\gamma_m a_m - \omega_m a_m - i\kappa^*_{mx} a_x - i\kappa^*_{my} a_y &= 0 \end{aligned} \tag{4.3}$$

where Newton's dot notation is used to represent the time derivative.

The solution to Equations 4.3 can be expressed in complex form as $a(t) = a\mathrm{e}^{i\omega t}$. This solution is inserted into the equation, which is differentiated and $\mathrm{e}^{i\omega t}$ factored out, resulting in the following equations of motion

$$\begin{aligned} a_x(\omega - \omega_x - i\gamma_x) + i\kappa_{mx} a_m &= -\mathrm{f}_x \cos\theta \\ a_y(\omega - \omega_y - i\gamma_y) + i\kappa_{my} a_m &= -\mathrm{f}_y \sin\theta \\ a_m(\omega - \omega_m - i\gamma_m) - i\kappa^*_{mx} a_x - i\kappa^*_{my} a_y &= 0 \end{aligned} \tag{4.4}$$

This system of linear equations may be solved analytically using Cramer's rule [94]. As the solutions of $a_x$, $a_y$ and $a_m$ are very long they are not shown here. The output of the model $M$ is the magnitude sum of oscillation of the masses $x$ and $y$, $M = |a_x|^2 + |a_y|^2$; $a_m$ is neglected as the molecule does not interact outside the plasmon-molecular system.

### Modeling Transmission and Reflection

When modeling a transmission spectrum the amplitude $M$ is considered to be equivalent to the amplitude of the transmitted light. This is because the amplitude of light emitted at a certain frequency is analogous to the ampli-

tude of the mass oscillation at that driving frequency. The transmitted light may be thought of as the output of a radiator; light incident on the perforated metal film is coupled to LSPs, and these plasmons produce radiation on the other side of the film which is detected and forms the transmission spectrum. This is not the case when modeling a reflection spectrum as the reflection minimum present in the measured spectrum is produced by the coupling of the incident light to LSPs only. Measured reflection is therefore equivalent to $1 - M$, as resonance of the plasmonic structure produces an increase in the coupling of light and a corresponding decrease in reflection.

Since the resonance characteristics in both transmission and reflection are thought to be the same, $M$ models transmission and $1 - M$ models reflection. A consequence of this approach is that the model assumes zero absorption, with perfect transmission through the perforated metal film. This is not the case in our system as intrinsic losses are produced by the metal film, surface roughness, ion damage *et cetera*. The simplification results in the fitted parameters for the reflection and transmission spectra not being equal as the spectra are fitted separately and these parameters would only be equal if there was zero absorption.

**Experimental Results**

The system constants $\omega_x$, $\omega_y$, $\omega_m$, $\gamma_x$, $\gamma_y$, $\gamma_m$ and $\theta$ may be extracted from experimental data (details are given for the experimental data shown below). This leaves variables $\kappa_{mx}$, $\kappa_{my}$, $f_x$ and $f_y$ that may be determined by fitting the system to experimental data. To determine the unknown variables the system of equations is solved and $M$ is subtracted from the experimental data giving an error vector. Nonlinear minimisation of the sum of the squares of the error vector is used to alter the variables until the best fit

is found; *fminsearch* is the Matlab function used to implement this least squares fitting. The Matlab code used is reproduced in Appendix C.

An array of apertures with dimensions $L_x = 1900$ nm, $L_y = 1340$ nm, $G_x = 580$ nm and $G_y = 360$ nm and pitch in $x$ and $y$ of 2.1 $\mu$m was produced using the EBL/Ar ion milling technique. It was subsequently coated with an 85 nm thick film of PMMA. The sample was illuminated with linearly polarised light and the reflection and transmission spectra measured using an FTIR microscope for polarisation values from $\theta = 0°$ to $\theta = 90°$ at $\theta = 10°$ intervals. Figures 4.19 (a) and 4.20 (a) show the measured data for reflection and transmission respectively ($\theta = 10°$ and $\theta = 80°$ are omitted for clarity).

To produce small values of $\omega_x$, $\omega_y$, $\omega_m$ and $\gamma_x$, $\gamma_y$, $\gamma_m$ the output of the FITR was converted from $cm^{-1}$ to $\mu m^{-1}$ and these units used throughout the simulation. Values of $\omega_{x,y,m}$ and $\gamma_{x,y,m}$ are measured from the FTIR data. For $\omega_x$ and $\omega_y$ the wavenumbers of the global resonant peaks produced at $\theta = 0°$ and $\theta = 90°$ respectively are used.

### Estimation of $\gamma_x$ and $\gamma_y$

The global transmission and reflection spectra formed by the LSP resonances are asymmetrical. This asymmetry results in the constants $\gamma_x$ and $\gamma_y$ being difficult to determine. Initially the measured full width half maximum of the curve was used. However because the global resonance produced by model is symmetric the output did not match the global plasmon spectrum. It was therefore impossible to accurately determine the variable values required to reproduce the reflection and transmission spectra at the carbonyl bond wavelength. In order to produce an accurate fit at the carbonyl bond wavelength the full width half maximum that would be produced if the mea-

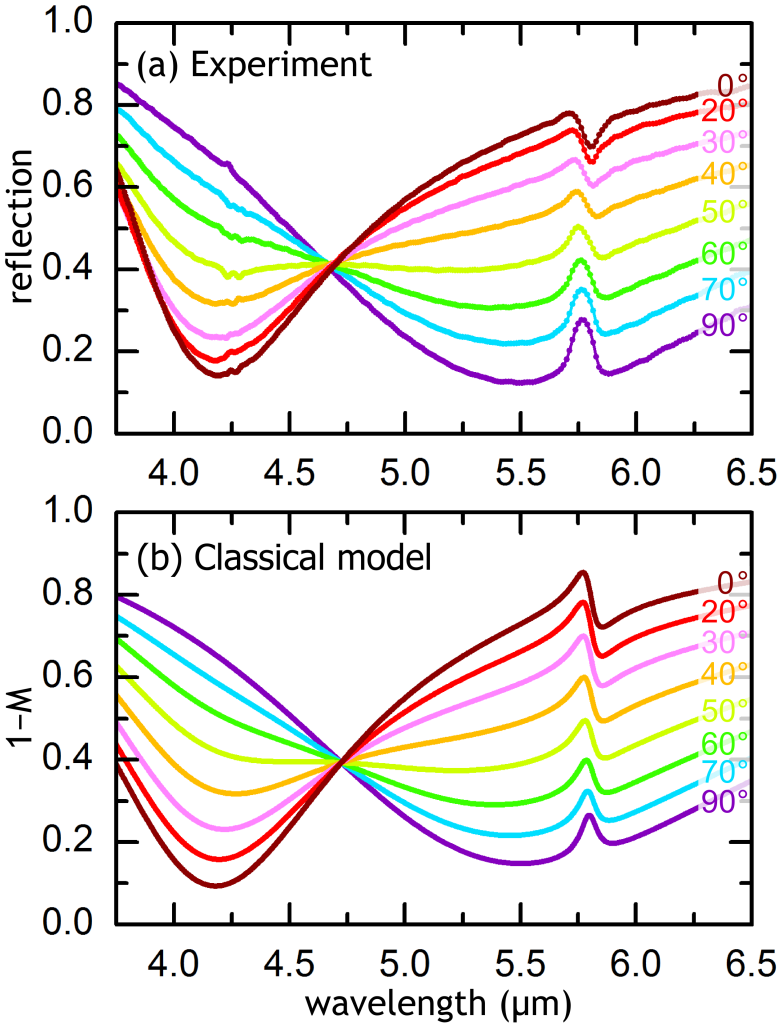


Figure 4.19: (a) Reflection spectrum of a PMMA-coated cruciform aperture array measured using FTIR. (b) Best fit of experimental data using the classical model. Curves are labeled with their corresponding polarisation $\theta$.

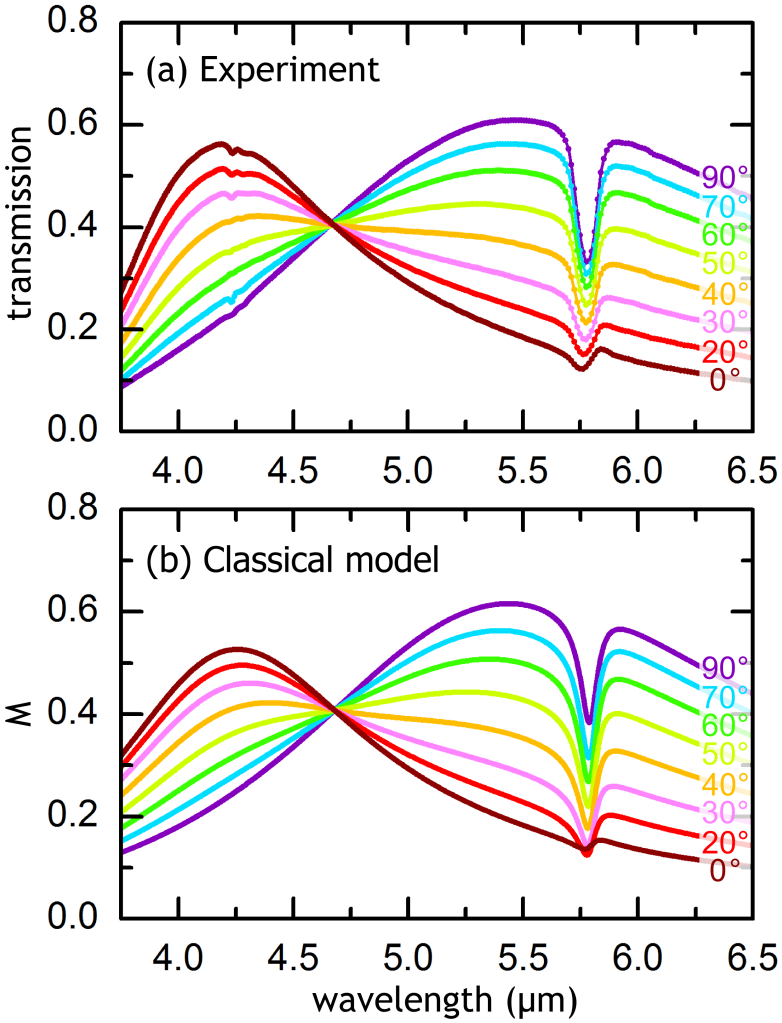


Figure 4.20: (a) Transmission spectrum of a PMMA-coated cruciform aperture array measured using FTIR. (b) Best fit of experimental data using the classical model. Curves are labeled with their corresponding polarisation $\theta$.

sured global resonance were symmetrical was extracted. Figure 4.21 shows the two damping values $\gamma_a$ and $\gamma_b$ that can be extracted from the asymmetrical global plasmon resonance. The asymmetry of the curve causes $\gamma_a$ to be larger than $\gamma_b$. As we are interested in the coupling of the plasmon resonances with the carbonyl bond the region of the measured spectrum that includes the carbonyl bond resonance was used to extract a damping value that would model this resonance accurately. Figure 4.21 shows this schematically. In the figure $\gamma_a$ corresponds to the full width half maximum that would be used in the model.

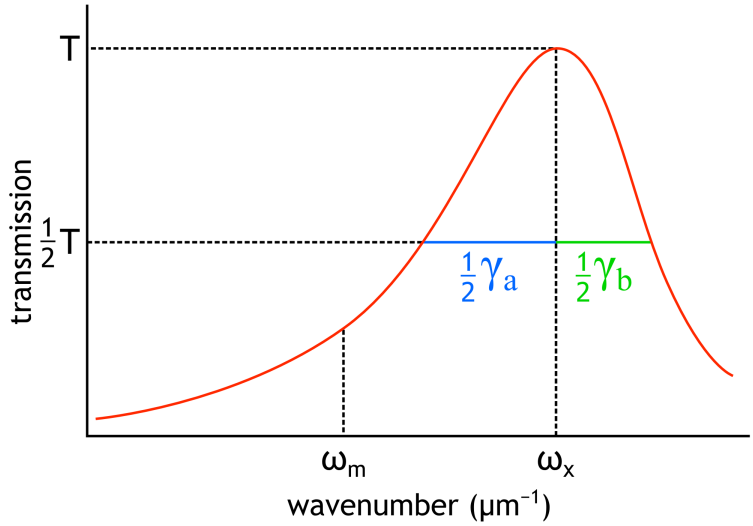


Figure 4.21: Sketch showing $\gamma$ values for an asymmetrical plasmon resonance where $\gamma_a > \gamma_b$. $\omega_m$ is the molecular bond resonance and $\omega_x$ is the plasmon resonance. T is the maximum transmission produced by the plasmon resonance.

### Free Parameter Estimation

Initial conditions for $f_x$, $f_y$, $\kappa_{mx}$ and $\kappa_{my}$ were selected so that the curve $M(\omega)$ lies close to the experimental data that is to be modeled. The imaginary parts of the $\kappa$ variables were initially zero. For a spectrum measured

with incident **E** field polarisation $\theta$, the value of $\theta$ was defined and the fitting routine was then run, producing estimates of the variables. This was repeated at all measured values of $\theta$, resulting in estimates for the variables at each measured polarisation. It was found that using a mean of the fitted variables from all polarisations did not produce an accurate representation of the experimental data. This is because of the sinusoidal component of $F_{x,y}$. When $\theta = 0°$ and $10°$ the $x$ terms dominate and when $\theta = 80°$ and $90°$ the $y$ terms dominate. For values of $\theta$ between $20°$ and $70°$ there is a mix of $x$ and $y$ terms.

We wish to determine values of $f_{x,y}$, $\mathrm{Re}(\kappa_{mx,my})$ and $\mathrm{Im}(\kappa_{mx,my})$ that produce accurate predictions of the reflection and transmission of the measured device for all incident **E** field polarisations. To find these values the mean of fitting parameters extracted from polarisations $\theta = 0°$ and $10°$ were used for $f_x$, $\mathrm{Re}(\kappa_{mx})$ and $\mathrm{Im}(\kappa_{mx})$ and the mean of fitting parameters extracted form polarisations $\theta = 80°$ and $90°$ were used for $f_y$, $\mathrm{Re}(\kappa_{my})$ and $\mathrm{Im}(\kappa_{my})$. Table 4.2 shows the result of this extraction. To simulate the reflection and transmission spectra that would be produced by the values shown in Table 4.2, these values were inserted into the model and $1 - M(\lambda)$ (for reflection) and $M(\lambda)$ (for transmission) were calculated for variable values of $\theta$. Figures 4.19 (b) and 4.20 (b) show the output of these simulations.

| Spectra | $f_x$ | $f_y$ | $\mathrm{Re}(\kappa_{mx})$ | $\mathrm{Im}(\kappa_{mx})$ | $\kappa_{my}$ | $i\kappa_{my}$ |
|---|---|---|---|---|---|---|
| Reflection | 0.0378 | 0.0444 | 0.0033 | -0.0048 | 0.0020 | 0.00050 |
| Transmission | 0.0286 | 0.0342 | 0.0028 | 0.0011 | 0.0035 | -0.00043 |

Table 4.2: Fitting output of the mechanical model. Values used to produce Figures 4.19 (b) and 4.20 (b).

**Polarisation dependence of $f_{x,y}$**

*A priori*, the relationship between $f_{x,y}$ and $\theta$ is not necessarily sinusoidal. To confirm that $F_x = f_x \cos\theta$ and $F_y = f_y \sin\theta$ are the correct terms for the driving force an independent fitting of $f_x$ and $f_y$ was undertaken. In these simulations values of $\omega_{x,y,m}$ and $\kappa_{mx,my}$ were kept constant and $F$ was a free fitting parameter extracted at each value of incident polarisation, $\theta$. We then plot the extracted $F_x$ and $F_y$ as a function of $\theta$ as shown in Figure 4.22. The points show the extracted values of $F_x$ and $F_y$ from the fitting procedure. The solid lines plot $F_x = f_x \cos\theta$ and $F_y = f_y \sin\theta$ with $f_x$ and $f_y$ taken from Table 4.2. The freely varying $F$ values (points) lie very close to the sinusoidal dependent $F$ values (lines). The sinusoidal relationship used in the model is therefore considered accurate.

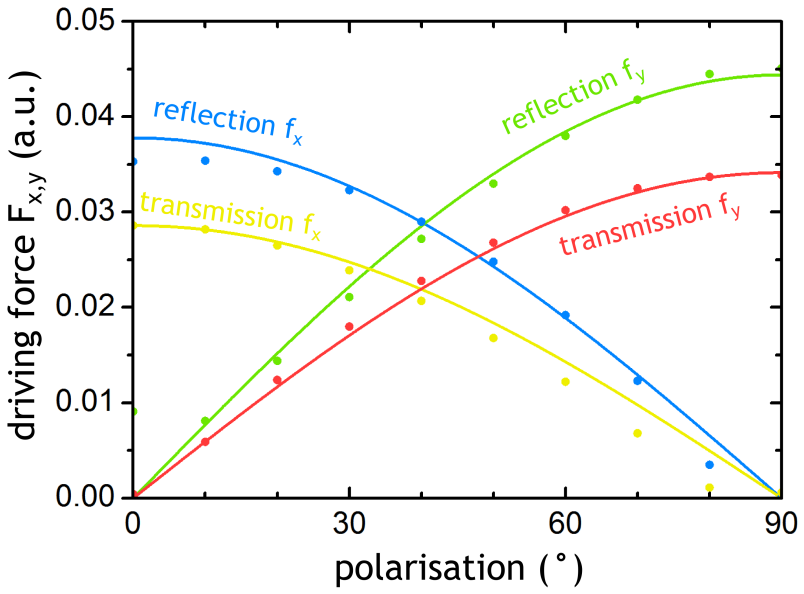


Figure 4.22: Polarisation dependence of the driving force $F_{x,y}$. Points show extracted values if $F_x$ and $F_y$ are considered free fitting parameters. Lines show the values of $F_x = f_x \cos\theta$ and $F_y = f_y \sin\theta$. Both reflection (green and blue) and transmission (red and yellow) fits are shown.

### 4.4.2 Quantum Mechanical Modeling of Plasmon-Molecule Interactions

In this section I show that the investigated system can be described by a quantum mechanical model by implementing a theoretical description developed by Dr. Nicolae C. Panoiu. Fano's original mathematical approach to the theoretical description of the interference of narrow and broad resonances was quantum mechanical [23] and provides a greater understanding of the physical system than a classical model. Following the success of our classical model (see Section 4.4.1) Dr. Panoiu attempted to describe the investigated system using the more sophisticated quantum mechanical approach. I developed his quantum mechanical model into a code that compares the models predictions to the experimentally extracted absorption of the system. The code then uses nonlinear least squares minimisation to extract the coupling parameters described in the model. The Matlab code is reproduced in Appendix D.

This model describes the interaction between the molecular vibrational mode of the carbonyl bond of PMMA and the LSPs produced by the asymmetrical cruciform apertures. Figure 4.23 shows the system schematically. Two continua represent the broad plasmon resonances. One of the continua corresponds to the higher energy plasmon mode which is excited by incident light with polarisation $\theta = 0°$ (blue). The other continuum corresponds to the lower energy plasmon mode which is excited by incident light with polarisation $\theta = 90°$ (red). The molecule is modeled as a two level system with ground state $|g\rangle$ (green) and excited state $|e\rangle$ (orange).

It is assumed that the interacting system is described by the Hamiltonian

$$\hat{H} = \hat{H}_0 + \hat{V}_a + \hat{V}_b + \hat{T} \tag{4.5}$$

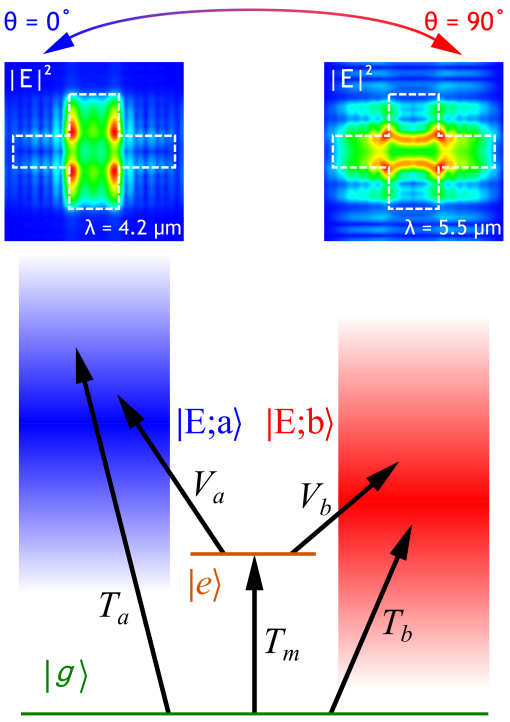


Figure 4.23: System schematic showing the ground state $|g\rangle$, the two LSP continua, $|E;a\rangle$ and $|E;b\rangle$, and the discrete molecular resonance $|e\rangle$ corresponding to the excited state of the PMMA carbonyl bond (see inset to Figure 4.2). Simulated spatial profiles (taken in the $x-y$ plane at the center of the aperture) show large field enhancement for $\theta = 0$ at $\lambda = 4.2$ $\mu$m and $\theta = 90°$ at $\lambda = 5.5$ $\mu$m. Aperture boundaries are indicated by dashed lines.

$H_0$ is the Hamiltonian of the system when the components are non-interacting and is given by

$$\hat{H}_0 = \hat{H}_g + \hat{H}_m + \hat{H}_a + \hat{H}_b = E_g|g \times g| + E_e|e \times e| + \sum_{i=a,b} \int dE \; E|E; i \times E; i| \tag{4.6}$$

Here the Hamiltonian of the ground state is $\hat{H}_g$, that of the non-interacting molecule is $\hat{H}_m$ and those of the two localized surface plasmons are $\hat{H}_a$ and $\hat{H}_b$. $E_g = 0$ is equal to zero as this corresponds to the ground state. The integrals describe the continuum of plasmons A and B.

The coupling between state $|e\rangle$ and plasmons A and B is given by

$$\begin{gathered} \hat{V}_i = \int dE \; V_{i,E}|E; i \times e| + hc \\ V_{i,E} = \langle E; i|\hat{V}_i|e\rangle \equiv v_i\sqrt{\rho_i(E)}, \\ i = a, b \end{gathered} \tag{4.7}$$

The probability to interact is assumed to be proportional to the density of states of the two plasmons. $v_a$ and $v_b$ are normalisation constants which determine the strength of this interaction. The density of states $\rho_a$ and $\rho_b$ of plasmons A and B respectively are described by Lorentzian functions centered at the plasmon energy $E_i$ and having width $\Gamma_i$.

$$\rho_i(\mathrm{E}) = \frac{1}{1 + \left(\frac{\mathrm{E}-\mathrm{E}_i}{\Gamma_i/2}\right)^2}, \;\; i = a, b \tag{4.8}$$

Values of $E_i$ and $\Gamma_i$ may be extracted from the measured plasmon resonances. However as the density of states is a Lorentzian and the measured plasmon resonances are asymmetrical the same problem arises that was encountered in the mechanical model. As in the mechanical model values of $\Gamma_p$ were taken from the side of the resonance between $\omega_i$ and $\omega_m$ (see Figure

4.21). Components $\hat{H}_0$, $\hat{V}_a$ and $\hat{V}_b$ can be thought of as the system in the dark, without excitation.

Component $\hat{T}$ corresponds to the probability of excitation of the two LSPs and the molecule from the ground state.

$$\hat{T} = \hat{T}_a + \hat{T}_b + \hat{T}_m \tag{4.9}$$

where

$$\begin{aligned} \langle E; a|\hat{T}_a|g\rangle &= \mu_a \sqrt{\rho_a(E)} \cos\theta \\ \langle E; b|\hat{T}_b|g\rangle &= \mu_b \sqrt{\rho_b(E)} \sin\theta \\ \langle e|\hat{T}_m|g\rangle &\equiv t_{e0} \end{aligned} \tag{4.10}$$

The normalization constants $\mu_a$ and $\mu_b$ are proportional to the coupling of the incident plane wave and the two localized plasmon resonances. The plasmon modes are dependent on the polarisation of incident light and so $\mu_a$ and $\mu_b$ have a sinusoidal relation. (The sinusoidal relationship has been confirmed in the classical model, see Figure 4.22.) The direct coupling of incident light and the molecule $t_{e0}$ is not constrained by polarisation or the density of states of the localized surface plasmons.

Dr. Panoiu applied Fano's original theory to the system and found that the absorption of the system is given by

$$A(E) = \mathcal{N}\left(|\langle\bar{\psi}_E|\hat{T}|g\rangle|^2 F(q,\epsilon) + |\langle\tilde{\psi}_E|\hat{T}|g\rangle|^2\right) \tag{4.11}$$

Here $\mathcal{N} = 2\pi n_s/I_0$ is a constant which is dependent on the number of molecules which interact with the enhanced field, $n_s$, and the intensity of the incoming beam, $I_0$. There are two components of $A(E)$, $|\langle\bar{\psi}_E|\hat{T}|g\rangle|^2 F(q,\epsilon)$

is the Fano resonance component and contains the Fano formula

$$F(q,\epsilon) = \frac{(q+\epsilon)^2}{1+\epsilon^2} \tag{4.12}$$

where the Fano parameters are given by

$$\epsilon = \frac{\mathrm{E}-\mathrm{E}_e}{\Gamma_d/2} - \frac{1}{|v_a|^2\rho_a + |v_b|^2\rho_b}\left[\frac{\mathrm{E}-\mathrm{E}_{p,a}}{\Gamma_{p,a}/2}|v_a|^2\rho_a + \frac{\mathrm{E}-\mathrm{E}_{p,b}}{\Gamma_{p,b}/2}|v_b|^2\rho_b\right] \tag{4.13}$$

and

$$q = \frac{t_{e0} + \pi\left(\mu_a v_a^*\rho_a \frac{\mathrm{E}-\mathrm{E}_{p,a}}{\Gamma_{p,a}/2}\cos\theta + \mu_b v_b^*\rho_b \frac{\mathrm{E}-\mathrm{E}_{p,b}}{\Gamma_{p,b}/2}\sin\theta\right)}{\pi(\mu_a v_a^*\rho_a\cos\theta + \mu_b v_b^*\rho_b\sin\theta)} \tag{4.14}$$

$|\langle\tilde{\psi}_E|\hat{T}|g\rangle|^2$ is the background that contains the rest of the resonance. Dr. Panoiu determined the components of $A(E)$ to be

$$|\langle\bar{\psi}_E|\hat{T}|g\rangle|^2 = \frac{\pi}{\gamma}|\mu_a v_a^*\rho_a\cos\theta + \mu_b v_b^*\rho_b\sin\theta|^2 \tag{4.15}$$

the continua contributing to the Fano line shape and

$$|\langle\tilde{\psi}_E|\hat{T}|g\rangle|^2 = \frac{\pi}{\gamma}|\mu_a v_a\sqrt{\rho_a\rho_b}\cos\theta + \mu_b v_b\sqrt{\rho_a\rho_b}\sin\theta|^2 \tag{4.16}$$

the continua producing the background. That plasmon A and B are excited by incident light with polarisation $\theta = 0°$ and $90°$ respectively is accounted for by the sinusoidal relation seen in these two terms. From Fano theory

$$\gamma(\mathrm{E}) = \pi\left[|v_a|^2\rho_a(\mathrm{E}) + |v_b|^2\rho_b(\mathrm{E})\right] \equiv \frac{\Gamma_{d(E)}}{2} \tag{4.17}$$

and describes the width of the modified excited state. Here $\Gamma_{d(E)}$ is the width of the discrete state.

The aperture array measured in Section 4.4.1 was used to test the quantum mechanical model. Absorption was extracted from the FTIR measurements using the relation $A = 1 - T - R$. Figure 4.24 (a) shows the result of this extraction. There are two global absorption peaks corresponding to the two plasmon resonances; one is present when $\theta = 0°$ and one when $\theta = 90°$. Superimposed on this global spectrum is the absorption resulting from the carbonyl bond at wavelength 5.79 $\mu$m. The magnitude of the absorption produced by the carbonyl bond increases as $\theta$ is rotated from 0° to 90°.

Values of $E_{p,a}$, $E_{p,b}$, $\Gamma_{p,a}$, $\Gamma_{p,b}$, $E_e$ and $\Gamma_d$ were extracted from the absorption data (wavenumbers are converted into units of energy using the relation $E = hc\tilde{\nu}$). $E_{p,a}$ and $\Gamma_{p,a}$ were taken from absorption measured when $\theta = 0°$ and $E_{p,b}$ and $\Gamma_{p,b}$ form absorption measured when $\theta = 90°$. As the global absorption spectrum produced by the plasmon resonances is asymmetric the values of $\Gamma_{p,a}$ and $\Gamma_{p,b}$ were extracted as shown in Section 4.4.1. The absorption extracted when $\theta = 0°$ gave values of $E_{p,a} = 0.2974$ eV and $\Gamma_{p,a} = 0.0828$ eV; the absorption extracted when $\theta = 90°$ gave values of $E_{p,b} = 0.2171$ eV and $\Gamma_{p,b} = 0.1225$ eV. The carbonyl bond resonance and damping were taken from the measurement of the 85 nm PMMA film shown in Figure 4.2 (and are therefore the same as those used in the classical model); $E_e = 0.2142$ eV and $\Gamma_d = 0.0012$ eV.

Initially, values of $\mu_a$, $\mu_b$, $v_a$, $v_b$ and $t_{e0}$ were also extracted from the absorption spectra measured when $\theta = 0°$ and 90° following the parameter-free modeling approach of Giannini *et al.* [52]. Here $|\mu_{a,b}|^2 = \Gamma_{p(a,b)}/2\pi$, $|v_a|^2 = |v_b|^2 = \Gamma_d/2\pi$ and $t_{e0} = |v_a|^2 = |v_b|^2$. A scaling factor was added to account for the variable number of molecules interacting with the plasmonic field. The scaling factor was estimated using unconstrained least squares fitting of the model prediction to the experimental data at each incident **E**

field polarisation as shown in Table 4.3.

| $\theta$ | Scaling Factor |
|---|---|
| 0 | 62.8 |
| 20 | 44.8 |
| 30 | 41.6 |
| 40 | 38.5 |
| 50 | 38.6 |
| 60 | 39.2 |
| 70 | 43.9 |
| 90 | 70.3 |

Table 4.3: Scaling factor used in the parameter-free fitting of the quantum mechanical model. Values used to produce Figure 4.24 (b).

Figure 4.24 (b) shows the result of this fitting. The global peaks of the LSP resonances are reproduced. However the feature formed by the interaction of the plasmon resonances and the carbonyl bond is a maximum in the experimental data and a minimum in the theoretical results. The poor agreement of the parameter free model with the experimental data is caused by the assumption that $v_a$ and $v_b$ are wholly dependent on the damping of the molecular resonance. This does not account for the spatial distribution of the optical near-field produced by the LSPs. We have seen in Figure 4.15 that this field is predicted to be polarisation-dependent and variable in intensity. In addition $t_{e0}$ is assumed to be equal to $\Gamma_d/2\pi$, which may not be true.

To investigate the possibility of variable coupling between incident light and the plasmonic system and between the variable plasmonic field and the molecule, $\mu_a$, $\mu_b$, $v_a$, $v_b$ and $t_{e0}$ must be changed to free fitting parameters. The initial conditions of the free fitting parameters were given as those predicted by Giannine *et al.* An unconstrained least squares fitting to the experimental absorption data at each incident **E** field polarisation was then

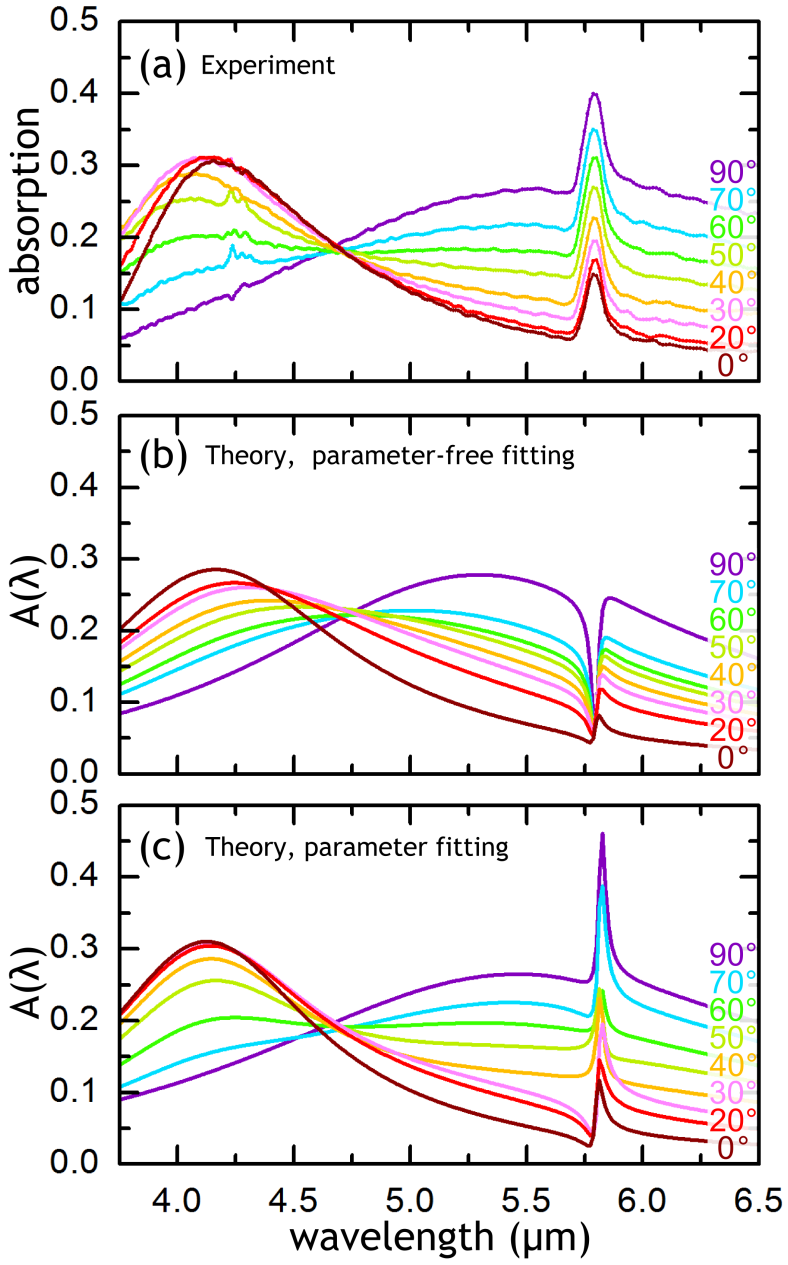


Figure 4.24: (a) Absorption $A = 1 - T - R$ of the structure extracted from FTIR measurements of transmission and reflection. (b) Best fit of experimental data using the quantum mechanical model and parameters $\mu_{(a,b)}$, $v_{(a,b)}$ and $t_{e0}$ extracted following the convention of Giannini *et al.*. (b) Best fit of experimental data using free fitting of the quantum mechanical model.

used to determine the variable values. Figure 4.24 (c) shows the result of this fitting. The global plasmonic spectra are reproduced and follow the absorption data. The local absorption maximum produced at the carbonyl bond wavelength is also reproduced and follows the same trend as the experimental data.

Table 4.4 shows the best fit values of the free fitting parameters (Table 4.5 summarises the symbols used in the model, their description and units). The majority of the fitted values have similar magnitude over all values of $\theta$. As parameters $v_a$ and $v_b$ describe the coupling between the discrete state and the continuum their values are not expected to be equal over all values of $\theta$. This is because the near-fields produced by the LSPs at different **E** field polarisations are spatially variable, causing a variation in coupling between the continuum and the molecules. The predicted values of $v_b$ are uniformly smaller than the predicted values of $v_a$. This may be linked to the magnitude of the **E** field produced by the LSPs - numerical calculations predict that the field produced by the $E_{p,b}$ LSP resonance is smaller than the field produced by the $E_{p,a}$ LSP resonance. Some values of $v_b$ are negative, this is because we chose these values to be real (although a complex case could also be considered in the future). Variation in the fitted values of $\mu_a$ and $\mu_b$ are the result of changes in coupling of incident light to the plasmonic modes caused by the different **E** field polarisations of incident light.

Values of $t_{e0}$ are very much smaller than $|v_{a,b}|^2$ for all incident **E** field polarisations apart from $\theta = 90°$. This indicates that the molecules interact primarily with the optical near-field of the LSPs. As the wire grid polariser, the sample alignment and the apertures used in the experiment are not perfect the transmission and reflection spectra measured when $\theta = 0°$ and $\theta = 90°$ will include the excitation of both LSP modes. However, as the model

| $\theta$ | $v_a$ $(\mathrm{eV})^{\frac{1}{2}}$ | $v_b$ $(\mathrm{eV})^{\frac{1}{2}}$ | $t_{e0}$ eV | $\mu_a$ $(\mathrm{eV})^{\frac{1}{2}}$ | $\mu_b$ $(\mathrm{eV})^{\frac{1}{2}}$ | $\mathcal{N}$ $(\mathrm{eV})^{-1} \cdot \mathrm{s}$ |
|---|---|---|---|---|---|---|
| 0 | 0.0019 | $9.60\times10^{-04}$ | $1.26\times10^{-14}$ | 0.0923 | 0.2124 | 121.8 |
| 20 | 0.0016 | $7.76\times10^{-04}$ | $4.10\times10^{-14}$ | 0.1760 | 0.0842 | 33.2 |
| 30 | 0.0029 | $8.78\times10^{-04}$ | $1.99\times10^{-14}$ | 0.0895 | 0.0395 | 105.6 |
| 40 | 0.0084 | $-15.00\times10^{-04}$ | $5.16\times10^{-14}$ | 0.0740 | 0.0928 | 265.2 |
| 50 | 0.0027 | $-5.11\times10^{-04}$ | $2.75\times10^{-14}$ | 0.0948 | 0.1035 | 183.3 |
| 60 | 0.0029 | $-2.66\times10^{-04}$ | $-18.90\times10^{-14}$ | 0.2014 | 0.1858 | 39.0 |
| 70 | 0.0014 | $-3.84\times10^{-04}$ | $4.59\times10^{-14}$ | 0.0690 | 0.0661 | 274.1 |
| 90 | 0.0032 | $-2.40\times10^{-04}$ | $3.36\times10^{-4}$ | 0.1375 | 0.0833 | 174.0 |

Table 4.4: The result of free parameter fitting the quantum mechanical model. Values used to produce Figure 4.24 (c).

is dependent upon a sinusoidal relation only a single LSP mode is excited at these two polarisations. The interaction between the metamolecule and the carbonyl bond is strongest when $\theta = 90°$, as the resonances are more closely matched than at any other polarisation. These two factors lead to the anomalous prediction of $t_{e0}$ at $\theta = 90°$. It is also possible that the mutual coupling of the LSP modes may occur at all polarisations, this effect is not taken into account in the model but could be tested for in a further investigation of the system.

We have investigated the coupling between the enhanced electromagnetic field produced by the two LSP modes supported by sub-wavelength cruciform apertures and a molecular bond using a quantum mechanical model based on the Fano resonance. The model has allowed us to make predictions about the coupling of the molecule to the plasmon modes and the incident light. We see that because of the small predicted value of $t_{e0}$, the coupling of the discrete state to the incident light, in comparison to values of $v_{a,b}$, the coupling of the discrete state to the continuum, molecules are predicted to primarily interact with the near-field of the LSP modes. We have also seen that a parameter-free modelling approach (Figure 4.24 (b)) is inaccurate when applied to this system.

| Symbol | Definition | Units |
|---|---|---|
| $v_a$ | Coupling constant describing the interaction between the discrete state and continuum $A$ | $(\mathrm{eV})^{\frac{1}{2}}$ |
| $v_b$ | Coupling constant describing the interaction between the discrete state and continuum $B$ | $(\mathrm{eV})^{\frac{1}{2}}$ |
| $t_{e0}$ | Coupling constant describing the interaction between the incoming light and the discrete state | eV |
| $\mu_a$ | Coupling constant describing the interaction between the incoming light and continuum $A$ | $(\mathrm{eV})^{\frac{1}{2}}$ |
| $\mu_b$ | Coupling constant describing the interaction between the incoming light and continuum $B$ | $(\mathrm{eV})^{\frac{1}{2}}$ |
| $\rho_a$ | Density of states of continuum $A$ | |
| $\rho_b$ | Density of states of continuum $B$ | |
| $\Gamma_a$ | FWHM of continuum $A$ | eV |
| $\Gamma_b$ | FWHM of continuum $B$ | eV |
| $\Gamma_m$ | FWHM of discrete state | eV |
| $E_a$ | Energy of continuum $A$ | eV |
| $E_b$ | Energy of continuum $B$ | eV |
| $E_e$ | Energy of discrete state | eV |
| $\gamma$ | Defined by Equation 4.17 | eV |
| $\mathcal{N}$ | Structure dependent physical constant | $(\mathrm{eV})^{-1} \cdot \mathrm{s}$ |

Table 4.5: A list of symbols used in the quantum mechanical model, as well as their definition and physical units.

# Chapter 5

# Experimental Results and Analysis: Nonlinear Optics

Surface-SHG is extremely sensitive to surface composition, so much so that the effect may be used to monitor the adsorption of single monolayers and sub-picoseconds surface dynamics. The intensity of metallic surface-SHG is also very sensitive to the roughness of the surface, and to sub-wavelength surface pattering. This sensitivity allows surface-SHG to be engineered by changing the size and geometry of sub-wavelength surface patterns so that they support SPP and LSP resonances which form the desired SHG effect. As the fabrication of patterned surfaces allows far greater control over the position of SPP and LSP resonances than is available from a random rough surface, SHG hotspots, which are related to high electron density in the metal, may form. Fabrication of these plasmonic structures allows the positioning of SHG hot spots to be controlled, and their formation investigated.

In order it investigate this phenomenon we formed a collaboration with Dr. Ventsislav K. Valev, KU Leuven, to investigate the nonlinear behavior of plasmonic nano-structures using second harmonic generation microscopy.

Following the discussion of sample design I fabricated structures which were measured by Dr. Valev using a second harmonic generation (SHG) microscope located in Hasselt University. The measurements of two star shaped designs are discussed in Sections 5.1 and 5.2. Dr. Valev also measured the second harmonic generation produced by cruciform apertures corresponding to the geometry investigated in Chapter 4; the results of this investigation are discussed in Section 5.3.

The structures shown in Sections 5.1 and 5.2 were both fabricated using EBL lift-off (see Section 3.1.6). The structures shown in Section 5.3 are fabricated using EBL and argon ion milling (see Section 3.1.7). In both structures the metallic features contain a 5 nm chromium layer coated with 35 nm gold layer. In all cases the substrate is a 100 nm thick silicon dioxide layer thermally grown on a silicon wafer.

## 5.1 Chiral Nanostructures

Figure 5.1 shows an SEM micrograph of part of a right-handed chiral star array. The inset shows the chiral-star geometry in which four curving arms are attached to a central square section. The complete array contains $20 \times 20$ chiral star structures arranged in a square lattice with pitch of approximately 1.5 $\mu$m in both $x$ and $y$. The geometry has four-fold rotational symmetry. The chiral stars have width $w_a$ and the central section width $w_b$. The fabricated structures shown in the SEM are not symmetrical as two of the arms are smaller than intended. This deviation from design is regular and repeated in all the fabricated structures. The fabricated stars have dimensions $w_a = 800$ nm and $w_b = 290$ nm. Left-hand chiral star structures were also fabricated.

Dr. Valev measured the second harmonic generation of the chiral star

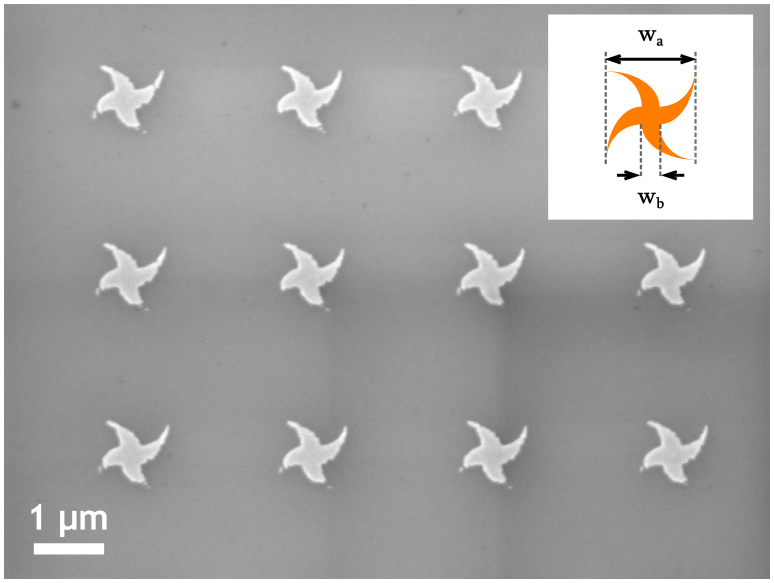


Figure 5.1: SEM micrograph showing right handed chiral star structures fabricated using the EBL, deposition and lift-off process. The metal structures (light areas) consist of a 5 nm chromium adhesion layer and a 35 nm gold layer. The inset shows the intended design of the structures (not to scale).

structures using a Zeiss LSM 510 scanning laser microscope (see Section 3.2.2). A fundamental wavelength of 800 nm was used and the laser light delivered in 120 fs pulses. The laser was scanned in 114 nm steps over the sample in a 512 $\times$ 512 point array, each point corresponding to a pixel in the SHG intensity map. Reflected light from the sample was passed through a short pass filter which removed light at the fundamental wavelength but allowed the 400 nm SHG to pass and be detected. The same detector gain was used in all measurements. Right and left hand circularly polarised light was produced by passing the laser beam through a quarter wave plate. The plate was rotated to 45° to the incoming beam to produce a left handed polarised light and to 135° to produce a right handed polarised light. The right and left hand chiral star structures were each measured with right and left handed circularly polarised light, producing four second harmonic

generation intensity maps. Figure 5.2 shows the four SHG intensity maps. Each intensity map contains $20 \times 20$ spots, each spot corresponding to one of the chiral star structures. Plate (a) and (c) show the SHG from right-handed chiral star structures illuminated by left-handed and right-handed circularly polarised light respectively. Plate (b) and (d) show the SHG produced by left-handed chiral star structures illuminated by left-handed and right handed circularly polarised light respectively. At first sight it appears that the intensity is equal in all the plates. However further analysis shows that the SHG intensity produced by the right-handed structures was maximised when the structures were illuminated with right-handed light and that left handed structures showed the same effect, with SHG maximised when the structures were illuminated with left handed light.

The sensitivity of the structures to the handedness of incident light may be assessed quantitatively using a histogram of pixel intensities. Figure 5.3 shows the number of pixels with intensity from zero to 70 (the intensity units are arbitrary). There are four intensity distribution curves corresponding to the four SHG intensity maps. The histograms produced by all the maps have similar pixel counts for intensities of zero to 16. These pixels correspond to background noise. At intensity values of 17 and greater the histograms produced by the two SHG maps shown in Figure 5.2 (a) and (d), which were recorded when structures were illuminated with polarised light of opposite handedness, show the same trend. The recorded SHG intensity decreases at the same rate in both histograms. When the structures were illuminated with polarised light of the same handedness, Figure 5.2 (b) and (c), the SHG intensity histograms show a higher count of pixels with intensity values of 17 and greater. There is a difference in the intensity between the right and left handed structures which is related to a chiral effect, which may be explored

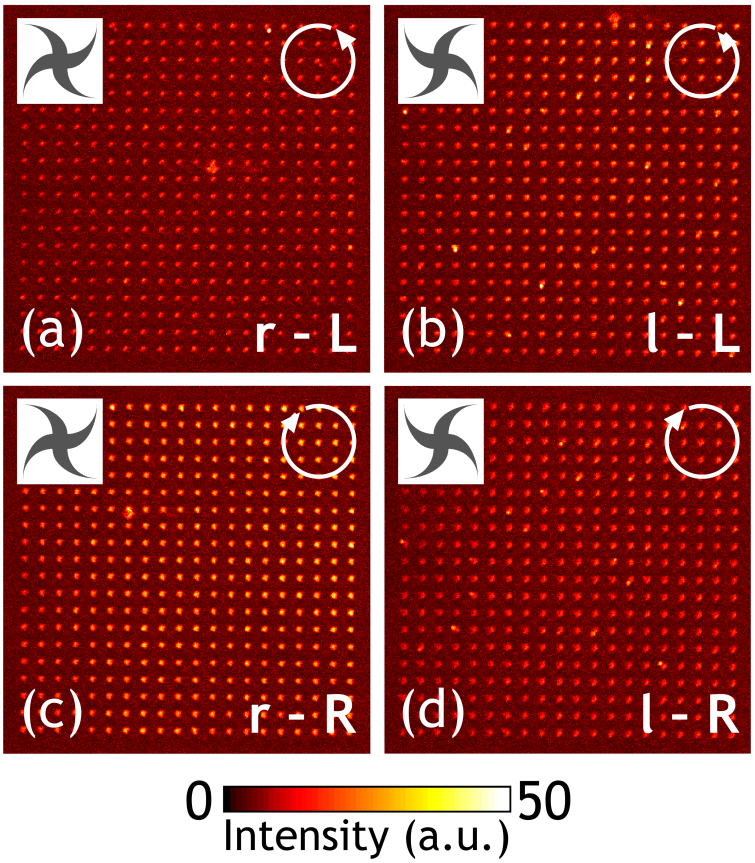


Figure 5.2: Intensity maps showing near-field SHG from two arrays of chiral star structures. Each spot is produced by a single structure in the array. Right-handed structures are shown in (a) and (c), left-handed structures are shown in (b) and (d). SHG was recorded for left-hand (shown in (a) and (b)), and right-hand (shown in (c) and (d)) circularly polarised light. Insets show the orientation of the structures and the handedness of the incident light. Labels r-L, l-L etc. indicated the handedness of the structure (lower case) and the circularly polarised light (upper case). Measurements were performed by Dr V. K. Valev, KU Leuven.

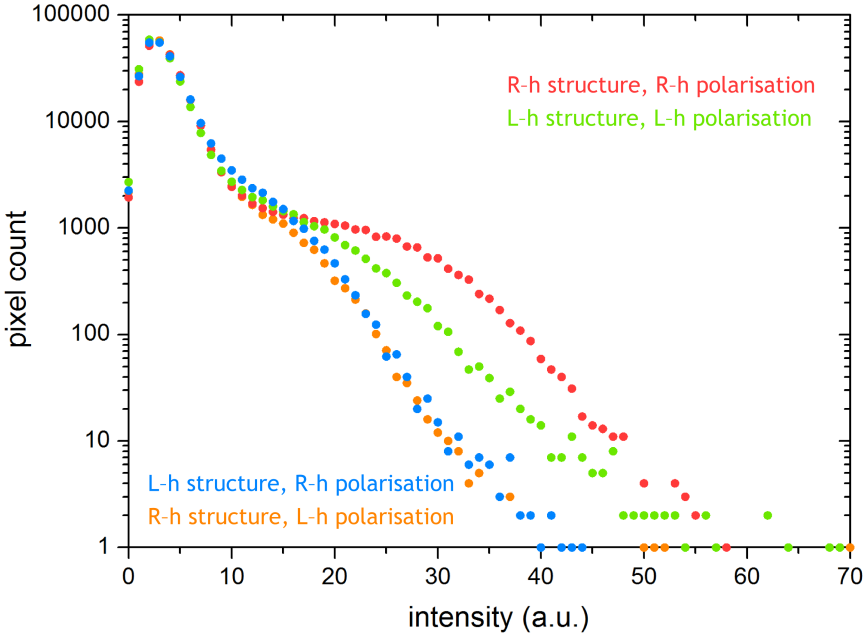


Figure 5.3: Histograms showing the pixel intensity count of the four SHG intensity maps shown in Figure 5.2. L-h and R-h refer to left-hand and right-hand respectively.

in future.

The sensitivity of the SHG of the chiral structures to the handedness of the incident circularly polarised light is an example of the SHG circular dichroism effect. The fundamental wavelength, $\lambda_f = 800$ nm, is equivalent to the width of the structure and therefore the features that cause the structures' chiral response are below the resolution limit of the microscope.

## 5.2 Sub-Wavelength Laser Ablation

Figure 5.4 shows part of a sample following fabrication of 'windmill' shaped metallic features. The structures are 1 $\mu$m across at the widest point, the straight edge is 200 nm long and the structures have pitch of 2.4 $\mu$m in the $x$ and $y$ directions. The complete array contains $20 \times 20$ structures. The

design was originally selected as one that may be sensitive to the handedness of circularly polarised light; however another outcome was observed when the geometry was illuminated with linearly polarised light.

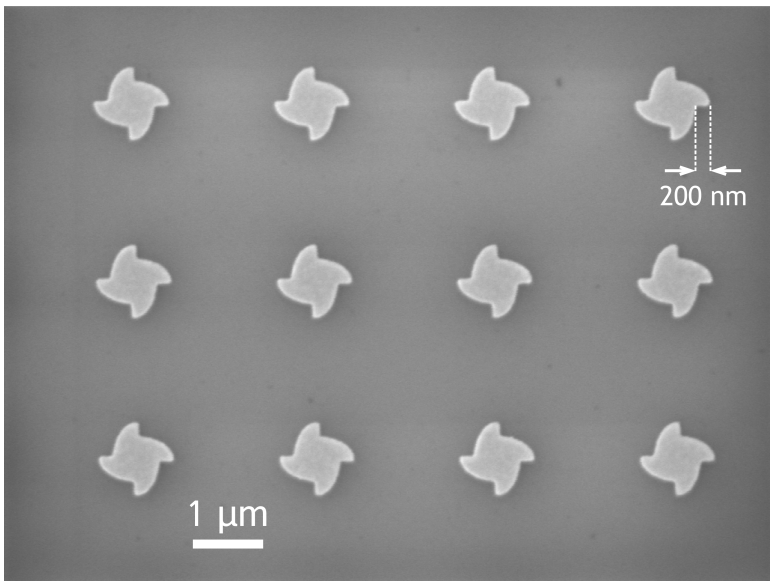


Figure 5.4: SEM micrograph showing windmill structures fabricated using the EBL, deposition and liftoff process. The metal structures (light areas) consist of a 5 nm chromium adhesion layer and a 35 nm gold layer.

Dr. Valev measured the second harmonic generation of the windmill structures using a Zeiss LSM 510 scanning laser microscope (see Section 3.2.2). Two polarisations of incident light, $\theta = 0°$ and $\theta = 90°$ were used. The fundamental wavelength was 800 nm and the laser light delivered in 120 fs pulses. Figure 5.5 shows the qualitative results of the laser scanning microscopy; panels (a) and (b) show SEM micrographs of exposed structures, panels (c) and (d) show the corresponding near field second harmonic generation.

The SEM micrographs both show two columns of metallic windmill structures. Each column contains three windmills; the windmills in the left hand column have been illuminated by the scanning laser microscope; the wind-

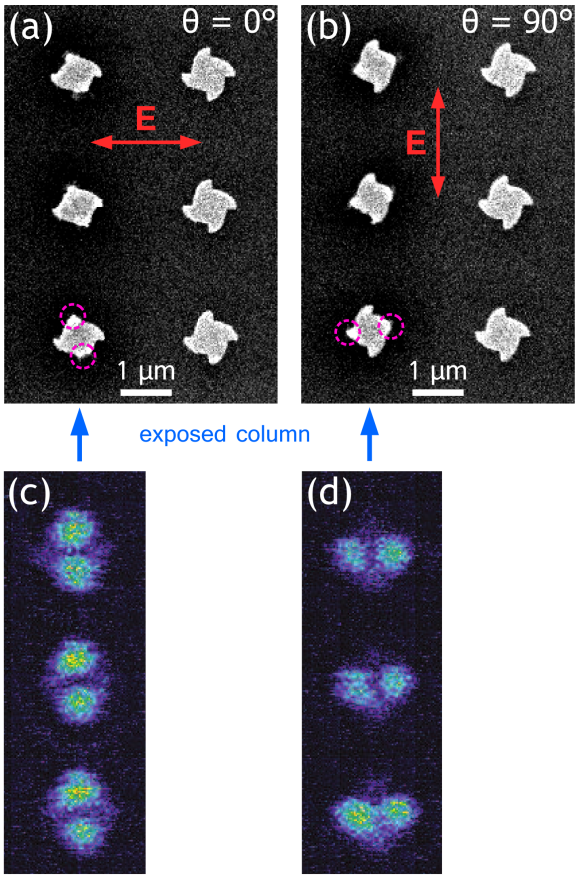


Figure 5.5: (a) and (b) show SEM micrographs of windmill structures, half of which have been exposed to an 800 nm wavelength scanning laser (exposed structures are located in columns indicated by blue arrows). Laser polarisation is shown by red arrow insets; pink insets indicate metal areas that have been ablated. (c) and (d) show SHG intensity maps produced by the scanning laser, SHG map (c) corresponds to SEM micrograph (a) and SHG map (d) corresponds to SEM micrograph (b). Measurements were performed by Dr. V. K. Valev, KU Leuven.

mills in the right hand column have not been illuminated. The exposed structures shown in (a) and (b) were illuminated with laser light of **E** field polarisation $\theta = 0°$ and $\theta = 90°$ respectively. The structures in the exposed columns all display similar deformation which is highlighted in two of the structures by broken pink rings. This deformation is caused by ablation of the metal layer by electrons that are excited by the laser light. The process was referred to as ablation, as opposed to melting, because as the intensity of the incident laser ration was increased, the gold areas of the irradiated regions disenable in SEM micrographs decreased, until the windmill structure was completely removed from the surface. The deformation is dependent on the polarisation of incident light, with the two points of the structures which are aligned parallel with the **E** field displaying less damaged than the two points that are aligned perpendicular to the **E** field.

The SHG intensity map produced by the laser scanning is also strongly dependent on the polarisation of the incident light. The areas of high SHG intensity are in the same orientation as the deformed region of the structures. Therefore the deformation of the structures may be linked to the regions of high SHG. This shows that melting of the structure is dependent on the shape of the structure and occurs in regions of the structure that are much smaller than the wavelength of the incident radiation.

## 5.3 Cruciform apertures

To apply SHG microscopy to the cruciform aperture geometry investigated in Chapter 4, apertures with a resonance close to 1 $\mu$m were fabricated. This wavelength was selected because the second harmonic generation (SHG) microscope used to measure the apertures has a maximum fundamental wavelength of 1 $\mu$m. Arrays of cruciform apertures containing $120 \times 120$

unit cells were fabricated using EBL and argon ion milling of a 35 nm gold and 5 nm chromium film on a 100 nm thick thermally grown layer of silicon dioxide ($SiO_2$) on a silicon substrate.

Figure 5.6 (a) shows the aperture geometry schematically and (b) shows an SEM micrograph of a typical array. The apertures shown in Figure 5.6 (b) have mean dimensions $G_x = 80$ nm, $G_y = 75$ nm, $L_x = 215$ nm, $L_y = 190$ nm, with pitch = 670 nm in both $x$ and $y$. Although the apertures appear essentially symmetrical there should still be a variation in the optical near-field because two LSP modes are supported, one in each of the apertures arms. These modes are dependent upon the **E** field polarisation of incident light. This is highlighted later by Figure 5.10, the output of the rigorous coupled-wave analysis used to design the structures.

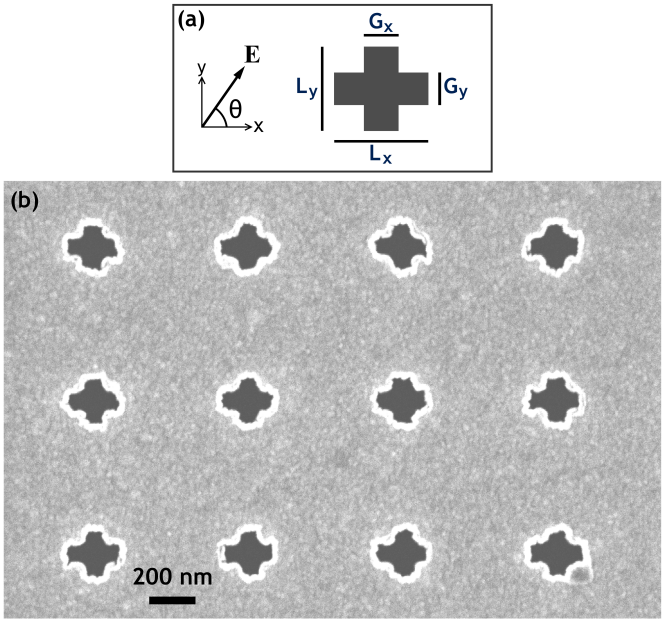


Figure 5.6: (a) Aperture geometry and definition of **E** field polarisation. (b) SEM micrograph showing part of an asymmetric cruciform aperture array fabricated using EBL and argon ion milling. Aperture dimensions are $L_x$ = 220 nm, $L_y$ = 190 nm, $G_x$ = 80 nm, $G_y$ = 70 nm, with pitch 670 nm in both $x$ and $y$

These apertures were designed to have resonance at approximately 1 $\mu$m wavelength with a magnitude that was tunable by adjusting the incident **E** field polarisation. Designed aperture dimensions were limited by the resolution of the EBL/argon ion milling fabrication method. Following fabrication aperture arrays were imaged using an SEM to determine aperture dimensions.

Figure 5.7 (a) and (b) show the SHG microscope intensity maps of the apertures shown in Figure 5.6 when they were illuminated with 1 $\mu$m wavelength light having **E** field polarisations $\theta = 0°$ and $\theta = 90°$ respectively. The laser was focused to a spot and scanned over the surface in 22 nm steps. Light from the sample with wavelength below 650 nm is passed through a beam splitter to the detector. The detected SHG at wavelength 500 nm was radiated from the surface of the sample. The two intensity maps show an array of $15 \times 17$ distinct spots that have high SHG intensity. Each of these high intensity regions corresponds to a single cruciform aperture. The low intensity region at the left hand side of the intensity map corresponds to the unpatterned gold surface.

Although at first sight the high intensity regions appear to be identical a variation in intensity with $\theta$ may occur. To determine the change in shape of the high intensity regions a row and column summation was used. Figure 5.8 illustrates the summation method. Figures 5.8 (a) and (b) show nine circular regions of high intensity. The regions in (a) are circular and the regions in (b) are elliptical. To show that the regions are either circular or elliptical a summation of the row and column values of the intensity matrix is performed. Figure 5.8 (c) and (d) show the summation of the rows and columns of the circular and elliptical intensity regions respectively. The row and column summations of an $n \times n$ matrix containing matrix

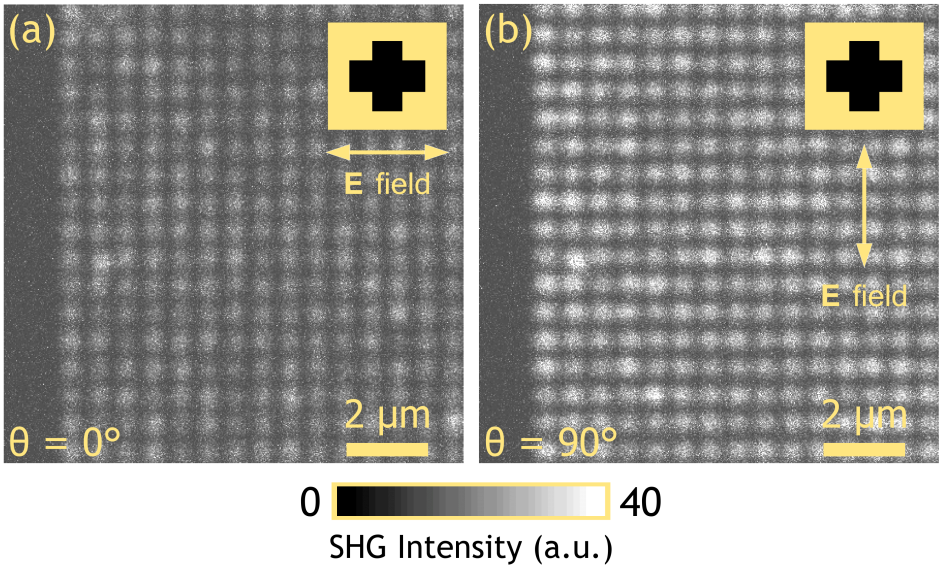


Figure 5.7: Intensity maps showing near-field SHG from an array of cruciform apertures. (a) Incident polarisation $\theta = 0°$. (b) Incident polarisation $\theta = 90°$. The insets to (a) and (b) show **E** field polarisation relative to aperture geometry. Measurements were performed by Dr V. K. Valev, KU Leuven.

elements designated $a_x$ and $a_y$ which form an array of elliptical intensity distributions with equal pitch in $x$ and $y$ and the major axes aligned with either a row or a column, as shown in Figure 5.8 (a) and (b), has the summation characteristic, when the eccentricity of the ellipse equals zero (*i.e.* the intensity distribution is circular)

$$\sum_{i=1}^{n} a_{x,i} = \sum_{i=1}^{n} b_{i,y}, \qquad x = y \tag{5.1}$$

This is plotted in Figure 5.8 (c) where the row and column sums are identical. For all other intensity distributions

$$\sum_{i=1}^{n} a_{x,i} \neq \sum_{i=1}^{n} b_{i,y}, \qquad x = y \tag{5.2}$$

The row and column summation of the elliptical intensity distribution is plotted in Figure 5.8 (d). When the summations are not equal the subtraction of the maximum column from the maximum row summation,

$$\sum_{i=1}^{n} a_{x,i} - \sum_{i=1}^{n} b_{i,y} = p, \tag{5.3}$$

indicates the alignment of the major axis of the ellipse. If $p$ is positive the ellipse major axis is aligned with the intensity distribution columns and if $p$ is negative it is aligned with the rows.

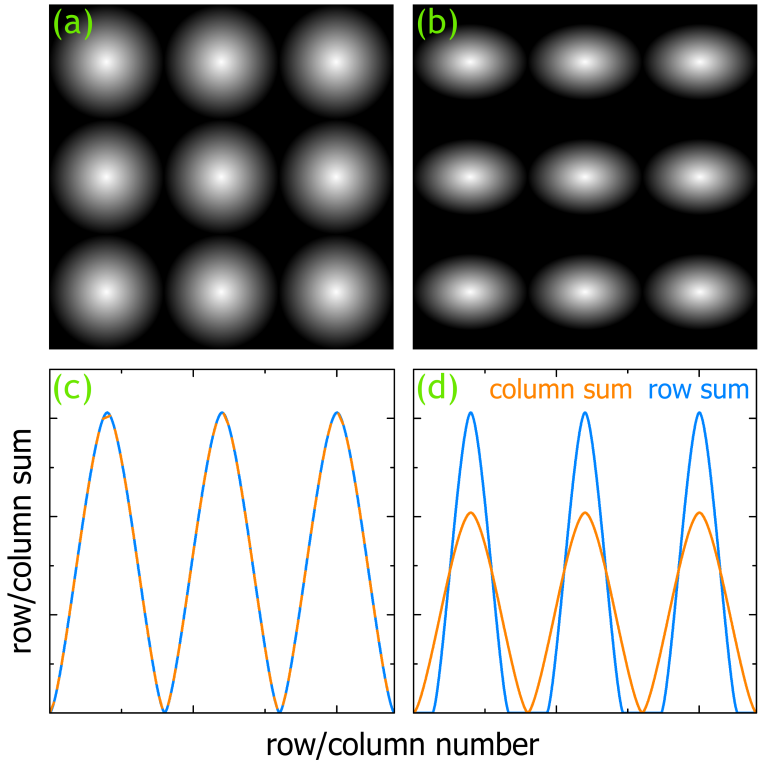


Figure 5.8: Summation of row and column values from schematic intensity maps. (a) Circular points. (b) Elliptical points with major axis running along map rows. (c) Summation of row (blue) and column (orange) values from intensity map (a). (d) Summation of row and column values from intensity map (b).

Figure 5.9 (a) and (b) show the row and column summation of the inten-

sity distribution map measured when $\theta = 0°$ and $\theta = 90°$ respectively for an array of $15 \times 15$ apertures taken from Figure 5.7. The integral over all intensity is equal for the row and column sums at each polarisation. The row and column sums are not zero between the local maxima because the apertures are not separated by a region of zero SHG. When $\theta = 0°$, $p$ is positive and the intensity distribution is elongated along the $\theta = 90°$ direction. When $\theta = 90°$, $p$ is negative and the intensity distribution is elongated along the $\theta = 0°$ direction. This shows that the apertures are sensitive to the polarisation of incident light and that the surface second harmonic generation produced by the apertures is also sensitive to this polarisation.

As the SHG is produced by movement of electrons in the metallic film these results could be used to infer the general charge distribution around the apertures. However, as the areas in each cross aperture that produce the SHG are not resolved. Only a general indication of charge distribution is provided. The areas which have high SHG may therefore correspond to areas that have high **E** field intensity. Figure 5.10 shows the field profile predicted at the surface of the apertures by numerical simulations at a wavelength of 1 $\mu$m. The predicted **E** field at the surface is stronger when $\theta = 90°$ and the **E** field distribution is sensitive to the polarisation of incident light. The SHG intensity shown in Figure 5.7 is also dependent on **E** field polarisation, showing the strongest SHG when $\theta = 90°$. The results are also interesting because a fundamental wavelength of 1 $\mu$m is exciting SHG (wavelength 500 nm) in structures with maximum feature size of 220 nm. Quantitative analysis of these results may be gained by further experimental investigation using other aperture geometries.

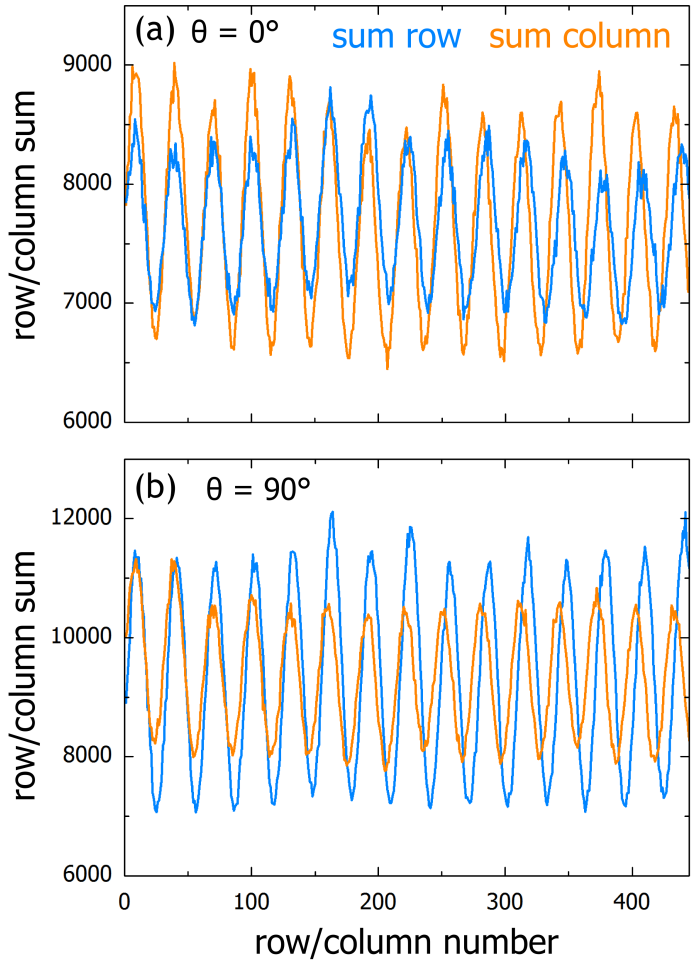


Figure 5.9: Summation of rows and columns from the SHG intensity maps shown in Figure 5.7, a square array of 15×15 apertures was selected from each map. (a) Cruciform aperture array illuminated with polarisation $\theta = 0°$ (Figure 5.7 (a)). (b) Cruciform aperture array illuminated with polarisation $\theta = 0°$ (Figure 5.7 (b)).

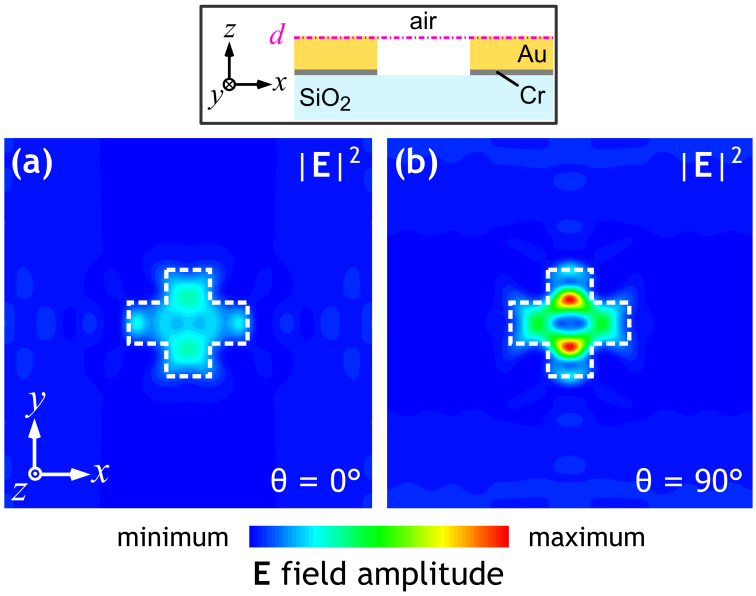


Figure 5.10: $|\mathbf{E}|^2$ distribution calculated in the $x-y$ plane at $z = d = 40$ nm (the surface of the metal layer of the measured apertures, shown in Figures 5.6 and 5.7); the origin of the $z$ axis is the surface of the $CaF_2$ substrate. Fields are calculated for two incident polarisations, (a) $\theta = 0°$ and (b) $\theta = 90°$. The dashed white lines show the aperture boundary. The fields are calculated at wavelength 1 $\mu$m corresponding to the fundamental laser wavelength used to produce Figure 5.7.

# Chapter 6

# Conclusions

## 6.1 Linear Optics

### 6.1.1 The Fano Resonance

LSP resonances created by sub-wavelength apertures are much broader than the narrow discrete resonances formed by molecular bonds. This mismatch in the resonance width suggests that interference between these resonances will produce an asymmetric Fano resonance at the molecular bond wavelength. By coating sub-wavelength apertures with molecules we are able to introduce resonant molecular bonds to the enhanced optical near-field formed by the LSP resonance. This allows us to investigate the interaction of a plasmon-molecular system by measuring its transmission and reflection spectra. As asymmetric cruciform aperture LSP resonances are sensitive to the **E** field polarisation of incident light we are able to tune the plasmon-molecular interactions in this device *in situ*.

To quantify tunable plasmon-molecular interactions the transmission and reflection spectra of PMMA-coated asymmetric cruciform apertures were measured using FTIR, and the absorption spectrum extracted, at various

**E** field polarisations. A classical mechanical oscillator model was then developed and used to simulate the **E** field polarisation dependence of the reflection and transmission spectra of the plasmon-molecular system. This classical model contains three linearly coupled harmonic oscillators; two of the oscillators are driven by a polarisation dependent external excitation, a third oscillator is coupled to the two externally driven oscillators. Fitting of the classical model to the FTIR measurements resulted in a good agreement between the measured data and the resonance of the classical system.

Two sets of coupling and driving values were extracted, one set for the transmission spectrum and one set for the reflection spectrum. The differences in the extracted coupling parameters between reflection and transmission data are most likely present because the model assumes zero absorption. The polarisation dependence of the external excitation was shown to be sinusoidal by allowing the external driving force to vary freely.

To increase our understanding of the physical system a quantum mechanical model was also developed by Dr. Nicolae Panoiu. This model was based on Fano's 1961 work [23] and contains a double continuum representing the two plasmonic modes and a discrete state representing the excited state of the PMMA carbonyl bond. I developed a fitting routine which applied the quantum mechanical model to the extracted absorption spectrum. This allowed us to predict constants which describe the coupling between the incident light and the LSP continua ($\mu_a$ and $\mu_b$), the incident light and the discrete state ($t_{e0}$) and the LSP continua and the discrete state ($v_a$ and $v_b$).

Initially the use of a parameter free approach to determine these variables was implemented as suggested by Giannini *et al.* [52]; however, this was found to produce an inadequate representation of the measured data. The

coupling variables were then allowed to vary freely, allowing the prediction of the coupling mechanisms between the discrete state of the carbonyl bond and the continuum of the plasmonic metamolecule. In this case we saw that $t_{e0}$ is much smaller than $|v_a|^2$ and $|v_b|^2$, indicating that the PMMA molecules interact primarily with the optical near-field formed by the LSPs.

The coupling between enhanced near fields and molecules could be used to increase the efficiency of devices that rely on the absorption of incident light, *e.g.* spectroscopic sensing systems. The investigated structure could potentially increase the functionality of these devices, as the enhanced field may be engineered at two distinct wavelengths, allowing *in situ* tuning between multiple molecular resonances over a broad spectrum in a single device.

### 6.1.2 FIB and EBL Fabrication Methods

Arrays of asymmetric cruciform apertures have been created using both FIB and EBL based fabrication methods. The apertures were formed in a metallic film on a transparent calcium fluoride substrate. A number of samples was fabricated; each sample consists of a square array of unit cells, with each unit cell containing a single cruciform aperture. The apertures support LSP modes which concentrate the electromagnetic field of incident light, the wavelength of this enhanced field being dependent on the aperture dimensions. As the apertures are asymmetric the LSPs may be tuned *in situ* by varying the **E** field polarisation of incident light.

Investigation of aperture transmission as a function of FIB dose found that increased dose resulted in an increase in aperture transmission. The transmission increase was found to be the result of two processes. The first is metal layer removal: an initial low dose resulted in close to zero aperture

transmission; as the dose was increased the aperture transmission also increased rapidly to approximately 30%. Inspection of SEM micrographs of the apertures shows that low FIB doses result in only a partial removal of the metal from the aperture area, and that the metal layer is almost completely removed when the FIB dose is increased above a critical level. The second process is responsible for the gradual increase in transmission with increasing dose observed after the initial rapid increase caused by metal layer removal. This process was identified as an increase in aperture area caused by additional FIB milling of the metal layer at the aperture edge. Normalising aperture transmission to aperture area has shown that aperture enlargement causes an increase in transmission that is separate to metal layer removal: the normalisation showed a convergence to a maximum aperture transmission of 44%/unit area following the initial rapid increase in transmission caused by metal layer removal.

A dose dependent blue shift in the transmission peaks of the FIB fabricated apertures was also observed. Rigorous coupled-wave analysis of the geometry indicated that this blue shift is the result of excavation of the calcium fluoride substrate which results in a lowering of the refractive index in the vicinity of the apertures. These results imply that care should be taken when calibrating an FIB system for plasmonic aperture fabrication; excavation of the substrate should be incorporated into the aperture design and the FIB dose should be calibrated so that only the required material is removed.

An EBL and argon ion milling process was also used to fabricate apertures. This allowed us to create arrays with larger area than those that could be fabricated using FIB, resulting in the improvement of the signal to noise ratio. The standard deviation of aperture dimensions was also improved by

the EBL fabrication technique, from 21 nm for FIB fabricated apertures, to 8 nm in the case of EBL fabricated apertures. However, these differences are dependent on the equipment used in the fabrication and may be overcome by using a more advanced FIB setup. There is a more fundamental difference between the two fabrication methods: the maximum transmission allowed by the FIB fabricated arrays was 38% whereas EBL and argon ion milling produced apertures with a maximum transmission of 79%. This suggests that the FIB process degrades the substrate or metal layer in some way that results in an increased absorption or reflection of incident light. Although the FIB process is more convenient, being resistless, the increased transmission losses incurred by this technique indicate that EBL and argon ion milling should be used to create plasmonic apertures if high transmission is desired.

## 6.2 Nonlinear Optics

Nonlinear optical measurements were made using a second harmonic generation (SHG) microscope which allowed the near field location of SHG hotspots to be determined. These measurements were made in collaboration with Dr. V. K. Valev. The near-field SHG of three different metallic geometries was measured using the technique. EBL was used to create the metallic patterns: two of the patterns contained uncoupled gold structures while the third was a cruciform aperture pattern. The uncoupled structures contained two geometries, referred to as chiral-star and 'windmill'.

The chiral star structure was found to display dichroic SHG which was dependent on the handedness of the incident circularly-polarised fundamental light. Measurements of SHG intensity maps found that right handed structures illuminated with right handed light produced higher pixel inten-

sity counts than the same structures illuminated with left handed light. The inverse was found in left handed structures. This example of SHG circular dichroism showed that the sub-wavelength shape of metallic structures has a large effect on its optical interaction.

The windmill star structure was used to investigate the dependence of near field SHG on the linear polarisation of the fundamental light. The comparison of SEM micrographs taken before and after SHG microscope imaging showed that regions which supported near field SHG hotspots had melted. The melting was dependent on the **E** field polarisation of the incident light, as was the SHG hotspot generation. Laser ablation of the metallic structures was therefore found to be dependent on the LSP resonance excited by the incident radiation.

SHG microscopy was used to investigate the spatial dependence of the near field SHG produced by a cruciform aperture structure illuminated by linearly polarised light. The maximum feature size of the cruciform apertures was 220 nm while the fundamental wavelength was 1 $\mu$m. Although individual near field hotspots could not be discerned, SHG intensity was found to be greater along the axis of the cruciform which was perpendicular to the **E** field polarisation when compared to the SHG signal from the axis of the cruciform parallel to the incident **E** field polarisation.

## 6.3 Further Work

This dissertation has indicated areas of pure science that could be investigated further. There are also practical applications of the technology that could be investigated from an engineering perspective. These ideas are highlighted in the following subsections.

### 6.3.1 Determining Sources of Loss in FIB Fabricated Samples

The maximum transmission achieved through a cruciform aperture array fabricated using FIB milling of a thin gold film 38% compared to 79% transmission through apertures of similar dimensions fabricated using EBL and argon ion milling. This suggests that that the FIB fabrication process produces large losses in plasmonic structures. It would be useful to understand the origin of these losses as loss is an important consideration in the future application of plasmonic systems. A systematic investigation of the material properties of the calcium fluoride substrate and metal layer following exposure to FIB would be required. It will also be necessary to consider the reflection as a function of FIB dose as this will indicate if the losses are caused by absorption or increased reflection.

### 6.3.2 Argon Ion Milling Dose

The transmission of apertures fabricated using the EBL technique has not been investigated with regard to argon ion beam dose. Methods used in the FIB dose investigation could be applied to this investigation. The results would most likely be similar to those found in the FIB dose investigation, with increasing dose producing an increase in transmission as the metal layer is removed. However, a better understanding of argon ion beam interaction with the metal layer and substrate could improve fabrication procedures.

### 6.3.3 Molecular Sensing

The current work details the interaction of the narrow band resonance of the carbonyl bond of PMMA. Molecules or mixtures of molecules with different molecular resonances could be introduced into the apertures to determine

the sensitivity of the array. These molecules could be in the form of a gas, as we have observed troughs in the transmission spectrum of the aperture arrays caused by exhaled carbon dioxide. The gold surface could also be functionalised enabling proteins or other biological molecules to bind to selective regions. Changes in the transmission or reflection from the surface could then be used to detect these molecules. The polarisation-tunable characteristics of the asymmetric cruciform could allow greater control over the wavelength range of a plasmonic based detector because the wavelength range covered by the two modes is much wider and allows tuning of the plasmon resonance intensity.

### 6.3.4 Micro-Fluidics

It will be relatively simple for the cruciform apertures to be fabricated on metal layers supported by very thin substrates which can also be removed. This would allow liquid to flow through the apertures, enabling continuous monitoring of the interaction of the plasmonic system and the liquid. This setup would allow two measurements to be made simultaneously; the first is the resonance shift produced by the refractive index of the liquid and the second is the interaction between the enhanced **E** field and red any optically active molecules present.

### 6.3.5 Three Dimensional Metamaterials

If more layers are included, the metasurfaces that have been investigated may be fabricated in multi-layer structures. Dielectric spacers between metal layers may take the form of magnesium fluoride which may be thermally evaporated *in situ* to create a stack of dielectric metal layers in which apertures could be milled using FIB or EBL and argon ion milling; this technique

has been demonstrated by Valentine *et al.* [116]. Another fabrication route would be the sequential deposition of patterned layers separated by a polymer, as have been used by Liu *et al.* [117]. This structure would allow the assessment of the bulk characteristics of the metamaterial, although losses incurred by the metal layers make this less attractive.

### 6.3.6 Nonlinear Optics

The field enhancement may be used to produce enhanced SHG if a nonlinear material is introduced into apertures that have LSP resonances. The material could be a crystal, such as gallium arsenide, which has been investigated in a geometry that was not polarisation sensitive by Fan *et al.* [118]. Other potential materials include poled chromophores dispersed in a polymer which could be spin coated onto the surface. It will also be possible to investigate the near field coupling between plasmonic structures using the SHG microscopy technique by systematically varying the separation of regions which support SHG hotspots.

# Appendix A

# Electron Beam Lithography

The process of using electron beam lithography (EBL) to create a PMMA mask that allows selective argon ion milling of a metal layer on a calcium fluoride ($CaF_2$) substrate is described below. Similar steps are used to create the independent chiral star and windmill structures seen in Sections 5.1 and 5.2, however in these cases the doped silicon substrate was sufficiently conducting to mitigate charging effects mentioned below.

Following the deposition of a chromium adhesion layer and gold film on a $CaF_2$ substrate (Section 3.1.3) a PMMA resist layer was spun on top of the gold layer. The PMMA resist used was produced by MicroChem Corp. consisting of anisol containing 2% PMMA solids with molecular weight 950000. The sample was spun first at 500 rpm for 5 seconds to spread the PMMA resist evenly over the gold surface and then the rotation rate was increased to 2000 rpm for 45 seconds. The rotation rate determines the final resist thickness. The sample was then placed on a 150 °C hotplate for 75 seconds to drive anisole from the film. A PMMA film of thickness approximately 85 nm results. The PMMA coated sample was then attached to the EBL sample holder using Kapton tape. The sample metal layer and sample holder

were joined electrically using a strip of carbon tape, creating an electrical contact between the metal layer and earth and thus preventing image and pattern drift caused by charging of the sample surface by the electron beam. The sample was then loaded into the EBL vacuum chamber and placed 7.5 mm below the SEM column. Following an initial rough focus of the electron beam the sample was then left for 30 minutes to 1 hour to allow stabilisation of the electron beam and the system to approach thermal equilibrium. A 10 keV electron beam passed through a 20 $\mu$m diameter aperture was focused on the surface of the resist. The smaller aperture size results in a sharp focus with small depth of field, allowing more detailed features to be exposed; however the exposure will take longer than when using a larger aperture because of the decrease in electron dose. Following focusing, a five second exposure of the PMMA to an unscanned electron beam produced an exposed area (spot) measuring between 15 nm and 30 nm diameter. This spot represents the width of a single pixel in a pixel exposure design. The electron beam current was then measured using a Faraday cup. The measured current is used to compute the exposure time of the EBL pattern which is dependent on the electron beam dose selected during design. A pattern created in the GDSII (Graphic Database System II stream format) format was then exposed.

A developer solution of one part MIBK three parts IPA was used to remove the areas of PMMA resist that were exposed to the electron beam. The sample was agitated in is the developer for 40 seconds and then transferred immediately to a bath of IPA for one minute to dilute the MIBK and stop the PMMA removal. The IPA was removed by blow drying with nitrogen.

The sample was then placed in an argon ion miller which removed the

exposed metal regions without milling away the entire PMMA masking layer (argon ion milling is discussed in Section 3.1.7). The PMMA mask was then removed by soaking in acetone overnight and ultrasonication of the sample. In some samples the PMMA mask located around the milled apertures could not be removed using acetone. This suggests that, in some cases, the PMMA about the apertures is polymerised (as acetone is unable to remove this material).

# Appendix B

# The Complex Conjugate in First Order Equations of Motion

The following outlines a proof which shows that the first order differential equations of motion used in Section 4.4.1 require complex conjugate terms (see Equations 4.3 and 4.4). The simplest system of the equations of motion is used; two undammed coupled oscillators with masses $X_1$ and $X_2$. The same process may be applied to the three damped oscillators used in the classical model.

First we define the conservation of energy term of the displacements $x_1$ and $x_2$ of the masses $X_1$ and $X_2$,

$$\frac{d}{dt}\left(|x_1|^2 + |x_2|^2\right) = 0, \tag{B.1}$$

which the equations of motion must satisfy. Next the equations of motion

of the two masses are stated:

$$\begin{aligned} -i\tfrac{dx_1}{dt} + i\alpha x_2 = 0 \\ -i\tfrac{dx_2}{dt} + i\alpha x_1 = 0 \end{aligned} \tag{B.2}$$

The masses are coupled to each other by a massless spring with spring constant $\alpha$ and experience zero damping. We multiply the first equation by $x_1^*$ and the second by $x_2^*$ and add the results together giving

$$-ix_1^*\frac{dx_1}{dt} + i\alpha x_2 x_1^* - ix_2^*\frac{dx_2}{dt} + i\alpha x_1 x_2^* = 0 \tag{B.3}$$

Now we write the complex conjugate of Equations B.2:

$$\begin{aligned} i\tfrac{dx_1^*}{dt} + i\alpha^* x_2^* = 0 \\ i\tfrac{dx_2^*}{dt} + i\alpha^* x_1^* = 0 \end{aligned} \tag{B.4}$$

We multiply the first equation by $x_1$ and the second by $x_2$ and add the results together giving

$$ix_1\frac{dx_1^*}{dt} - i\alpha^* x_2^* x_1 + ix_2\frac{dx_2^*}{dt} - i\alpha^* x_1^* x_2 = 0 \tag{B.5}$$

Combining Equations B.3 and B.5 and applying the product rule leads to

$$i\frac{d}{dt}(x_1 x_1^*) + i\frac{d}{dt}(x_2 x_2^*) - i(\alpha + \alpha^*)x_1^* x_2 - i(\alpha^* + \alpha)x_1 x_2^* = 0 \tag{B.6}$$

From the conservation of energy, Equation B.1, the first two terms are equal to zero, the use of the complex conjugate satisfies the condition that the other terms in the equation must also be equal to zero.

# Appendix C

# Matlab Code, Classical Model

## Classical Model, Experimental Data and Parameter Input

```
clear

%uses function importDPTfile to import FTIR data
%change numbers on lines 5 and 6 to select polarisation
importDPTfile('08May12_RhA1_Tr_Pol00.dpt')
    FTIRdata = x08May12_RhA1_Tr_Pol00;
                              theta = 0;

%takes columns from FTIR data
wavenumber_cm = FTIRdata(:,1);
transmission = FTIRdata(:,2);

%converts wavenumber cm^-1 to wavenumber um^-1
wavenumber_um = zeros(1, length(wavenumber_cm));
for k = 1:length(wavenumber_cm)
    wavenumber_um(k) = wavenumber_cm(k)/10000;
end

%creates the data sets ResonatorsFit will work with
aaa = wavenumber_um';
 bbb = transmission;

%select FTIR data range to work with
FTIRrange = 1334:1:1828;

%plot FTIR data
figure
scatter(aaa(FTIRrange),bbb(FTIRrange),'.b')
 hold on;

%fixed parameters taken from FTIR data
 gm = 0.00100;
  gx = 0.03940;
   gy = 0.04340;
    omm = 0.1728;
     omx = 0.2348;
      omy = 0.1822;
params(1) = theta;
params(2) = omx;
params(3) = omy;
params(4) = omm;
params(5) = gx;
params(6) = gy;
params(7) = gm;

%Initial Conditions for ResonatorsFit_2tr estimates
 fx = 0.02;%0.030;
  fy = 0.02;%0.035;
   kmx = 0.01;%0.0020;
    kmy = 0.01;%0.0020;
start_point(1) = fx;
start_point(2) = fy;
start_point(3) = kmx;
start_point(4) = 0.000;
start_point(5) = kmy;
start_point(6) = 0.000;

%run ResonatorsFit
[estimates, model] = ResonatorsFit_2tr(aaa(FTIRrange)',
bbb(FTIRrange)', params, start_point);
```

```
%apply estimates to model and plot
[sse, FittedCurve] = model(estimates);
plot(aaa(FTIRrange), FittedCurve, 'r', 'LineWidth', 2)
hold on
%apply IC to model and plot
[ssei, InitialCurve] = model(start_point);
plot(aaa(FTIRrange), InitialCurve, 'g')
hold on

%lable X and Y axis
xlabel('\mum^{-1}')
ylabel('|a_x|^2+|a_y|^2')

%output best fit estimates
estimates

%FIN
```

## Function importDPTfile

```
function importDPTfile(fileToRead1)
%IMPORTFILE(FILETOREAD1)
%  Imports data from the specified file
%  FILETOREAD1:  file to read

%  Auto-generated by MATLAB on 09-May-2012 12:08:53

% Import the file
rawData1 = importdata(fileToRead1);

% For some simple files (such as a CSV or JPEG files), IMPORTDATA
might
% return a simple array.  If so, generate a structure so that the
output
% matches that from the Import Wizard.
[~,name] = fileparts(fileToRead1);
newData1.(genvarname(name)) = rawData1;

% Create new variables in the base workspace from those fields.
vars = fieldnames(newData1);
for i = 1:length(vars)
    assignin('base', vars{i}, newData1.(vars{i}));
end
```

## Classical Model Fitting Function

```
function [estimates, model] = ResonatorsFit_2tr(xdata, ydata, params,
start_point)

model = @CoupledResonators;

% fminsearch fitting options
options =
optimset('MaxFunEvals',10000*length(xdata),'MaxIter',1000*length(xdata
),'TolFun',1.e-5,'TolX',1.e-5);

% unconstrained nonlinear minimization of the sum of the squares of
errors
estimates = fminsearch(model, start_point, options);

    % Function imports constants and variables then implements
Cramer's
    % rule to solve the equations of motion for each value of omega
    function [sse, FittedCurve] = CoupledResonators(fit_params)
        % constants
        theta = params(1);
        omx = params(2);
        omy = params(3);
        omm = params(4);
        gx = params(5);
        gy = params(6);
        gm = params(7);

        % variables
        fx = fit_params(1);
        fy = fit_params(2);
        kmx = fit_params(3)+1i*fit_params(4);
        kmy = fit_params(5)+1i*fit_params(6);

        FittedCurve = zeros(1,length(xdata));

        % loop solves equations of motion for each x data point
        for k=1:length(xdata)
            om = xdata(k);
            v = [-fx*cos(theta) -fy*sin(theta) 0]';
            vx =[om-omx-1i*gx 0 -1i*conj(kmx)]';
            vy =[0 om-omy-1i*gy -1i*conj(kmy)]';
            vm =[1i*kmx 1i*kmy om-omm-1i*gm]';
            Delta = det([vx vy vm]);
            ax = det([v vy vm])/Delta;
            ay = det([vx v vm])/Delta;
            am = det([vx vy v])/Delta;
            FittedCurve(k) = abs(ax)^2+abs(ay)^2;
        end
        % sum of the squares of errors of a loop iteration
        ErrorVector = FittedCurve - ydata;
        sse = sum(ErrorVector.^2);
    end
end
```

# Appendix D

# Matlab Code, Quantum Mechanical Model

## Quantum Mechanical Model, Experimental Data and Parameter Input

```
clear

theta = (pi)/9;

c = 299792458*10^6; % um.s^-1
h = 4.135667517e-015; % eV.s

%uses function importDPTfile to import FTIR data
%change numbers on lines 5 and 6 to select polarisation
importDPTfile('06Dec11_RhA1_Re_Pol20.dpt')
FTIRrefnData = x06Dec11_RhA1_Re_Pol20;
  importDPTfile('08May12_RhA1_Tr_Pol20.dpt')
  FTIRtranData = x08May12_RhA1_Tr_Pol20;
                                pol = 20; % for output struct

%takes columns from FTIR data
wavenumber_cm = FTIRrefnData(:,1);
reflection = FTIRrefnData(:,2);
transmission = FTIRtranData(:,2);

%load('absorptionSansPeakPol90');

% absorption = 1 - T - R
absorption = (1 - reflection - transmission);

% smooths absorption using moving average
absorptionSmooth = tsmovavg(absorption, 's', 6, 1);

%converts wavenumber cm^-1 to eV
IeV = zeros(1, length(wavenumber_cm));
for k0 = 1:length(wavenumber_cm)
    IeV(k0) = c*h*(wavenumber_cm(k0)/10000);
end

%FTIRrange and plotRange
FTIRrange = 1405:1:1683;
plotRange = 1300:1:1700;

%figure
hold on
scatter(IeV(FTIRrange), absorptionSmooth(FTIRrange), '.b')
hold on

% input parameters are taken from measurements made for the mechanical
% model of absorption
gm = 0.0010;
 gx = 0.0668;
  gy = 0.0988;
  omm = 0.1728;
   omx = 0.2399;
    omy = 0.1751;

% convert width of PMMA, plasmon a and b and peak positions into units
eV
GAMd = c*h*gm;
GAMpa = c*h*gx;
 GAMpb = c*h*gy;
     Ee = c*h*omm;
     Epa = c*h*omx;
```

```
      Epb = c*h*omy;

parameter(1) = Ee;
parameter(2) = Epa;
parameter(3) = Epb;
parameter(4) = GAMd;
parameter(5) = GAMpa;
parameter(6) = GAMpb;

parameter(7) = theta;

% Va, Vb and t will be fitted
Va = 1.4e-5;
 Vb = 1.4e-5;
   t = 2e-14;
  muA = 0.12;
   muB = 0.12;
scalingFactor = 120;
variable(1) = Va;
variable(2) = Vb;
variable(3) = t;
variable(4) = muA;
variable(5) = muB;
variable(6) = scalingFactor;

% run QMfanoFit FITTING happens here
[estimates, funVal, EXTflag, FMINoutput, model] =
QMfanoFit2_fitEverything4(IeV(FTIRrange)',
absorptionSmooth(FTIRrange)', parameter, variable);
% run QMfanoFit to create longModel for extra values in output
[dud1, dud2, dud3, dud4, longModel] =
QMfanoFit2_fitEverything4(IeV(plotRange)',
absorptionSmooth(plotRange)', parameter, variable);

% extends x data range to more than the initial FTIR data
[sse, FitCurve] = longModel(estimates);

% plotting
hold on
plot(IeV(plotRange), FitCurve, 'm', 'LineWidth', 2)
hold on

%converts wavenumber cm^-1 to eV
wavelength_um = zeros(1, length(wavenumber_cm));
for k1 = 1:length(wavenumber_cm)
    wavelength_um(k1) = 10000/wavenumber_cm(k1);
end

% combining wavelength and the fitted curve into one matrix
outputPlot = [wavelength_um(plotRange)', FitCurve'];

save Fitting_nGamma_11Aug12_theta20.dpt outputPlot -ASCII

% create a variable that will output estimates from
QMfanoFit2_fitEverything2
outputEstimates = struct('pol', pol, 'Va', estimates(1), 'Vb',
estimates(2), 't', estimates(3),'muA', estimates(4), 'muB',
estimates(5), 'scalingFactor', estimates(6), 'sse', sse);
outputEstimates

%lable X and Y axis
xlabel('E (eV)')
```

```
ylabel('I(E)')

% FIN
```

## Quantum Mechanical Model Fitting Function

```
function[estimates, funVal, EXTflag, FMINoutput, Ie] =
QMfanoFit2_fitEverything4(xData, yData, parameter, variable)

Ie = @qmIe;

options =
optimset('MaxFunEvals',10000*length(xData),'MaxIter',1000*length(xData
),'TolFun',1.e-5,'TolX',1.e-5);
[estimates, funVal, EXTflag, FMINoutput] = fminsearch(Ie, variable,
options);

    function[sse, Iscaled] = qmIe(ICparam)

        l = length(xData);
        E = xData;

        % set up all values that are going to be calculated and saved
on each loop iteration
        gamma = zeros(1,l);
        FanoBraKet = zeros(1,l);
        BackgroundBraKet = zeros(1,l);
        epsilon = zeros(1,l);
        q = zeros(1,l);
        I = zeros(1,l);
        F = zeros(1,l);
        rhoA = zeros(1,l);
        rhoB = zeros(1,l);

        Ee = parameter(1);
        Epa = parameter(2);
        Epb = parameter(3);
        GAMd = parameter(4);
        GAMpa = parameter(5);
        GAMpb = parameter(6);

        theta = parameter(7);

        Va = ICparam(1);
        Vb = ICparam(2);
        t = ICparam(3);
        muA = ICparam(4);
        muB = ICparam(5);
        scalingFactor = ICparam(6);

        % for loop calculates the values of the above parameters for
values of E
        for k2 = 1:l

            rhoA(k2) = 1/(1+((E(k2)-Epa)/(GAMpa/2))^2);
            rhoB(k2) = 1/(1+((E(k2)-Epb)/(GAMpb/2))^2);

            gamma(k2) = pi*((abs(Va)^2 * rhoA(k2)) + (abs(Vb)^2 *
rhoB(k2)));
```

```
            FanoBraKet(k2) =
(pi/gamma(k2))*abs(muA*Va*rhoA(k2)*cos(theta) +
muB*Vb*rhoB(k2)*sin(theta))^2;

            BackgroundBraKet(k2) = (pi/gamma(k2)) *
abs(muA*Vb*sqrt(rhoA(k2)*rhoB(k2))*cos(theta) +
muB*Va*sqrt(rhoA(k2)*rhoB(k2))*sin(theta))^2;

            % calculating epsilon
            epA = ((E(k2)-Epa)/(GAMpa/2)) * abs(Va)^2 * rhoA(k2);
            epB = ((E(k2)-Epb)/(GAMpb/2)) * abs(Vb)^2 * rhoB(k2);
            epsilon(k2) = ((E(k2) - Ee)/(GAMd/2)) - ( ((2*pi)/GAMd) *
(epA + epB) );

            % calculating q
            numA = muA*conj(Va)*rhoA(k2)*((E(k2)-
Epa)/(GAMpa/2))*cos(theta);
            numB = muB*conj(Vb)*rhoB(k2)*((E(k2)-
Epb)/(GAMpb/2))*sin(theta);
            den = pi*(muA*conj(Va)*rhoA(k2)*cos(theta) +
muB*conj(Vb)*rhoB(k2)*sin(theta));
            q(k2) = (abs(t) + pi*(numA + numB))/den;

            % calculating Fano part
            F(k2) = ( (q(k2) + epsilon(k2) )^2 / (1 + epsilon(k2)^2)
      );

            % calculating I(E)
            I(k2) = (FanoBraKet(k2) * F(k2) + BackgroundBraKet(k2)) *
E(k2);
        end
        Iscaled = I * scalingFactor;
        ErrorVector = Iscaled - yData;
        sse = sum(ErrorVector.^2);
    end
end
```

# Appendix E

# Articles in Peer Reviewed Journals

The following is a list of articles published in pear review journals which contain work covered in this dissertation:

**Polarization-induced tunability of localized surface plasmon resonances in arrays of sub-wavelength cruciform apertures** *P. G. Thompson, C. G. Biris, E. J. Osley, O. Gaathon, R. M. Osgood Jr., N. C. Panoiu, P. A. Warburton*, Optics Express **19** 25035 (2011)

**The role of chiral local field enhancements below the resolution limit of Second Harmonic Generation microscopy**,
*V. K. Valev, B. D. Clercq, X. Zheng, D. Denkova, E. J. Osley, S. Vandendriessche, A. V. Silhanek, V. Volskiy, P. A. Warburton, G. A. E. Vandenbosch, M. Ameloot, V. V. Moshchalkov, T. Verbiest*,
Optics Express **20** 256 (2012)

**Plasmon-Enhanced Sub-Wavelength Laser Ablation**, *V. K. Valev, D. Denkova, X. Zheng, A. I. Kuznetsov, C. Reinhardt, B. N. Chichkov, G. Tsutsumanova, E. J. Osley, V. Petkov, B. De Clercq, A. V. Silhanek, Y. Jeyaram, V. Volskiy, P. A. Warburton, G. A. E. Vandenbosch, S. Russev, O. A. Aktsipetrov, M. Ameloot, V. V. Moshchalkov, T. Verbiest* Adv. Mater. **24** OP29 (2012)

**Fano resonance resulting from a tunable interaction between molecular vibrational modes and a double-continuum of a plasmonic metamolecule**,
*E. J. Osley, C. G. Biris, P. G. Thompson, R. R. F. Jahromi, P. A. Warburton, N. C. Panoiu* Phys. Rev. Lett. **110** 087402 (2013)

The article Phys. Rev. Lett. **110** 087402 (2013) and its supplemental material is reproduced in the following pages.

# Appendix F

# Conference Presentations

The following is a list of conference papers which I presented and which contain work covered in this dissertation:

**Plasmon-mediated polarization-tuneable enhancement of optical absorption in a polymer film** *E. J. Osley, P. G. Thompson, C. G. Biris, N. C. Panoiu, P. A. Warburton*, APS March Meeting 2011

**BAPS.2011.MAR.B32.5**

**Tunable Fano resonance due to interaction between molecular vibrational modes and a double-continuum of a plasmonic meta-molecule** *E. J. Osley, C. G. Biris, P. G. Thompson, R. R. F. Jahromi, N. C. Panoiu, P. A. Warburton*, APS March Meeting 2013

**BAPS.2013.MAR.M20.15**

# References


[1] T. W. Ebbesen, H. J. Lezec, H. F. Ghaemi, T. Thio, and P. A. Wolff, "Extraordinary optical transmission through sub-wavelength hole arrays," *Nature*, vol. 391, pp. 667–669, 1998.

[2] S. M. Nie and S. R. Emery, "Probing single molecules and single nanoparticles by surface-enhanced Raman scattering," *Science*, vol. 275, pp. 1102–1106, 1997.

[3] D. Enders and A. Pucci, "Surface enhanced infrared absorption of octadecanethiol on wet-chemically prepared Au nanoparticle films," *Applied Physics Letters*, vol. 88, p. 184104, 2006.

[4] J. N. Anker, W. P. Hall, O. Lyandres, N. C. Shah, J. Zhao, and R. P. V. Duyne, "Biosensing with plasmonic nanosensors," *Nature Materials*, vol. 7, pp. 442–453, 2008.

[5] R. M. Roth, N. C. Panoiu, M. M. Adams, J. I. Dadap, and R. M. O. Jr., "Polarization-tunable plasmon-enhanced extraordinary transmission through metallic films using asymmetric cruciform apertures," *Optics Letters*, vol. 32, pp. 3414–3416, 2007.

[6] P. G. Thompson, C. G. Biris, E. J. Osley, O. Gaathon, R. M. O. Jr., N. C. Panoiu, and P. A. Warburton, "Polarization-induced tunability

of localized surface plasmon resonances in arrays of sub-wavelength cruciform apertures," *Optics Express*, vol. 19, pp. 25035–25047, 2011.

[7] H. A. Bethe, "Theory of diffraction by small holes," *Phys. Rev.*, vol. 66, pp. 163–182, Oct 1944.

[8] F. Przybilla, A. Degiron, J.-Y. Laluet, C. Genet, and T. W. Ebbesen, "Optical transmission in perforated noble and transition metal films," *Journal of Optics A: Pure and Applied Optics*, vol. 8, no. 5, pp. 458–463, 2006.

[9] S. G. Rodrigo, F. J. García-Vidal, and L. Martín-Moreno, "Influence of material properties on extraordinary optical transmission through hole arrays," *Phys. Rev. B*, vol. 77, p. 075401, 2008.

[10] H. J. Lezec, A. Degiron, E. Devaux, R. A. Linke, L. Martin-Moreno, F. J. Garcia-Vidal, and T. W. Ebbesen, "Beaming light from a subwavelength aperture," *Science*, vol. 297, no. 5582, pp. 820–822, 2002.

[11] K. J. K. Koerkamp, S. Enoch, F. B. Segerink, N. F. van Hulst, and L. Kuipers, "Strong influence of hole shape on extraordinary transmission through periodic arrays of subwavelength holes," *Phys. Rev. Lett.*, vol. 92, no. 18, p. 183901, 2004.

[12] R. Gordon, A. G. Brolo, A. McKinnon, A. Rajora, B. Leathem, and K. L. Kavanagh, "Strong polarization in the optical transmission through elliptical nanohole arrays," *Phys. Rev. Lett.*, vol. 92, no. 3, p. 037401, 2004.

[13] A. Degiron and T. W. Ebbesen, "The role of localized surface plasmon modes in the enhanced transmission of periodic subwavelength aper-

tures," *Journal of Optics A: Pure and Applied Optics*, vol. 7, pp. S90–S96, 2005.

[14] Z. Ruan and M. Qiu, "Enhanced transmission through periodic arrays of subwavelength holes: The role of localized waveguide resonances," *Phys. Rev. Lett.*, vol. 96, no. 23, p. 233901, 2006.

[15] L. Lin, L. B. Hande, and A. Roberts, "Resonant nanometric cross-shaped apertures: Single apertures versus periodic arrays," *Applied Physics Letters*, vol. 95, p. 201116, 2009.

[16] C. Y. Chen, M. W. Tsai, T. H. Chuang, Y. T. Chang, and S. C. Lee, "Extraordinary transmission through a silver film perforated with cross shaped hole arrays in a square lattice," *Applied Physics Letters*, vol. 91, no. 6, p. 063108, 2007.

[17] L. Lin and A. Roberts, "Light transmission through nanostructured metallic films: coupling between surface waves and localized resonances," *Optics Express*, vol. 19, pp. 2626–2633, 2011.

[18] L. Lin and A. Roberts, "Angle-robust resonances in cross-shaped aperture arrays," *Applied Physics Letters*, vol. 97, p. 061109, 2010.

[19] L. Lin, X. M. Goh, L. P. McGuinness, and A. Roberts, "Plasmonic Lenses Formed by Two-Dimensional Nanometric Cross-Shaped Aperture Arrays for Fresnel-Region Focusing," *Nano Letters*, vol. 10, pp. 1936–1940, 2010.

[20] H. T. Chen, W. J. Padilla, J. M. O. Zide, A. C. Gossard, A. J. Taylor, and R. D. Averitt, "Active terahertz metamaterial devices," *Nature*, vol. 444, pp. 597–600, 2006.

[21] S. Xiao, U. K. Chettiar, A. V. Kildishev, V. Drachev, I. C. Khoo, and V. M. Shalaev, "Tunable magnetic response of metamaterials," *Applied Physics Letters*, vol. 95, p. 033115, 2009.

[22] H. T. Chen, H. Yang, R. Singh, J. F. O'Hara, A. K. Azad, S. A. Trugman, Q. X. Jia, and A. J. Taylor, "Tuning the Resonance in High-Temperature Superconducting Terahertz Metamaterials," *Physical Review Letters*, vol. 105, p. 247402, 2010.

[23] U. Fano, "Effects of Configuration Interaction on Intensities and Phase Shifts," *Physical Review*, vol. 124, pp. 1866–1878, 1961.

[24] M. I. Stockman, S. V. Faleev, and D. J. Bergman, "Localization versus delocalization of surface plasmons in nanosystems: Can one state have both characteristics?," *Physical Review Letters*, vol. 87, p. 167401, 2001.

[25] S. Zhang, D. A. Genov, Y. Wang, M. Liu, and X. Zhang, "Plasmon-Induced Transparency in Metamaterials," *Physical Review Letters*, vol. 101, p. 047401, 2008.

[26] N. Verellen, Y. Sonnefraud, H. Sobhani, F. Hao, V. V. Moshchalkov, P. V. Dorpe, P. Nordlander, and S. A. Maier, "Fano Resonances in Individual Coherent Plasmonic Nanocavities," *Nano Letters*, vol. 9, pp. 1663–1667, 2009.

[27] F. Hao, P. Nordlander, M. T. Burnett, and S. A. Maier, "Enhanced tunability and linewidth sharpening of plasmon resonances in hybridized metallic ring/disk nanocavities," *Physical Review B*, vol. 76, p. 245417, 2007.

[28] F. Hao, Y. Sonnefraud, P. V. Dorpe, S. A. Maier, N. J. Halas, and P. Nordlander, "Symmetry Breaking in Plasmonic Nanocavities: Subradiant LSPR Sensing and a Tunable Fano Resonance," *Nano Letters*, vol. 8, pp. 3983–3988, 2008.

[29] Y. Sonnefraud, N. Verellen, H. Sobhani, G. A. E. Vandenbosch, V. V. Moshchalkov, P. V. Dorpe, P. Nordlander, and S. A. Maier, "Experimental Realization of Subradiant, Superradiant, and Fano Resonances in Ring/Disk Plasmonic Nanocavities," *ACS Nano*, vol. 4, pp. 1664–1670, 2010.

[30] J. A. Fan, C. Wu, K. Bao, J. Bao, R. Bardhan, N. J. Halas, V. N. Manoharan, P. Nordlander, G. Shvets, and F. Capasso, "Self-Assembled Plasmonic Nanoparticle Clusters," *Science*, vol. 328, pp. 1135–1138, 2010.

[31] Y. Francescato, V. Giannini, and S. A. Maier, "Plasmonic Systems Unveiled by Fano Resonances," *ACS Nano*, vol. 6, pp. 1830–1838, 2012.

[32] B. Gallinet and O. J. F. Martin, "*Ab initio* theory of Fano resonances in plasmonic nanostructures and metamaterials," *Physical Review B*, vol. 83, 2011.

[33] C. L. G. Alzar, M. A. G. Martinez, and P. Nussenzveig, "Classical analog of electromagnetically induced transparency," *American Journal of Physics*, vol. 70, pp. 37–41, 2002.

[34] Y. S. Joe, A. M. Satanin, and C. S. Kim, "Classical analogy of Fano resonances," *Physica Scripta*, vol. 74, no. 2, pp. 259–266, 2006.

[35] C. Wu, A. B. Khanikaev, R. Adato, N. Arju, A. A. Yanik, H. Altug, and G. Shvets, "Fano-resonant asymmetric metamaterials for ultrasensitive spectroscopy and identification of molecular monolayers," *Nature Materials*, vol. 11, pp. 69–75, 2012.

[36] G. C. Schatz, "Theoretical studies of surface enhanced raman scattering," *Accounts of Chemical Research*, vol. 17, no. 10, pp. 370–376, 1984.

[37] G. T. Boyd, T. Rasing, J. R. R. Leite, and Y. R. Shen, "Local-field enhancement on rough surfaces of metals, semimetals, and semiconductors with the use of optical second-harmonic generation," *Phys. Rev. B*, vol. 30, pp. 519–526, 1984.

[38] L. Salomon, F. Grillot, A. V. Zayats, and F. de Fornel, "Near-field distribution of optical transmission of periodic subwavelength holes in a metal film," *Phys. Rev. Lett.*, vol. 86, pp. 1110–1113, 2001.

[39] A. Krishnan, T. Thio, T. J. Kim, H. J. Lezec, T. W. Ebbesen, P. A. Wolff, J. Pendry, L. Martin-Moreno, and F. J. Garcia-Vidal, "Evanescently coupled resonance in surface plasmon enhanced transmission," *Optics Communications*, vol. 200, pp. 1–7, 2001.

[40] S. C. Hohng, Y. C. Yoon, D. S. Kim, V. Malyarchuk, R. Muller, C. Lienau, J. W. Park, K. H. Yoo, J. Kim, H. Y. Ryu, and Q. H. Park, "Light emission from the shadows: Surface plasmon nano-optics at near and far fields," *Applied Physics Letters*, vol. 81, no. 17, pp. 3239–3241, 2002.

[41] S. M. Williams, A. D. Stafford, K. R. Rodriguez, T. M. Rogers, and J. V. Coe, "Accessing surface plasmons with ni microarrays for en-

hanced ir absorption by monolayers," *Journal of Physical Chemistry B*, vol. 107, no. 43, pp. 11871–11879, 2003.

[42] K. R. Rodriguez, H. Tian, J. M. Heer, S. Teeters-Kennedy, and J. V. Coe, "Interaction of an infrared surface plasmon with an excited molecular vibration," *Journal of Chemical Physics*, vol. 126, no. 15, p. 151101, 2007.

[43] J. Dintinger, S. Klein, F. Bustos, W. L. Barnes, and T. W. Ebbesen, "Strong coupling between surface plasmon-polaritons and organic molecules in subwavelength hole arrays," *Phys. Rev. B*, vol. 71, no. 3, p. 035424, 2005.

[44] J. Dintinger, S. Klein, and T. W. Ebbesen, "Molecule-surface plasmon interactions in hole arrays: Enhanced absorption, refractive index changes, and all-optical switching," *Advanced Materials*, vol. 18, no. 10, pp. 1267–1270, 2006.

[45] Y. Sugawara, T. A. Kelf, J. J. Baumberg, M. E. Abdelsalam, and P. N. Bartlett, "Strong coupling between localized plasmons and organic excitons in metal nanovoids," *Phys. Rev. Lett.*, vol. 97, no. 26, p. 266808, 2006.

[46] J. Etou, D. Ino, D. Furukawa, K. Watanabe, I. F. Nakai, and Y. Matsumoto, "Mechanism of enhancement in absorbance of vibrational bands of adsorbates at a metal mesh with subwavelength hole arrays," *Physical Chemistry Chemical Physics*, vol. 13, pp. 5817–5823, 2011.

[47] G. A. Wurtz, P. R. Evans, W. Hendren, R. Atkinson, W. Dickson, R. J. Pollard, A. V. Zayats, W. Harrison, and C. Bower, "Molecular plasmonics with tunable exciton-plasmon coupling strength in

j-aggregate hybridized au nanorod assemblies," *Nano Letters*, vol. 7, no. 5, pp. 1297–1303, 2007.

[48] F. Neubrech, A. Pucci, T. W. Cornelius, S. Karim, A. Garcia-Etxarri, and J. Aizpurua, "Resonant Plasmonic and Vibrational Coupling in a Tailored Nanoantenna for Infrared Detection," *Physical Review Letters*, vol. 101, p. 157403, 2008.

[49] H. Chen, T. Ming, L. Zhao, F. Wang, L.-D. Sun, J. Wang, and C.-H. Yan, "Plasmon-molecule interactions," *Nano Today*, vol. 5, no. 5, pp. 494–505, 2010.

[50] A. Kinkhabwala, Z. Yu, S. Fan, Y. Avlasevich, K. Muellen, and W. E. Moerner, "Large single-molecule fluorescence enhancements produced by a bowtie nanoantenna," *Nature Photonics*, vol. 3, no. 11, pp. 654–657, 2009.

[51] I. M. Pryce, K. Aydin, Y. A. Kelaita, R. M. Briggs, and H. A. Atwater, "Highly Strained Compliant Optical Metamaterials with Large Frequency Tunability," *Nano Letters*, no. 10, pp. 4222–4227, 2010.

[52] V. Giannini, Y. Francescato, H. Amrania, C. C. Phillips, and S. A. Maier, "Fano resonances in nanoscale plasmonic systems: A parameter-free modeling approach," *Nano Letters*, vol. 11, no. 7, pp. 2835–2840, 2011.

[53] B. H. Stuart, *Infrared Spectroscopy: Fundamentals and Applications*, p. 114. John Wiley & Sons, Inc., 2004.

[54] J. A. Hutchison, D. M. O'Carroll, T. Schwartz, C. Genet, and T. W. Ebbesen, "Absorption-Induced Transparency," *Angewandte Chemie - International Edition*, vol. 50, pp. 2085–2089, 2011.

[55] R. W. Munn and C. N. Ironside, eds., *Principles and Applications of Nonlinear Opticlal Materials*. Blackie Academic & Professional, 1993.

[56] P. A. Franken, G. Weinreich, C. W. Peters, and A. E. Hill, "Generation of Optical Harmonics," *Physical Review Letters*, vol. 7, p. 118, 1961.

[57] D. F. Eaton, "Nonlinear Optical-Materials," *Science*, vol. 253, pp. 281–287, 1991.

[58] P. Günter, ed., *Nonlinear Optical Effects and Materials*, pp. 10–11. Springer, 2000.

[59] R. W. Terhune, P. D. Maker, and C. M. Savage, "Optical Harmonic Generation in Calcite," *Physical Review Letters*, vol. 8, pp. 404–406, 1962.

[60] N. Bloembergen, R. K. Chang, S. S. Jha, and C. H. Lee, "Optical Second-Harmonic Generation in Reflection from Media with Inversion Symmetry," *Physical Review*, vol. 174, pp. 813–822, 1968.

[61] C. K. Chen, T. F. Heinz, D. Ricard, and Y. R. Shen, "Detection of Molecular Monolayers by Optical Second-Harmonic Generation," *Physical Review Letters*, vol. 46, pp. 1010–1012, 1981.

[62] Y. R. Shen, "Surface properties probed by second-harmonic and sum-frequency generation," *Nature*, vol. 337, pp. 519–525, 1989.

[63] C. K. Chen, A. R. B. Decastro, and Y. R. Shen, "Surface-Enchanced Second-Harmonic Generation," *Physical Review Letters*, vol. 46, pp. 145–148, 1981.

[64] I. I. Smolyaninov, A. V. Zayats, and C. C. Davis, "Near-field second harmonic generation from a rough metal surface," *Physical Review B*, vol. 56, pp. 9290–9293, 1997.

[65] A. V. Zayats, I. I. Smolyaninov, and C. C. Davis, "Observation of localized plasmonic excitations in thin metal films with near-field second-harmonic microscopy," *Optics Communications*, vol. 169, pp. 93–96, 1999.

[66] A. V. Zayats, T. Kalkbrenner, V. Sandoghdar, and J. Mlynek, "Second-harmonic generation from individual surface defects under local excitation," *Physical Review B*, vol. 61, pp. 4545–4548, 2000.

[67] M. Zavelani-Rossi, M. Celebrano, P. Biagioni, D. Polli, M. Finazzi, L. Duo, G. Cerullo, M. Labardi, M. Allegrini, J. Grand, and P. M. Adam, "Near-field second-harmonic generation in single gold nanoparticles," *Applied Physics Letters*, vol. 92, p. 093119, 2008.

[68] C. Anceau, S. Brasselet, J. Zyss, and P. Gadenne, "Local second-harmonic generation enhancement on gold nanostructures probed by two-photon microscopy," *Optics Letters*, vol. 28, pp. 713–715, 2003.

[69] J. Butet, J. Duboisset, G. Bachelier, I. Russier-Antoine, E. Benichou, C. Jonin, and P.-F. Brevet, "Optical Second Harmonic Generation of Single Metallic Nanoparticles Embedded in a Homogeneous Medium," *Nano Letters*, vol. 10, pp. 1717–1721, 2010.

[70] A. Belardini, M. C. Larciprete, M. Centini, E. Fazio, C. Sibilia, M. Bertolotti, A. Toma, D. Chiappe, and F. B. de Mongeot, "Tailored second harmonic generation from self-organized metal nano-wires arrays," *Optics Express*, vol. 17, pp. 3603–3609, 2009.

[71] A. Belardini, M. C. Larciprete, M. Centini, E. Fazio, C. Sibilia, D. Chiappe, C. Martella, A. Toma, M. Giordano, and F. B. de Mongeot, "Circular Dichroism in the Optical Second-Harmonic Emission of Curved Gold Metal Nanowires," *Physical Review Letters*, vol. 107, p. 257401, 2011.

[72] P. J. Campagnola, M. de Wei, A. Lewis, and L. M. Loew, "High-resolution nonlinear optical imaging of live cells by second harmonic generation," *Biophysical Journal*, vol. 77, no. 6, pp. 3341–3349, 1999.

[73] S. I. Bozhevolnyi, J. Beermann, and V. Coello, "Direct observation of localized second-harmonic enhancement in random metal nanostructures," *Phys. Rev. Lett.*, vol. 90, p. 197403, May 2003.

[74] A. Papakostas, A. Potts, D. M. Bagnall, S. L. Prosvirnin, H. J. Coles, and N. I. Zheludev, "Optical manifestations of planar chirality," *Physical Review Letters*, vol. 90, p. 107404, 2003.

[75] V. K. Valev, N. Smisdom, A. V. Silhanek, B. D. Clercq, W. Gillijns, M. Ameloot, V. V. Moshchalkov, and T. Verbiest, "Plasmonic ratchet wheels: Switching circular dichroism by arranging chiral nanostructures," *Nano Letters*, vol. 9, pp. 3945–3948, 2009.

[76] V. K. Valev, "Characterization of nanostructured plasmonic surfaces with second harmonic generation," *Langmuir*, vol. 28, pp. 15454–15471, 2012.

[77] V. K. Valev, A. V. Silhanek, Y. Jeyaram, D. Denkova, B. D. Clercq, V. Petkov, X. Zheng, V. Volskiy, W. Gillijns, G. A. E. Vandenbosch, O. A. Aktsipetrov, M. Ameloot, V. V. Moshchalkov, and T. Verbiest, "Hotspot decorations map plasmonic patterns with the resolu-

tion of scanning probe techniques," *Physical Review Letters*, vol. 106, p. 226803, 2011.

[78] V. K. Valev, A. V. Silhanek, N. Verellen, W. Gillijns, P. V. Dorpe, O. A. Aktsipetrov, G. A. E. Vandenbosch, V. V. Moshchalkov, and T. Verbiest, "Asymmetric optical second-harmonic generation from chiral g-shaped gold nanostructures," *Physical Review Letters*, vol. 104, p. 127401, 2010.

[79] J. Weiner, "The physics of light transmission through subwavelength apertures and aperture arrays," *Reports on Progress in Physics*, vol. 72, pp. 1–19, 2009.

[80] S. A. Maier, *Plasmonics: Fundamentals and Applications*. Springer, 2010.

[81] L. Novotny and B. Hecht, *Principles of Nano-Optics*, pp. 369–413. Cambridge University Press, second ed., 2012.

[82] P. Drude, "Zur elektronentheorie der metalle," *Annalen der Physik*, vol. 306, no. 3, pp. 566–613, 1900.

[83] N. W. Ashcroft and N. D. Mermin, *Solid State Physics*, pp. 1–27. Saunders College Publishing, 1976.

[84] D. J. Griffiths, *Introduction to Electrodynamics*. Prentice Hall International, Inc., third ed., 1999.

[85] C. Kittel, *Introduction to Solid State Physics*, pp. 396–397. John Wiley & Sons, Inc., eighth ed., 2005.

[86] L. Novotny and B. Hecht, *Principles of Nano-Optics*, pp. 378–418. Cambridge University Press, 2008.

[87] A. R. Zakharian, J. V. Moloney, and M. Mansuripur, "Surface plasmon polaritons on metallic surfaces," *Optics Express*, vol. 15, no. 1, pp. 183–197, 2007.

[88] S. A. Maier, *Plasmonics: Fundamentals and Applications*, pp. 42–47. Springer, 2010.

[89] S. A. Maier, *Plasmonics: Fundamentals and Applications*, pp. 65–88. Springer, 2010.

[90] W. Murray and W. Barnes, "Plasmonic materials," *Advanced Materials*, vol. 19, pp. 3771–3782, 2007.

[91] A. V. Zayats, I. I. Smolyaninov, and A. A. Maradudin, "Nano-optics of surface plasmon polaritons," *Physics Reports*, vol. 408, pp. 131–314, 2005.

[92] U. Fano, G. Pupillo, A. Zannoni, and C. W. Clark, "On the absorption spectrum of noble gases at the arc spectrum limit," *Journal of Research of the National Institute of Standards and Technology*, vol. 110, no. 6, pp. 583–587, 2005.

[93] W. Jevons and A. G. Shenstone, "Spectroscopy: I. atomic spectra ," *Reports on Progress in Physics*, vol. 5, pp. 210–227, 1938.

[94] G. Cramer, *Introduction  l'analyse des lignes courbes algbriques*, pp. 657–659. 1750.

[95] D. W. Jordan and P. Smith, *Mathematical Techniques*, pp. 229–232. third ed., 2002.

[96] J. B. Lassiter, H. Sobhani, M. W. Knight, W. S. Mielczarek, P. Nordlander, and N. J. Halas, "Designing and Deconstructing the Fano Line-

shape in Plasmonic Nanoclusters," *Nano Letters*, vol. 12, pp. 1058–1062, 2012.

[97] M. G. Moharam and T. K. Gaylord, "Rigorous coupled-wave analysis of metallic surface-relief gratings," *Journal of the Optical Society of America A*, vol. 3, pp. 1780–1787, 1986.

[98] D. F. Bezuidenhout, *Handbook of Optical Constants of Solids II*, vol. 2, p. 815. Academic Press, 1991.

[99] I. H. Malitson, "A redetermination of some optical properties of calcium fluoride," *Applied Optics*, vol. 2, pp. 1103–1107, 1963.

[100] E. D. Palik, ed., *Handbook of Optical Constants of Solids*, vol. 1, pp. 749–763. Academic Press, 1985.

[101] R. R. Willey, *Practical Design and Production of Optical Thin Films*, pp. 298–299. Marcel Dekker, Inc., second ed., 2002.

[102] R. C. Weast, M. J. Astle, and W. H. Beyer, eds., *CRC Handbook of Chemistry and Physics*. CRC Press, Inc., 66 ed., 1985.

[103] L. A. Giannuzzi and F. A. Stevie, eds., *Introduction to Focused Ion Beams*. Springer, 2005.

[104] N. Yao, ed., *Focused Ion Beam Systems*. Cambridge University Press, 2007.

[105] V. E. Krohn and G. R. Ringo, "Ion source of high brightness using liquid metal," *Applied Physics Letters*, vol. 27, pp. 479–481, 1975.

[106] A. E. Grigorescu and C. W. Hagen, "Resists for sub-20-nm electron beam lithography with a focus on hsq: state of the art," *Nanotechnology*, vol. 20, no. 29, pp. 1–31, 2009.

[107] J. J. Cuomo, S. M. Rossnagel, and H. R. Kaufman, eds., *Handbook of Ion Beam Processing Technology*, pp. 8–20. Noyes Publications, 1989.

[108] P. R. Griffiths and J. A. de Haseth, *Fourier Transform Infrared Spectrometry*. John Wiley & Sons, Inc., 1986.

[109] S. P. Davis, M. C. Abrams, and J. W. Brault, *Fourier Transform Spectrometry*. Academic Press, 2001.

[110] A. A. Michelson and E. W. Morley, "On the relative motion of the earth and the luminiferous ether," *The American Journal of Science*, vol. 34, pp. 333–345, 1887.

[111] R. Hellwarth and P. Christensen, "Nonlinear optical microscopic examination of structure in polycrystalline znse," *Optics Communications*, vol. 12, pp. 318–322, 1974.

[112] P. J. Campagnola and L. M. Loew, "Second-harmonic imaging microscopy for visualizing biomolecular arrays in cells, tissues and organisms," *Nature Biotechnology*, vol. 21, no. 11, pp. 1356–1360, 2003.

[113] J. A. Schuller, E. S. Barnard, W. Cai, Y. C. Jun, J. S. White, and M. L. Brongersma, "Plasmonics for extreme light concentration and manipulation," *Nature Materials*, vol. 9, no. 3, pp. 193–204, 2010.

[114] S. N. Kasarova, N. G. Sultanova, C. D. Ivanov, and I. D. Nikolov, "Analysis of the dispersion of optical plastic materials," *Optical Materials*, vol. 29, pp. 1481–1490, 2007.

[115] M. A. Ordal, R. J. Bell, R. W. Alexander, L. L. Long, and M. R. Querry, "Optical-properties of 14 metals in the infrared and far infrared," *Applied Optics*, vol. 24, pp. 4493–4499, 1985.

[116] J. Valentine, S. Zhang, T. Zentgraf, E. Ulin-Avila, D. A. Genov, G. Bartal, and X. Zhang, "Three-dimensional optical metamaterial with a negative refractive index," *Nature*, vol. 455, pp. 376–379, 2008.

[117] N. Liu, H. Guo, L. Fu, S. Kaiser, H. Schweizer, and H. Giessen, "Three-dimensional photonic metamaterials at optical frequencies," *Nature Materials*, vol. 7, pp. 31–37, 2008.

[118] W. Fan, S. Zhang, N. C. Panoiu, A. Abdenour, S. Krishna, R. M. O. Jr., K. J. Malloy, and S. R. J. Brueck, "Second harmonic generation from a nanopatterned isotropic nonlinear material," *Nano Letters*, vol. 6, no. 5, pp. 1027–1030, 2006.

*I love deadlines. I like the whooshing noise they make as they fly by.*

Douglas Adams